



# **Laser-induced graphene-based wearable sensors for health monitoring**

**Khanthapak Thaipakdee**

**September 2024**

**Supervisors: Dr Youbin Zheng**

**Dissertation submitted to the University of Liverpool in partial  
fulfilment of the requirements for the degree of  
Master of Science in Engineering in Microelectronic Systems.**

## Abstract

---

Soft, flexible, and wearable electronics hold significant promise across various fields, such as healthcare, human-machine interfaces, and robotics. However, many current on-skin electronic devices are made from materials with limited gas permeability, which can impede sweat evaporation and reduce their long-term effectiveness. To overcome this limitation, this project aims to develop a wearable epidermal sensing system using direct carbon dioxide ( $\text{CO}_2$ ) laser irradiation. By utilizing the “laser-induced graphene (LIG)” technique, the project will simplify the fabrication process. The focus will be on optimizing laser parameters, including power levels, scanning speeds, and sensor patterns, to produce LIG on various composite substrates such as polyimide (PI), polyurethane (PU) tape, silicone protection tape, bandages, and medical tape. The mechanical and electrical properties, crucial for sensing, will be thoroughly evaluated. LIG transferred onto PU tape is anticipated to demonstrate enhanced characteristics due to its elasticity. The goal is to improve the detection of physiological signals, such as human movements like finger bending, hand gripping, and arterial pulse. In conclusion, this project aims to advance wearable sensing technology through LIG and innovative optimization methods, making a significant contribution to healthcare and human-machine interface technologies.

# Contents

---

Nomenclature	i
Acknowledgments	ii
Lists of Figures	iii
Lists of Tables	vi
<b>1. Introduction.....</b>	<b>1</b>
1.1. Background .....	1
1.2. Problem Statements.....	2
1.3. Aims and Objectives .....	3
1.4. Scope and Limitation .....	4
1.5. Outline of Final Report .....	4
<b>2. Literature Review .....</b>	<b>5</b>
2.1. Introduction of LIG .....	5
2.1.1. Discover of LIG .....	6
2.1.2. Formation of LIG.....	7
2.2. Synthesis and Attribute Adjustment of LIG .....	8
2.2.1. Variety of laser technologies .....	8
2.2.2. Variety of carbon-rich materials .....	12
2.3. Strain Detection Using LIG-based Sensors.....	15
2.3.1. Strain sensing evaluation .....	15
2.3.2. Fabrication techniques .....	17
2.3.3. Applications of strain sensors in Health Monitoring .....	18
2.3.4. Current Challenges and Future Directions.....	20
<b>3. Experimental Methodologies .....</b>	<b>21</b>
3.1. Materials and Preparation .....	21
3.1.1. LIG Fabrication Parameters .....	21
3.1.2. Transfer Materials .....	23
3.2. Design and Characterization of LIG Strain Sensors .....	26
3.2.1. Resistance Measurement Setup.....	26
3.2.2. Bending Test Methodology .....	26
3.2.3. Continuous Bending Test Method.....	27
3.2.4. Data Acquisition and Processing.....	27
3.2.5. Performance Metrics .....	28
3.2.6. Limitations and Considerations.....	29

# Contents

---

3.3.	Evaluation of Sensor Performance for Health Applications .....	30
3.3.1.	Finger Bending Monitoring.....	30
3.3.2.	Hand Grip Measurement.....	30
3.3.3.	Pulse Detection .....	31
3.3.4.	ECG Electrode Design and Evaluation .....	31
3.3.5.	Metrics in Classification .....	33
3.3.6.	Comparative Analysis .....	34
<b>4.</b>	<b>Results and Discussion.....</b>	<b>35</b>
4.1.	Influence of Power and Scanning Speed on LIG Performance.....	35
4.1.1.	Preliminary Experimental Setup .....	35
4.1.2.	Preliminary Results and Discussion.....	35
4.1.3.	Verification and Resistance Measurements .....	38
4.1.4.	Resistance Analysis.....	39
4.2.	Influence of Sensor Pattern on LIG Performance .....	41
4.3.	Performance of LIG-based Strain Sensors Fabricated on PI Substrates .....	44
4.4.	Performance of LIG-based Strain Sensors on PU Substrates.....	44
4.5.	Performance of LIG-based Strain Sensors on protection tape, bandage, and PE nonwoven tape. ....	73
4.6.	Application of LIG-based Strain Sensors.....	75
<b>5.</b>	<b>Conclusions and Further Work .....</b>	<b>94</b>
<b>6.</b>	<b>References .....</b>	<b>95</b>
<b>Appendix A:</b>	<b>Project Specification.....</b>	<b>102</b>
<b>Appendix B:</b>	<b>Ethical approval.....</b>	<b>107</b>
<b>Appendix C:</b>	<b>LIG-based Strain Sensors on protection tape, bandage, and PE nonwoven tape .....</b>	<b>110</b>
<b>Appendix D:</b>	<b>Coding.....</b>	<b>114</b>

---

## Nomenclature

---

CO<sub>2</sub> Carbon dioxide

DPI Dots per Inch

EEG Electroencephalogram

ECG Electrocardiogram

EMG Electromyography

EOG Electrooculography

LIG Laser-induced graphene

PDMS Polydimethylsiloxane

PET Polyethylene terephthalate

PI Polyimide

PPG Photoplethysmogram

PU Polyurethane

SEM Scanning electron microscopy

UV Ultraviolet

XRD X-ray diffraction

## Acknowledgments

---

I would like to express my deepest gratitude to my supervisor, Dr. Youbin Zheng, for his invaluable guidance, encouragement, and support throughout the duration of this project. His expertise and insight have been instrumental in shaping the direction of my research, and I am immensely grateful for the opportunity to learn under his mentorship.

I also wish to extend my thanks to the Department of Electrical Engineering and Electronics at the University of Liverpool for providing the resources and environment necessary for this research. My heartfelt appreciation goes to my lecturers and classmates, whose discussions and shared knowledge have contributed significantly to my academic growth.

A special thanks to my family and friends for their constant support and encouragement, especially during challenging times. Your belief in me has been a source of strength and motivation.

Lastly, a warm acknowledgment to my dog, who has been a constant companion, offering comfort and joy throughout this journey.

Thank you to everyone who has helped make this project a reality.

## Lists of Figures

---

Figure 2-1 SEM image of LIG morphology under different scanning cycles [46].	10
Figure 2-2 Relationship between LIG resistance and frequency, alongside SEM images [24].	11
Figure 2-3 LIG-based strain sensors for human motion detection [46].	19
Figure 3-1 LIG Strain sensor patterns.	22
Figure 3-2 Precursor material and transfer materials.	24
Figure 3-3 ECG electrode patterns. Right – Circular pattern, Left – Fractal-like pattern, Black – Hole	32
Figure 4-1 Photograph of LIG and layout with different laser power and scanning speed.	37
Figure 4-2 Photograph of LIG and layout with power from 5% to 25% and scanning speed from 200 mm/s to 400 mm/s.	39
Figure 4-3 LIG Resistance with different laser power and scanning speed.	40
Figure 4-4 Photograph of LIG with different sensing patterns.	43
Figure 4-5 Variation in electrical resistance of LIG serpentine during bending (Flat to 1.25 mm radius, synthesized at speed 200 mm/s, power 15%).	45
Figure 4-6 Electrical resistance of LIG serpentine at different bending radii (Original signal vs. After notch filter, synthesized at speed 200 mm/s, power 15%)	47
Figure 4-7 Electrical resistance of LIG serpentine at different bending radii (Signal after median filter vs. After outlier removal, synthesized at speed 200 mm/s, power 15%)	47
Figure 4-8 Variation in electrical resistance of LIG serpentine at different bending radii over multiple cycles (Synthesized at speed 200 mm/s, power 15%)	48
Figure 4-9 Variation in electrical resistance of LIG square during bending (Flat to 1.25 mm radius, synthesized at speed 200 mm/s, power 15%).	49
Figure 4-10 Variation in electrical resistance of LIG shutter during bending (Flat to 1.25 mm radius, synthesized at speed 200 mm/s, power 15%, 1 <sup>st</sup> cycle).	51
Figure 4-11 Variation in electrical resistance of LIG shutter during bending (Flat to 1.25 mm radius, synthesized at speed 200 mm/s, power 15%, 4 <sup>th</sup> cycle).	51
Figure 4-12 Variation in electrical resistance of LIG shutter during bending (Flat to 1.25 mm radius, synthesized at speed 200 mm/s, power 15%, 3 <sup>rd</sup> cycle).	52
Figure 4-13 Electrical resistance of LIG zigzag at different bending radii (Original signal vs. After notch filter, synthesized at speed 200 mm/s, power 15%)	53
Figure 4-14 Electrical resistance of LIG zigzag at different bending radii (Signal after median filter vs. After outlier removal, synthesized at speed 200 mm/s, power 15%)	53

## **Lists of Figures (Cont.)**

---

Figure 4-15 Variation in electrical resistance of LIG serpentine during bending (Flat to 1.25 mm radius, synthesized at speed 200 mm/s, power 20%).	54
Figure 4-16 Variation in electrical resistance of LIG square during bending (Flat to 1.25 mm radius, synthesized at speed 200 mm/s, power 20%).	55
Figure 4-17 Variation in electrical resistance of LIG shutter during bending (Flat to 1.25 mm radius, synthesized at speed 200 mm/s, power 20%).	56
Figure 4-18 Variation in electrical resistance of LIG zigzag during bending (Flat to 1.25 mm radius, synthesized at speed 200 mm/s, power 20%).	57
Figure 4-19 LIG-PU strain sensor with various sensing pattern.	61
Figure 4-20 Variation in electrical resistance of LIG-PU Serpentine during bending (Flat to 1.25 mm radius, synthesized at speed 200 mm/s, power 20%).	63
Figure 4-21 Variation in electrical resistance of LIG-PU square during bending (Flat to 1.25 mm radius, synthesized at speed 200 mm/s, power 20%).	63
Figure 4-22 Variation in electrical resistance of LIG-PU shutter during bending (Flat to 1.25 mm radius, synthesized at speed 200 mm/s, power 20%).	64
Figure 4-23 Variation in electrical resistance of LIG-PU zigzag during bending (Flat to 1.25 mm radius, synthesized at speed 200 mm/s, power 20%).	64
Figure 4-24 Variation in electrical resistance of LIG-PU Serpentine during bending (Flat to 1.25 mm radius, synthesized at speed 100 mm/s, power 10%).	66
Figure 4-25 Variation in electrical resistance of LIG-PU square during bending (Flat to 1.25 mm radius, synthesized at speed 100 mm/s, power 10%).	66
Figure 4-26 Voltage of LIG-PU Serpentine at different bending radii (Signal after outlier removal, synthesized at speed 100 mm/s, power 10%).	67
Figure 4-27 Voltage of LIG-PU square at different bending radii (Signal after outlier removal, synthesized at speed 100 mm/s, power 10%).	67
Figure 4-28 Electrical resistance of LIG-PU shutter during bending (Flat to 1.25 mm radius, synthesized at speed 100 mm/s, power 10%).	69
Figure 4-29 Electrical resistance of LIG-PU zigzag during bending (Flat to 1.25 mm radius, synthesized at speed 100 mm/s, power 10%).	69
Figure 4-30 Voltage of LIG-PU shutter at different bending radii (Signal after outlier removal, synthesized at speed 100 mm/s, power 10%).	70
Figure 4-31 Voltage of LIG-PU zigzag at different bending radii (Signal after outlier removal, synthesized at speed 100 mm/s, power 10%).	70

## Lists of Figures (Cont.)

---

Figure 4-32 Voltage of LIG-PU shutter during finger bending (Synthesized at speed 200, power 20%).	77
Figure 4-33 Voltage of LIG-PU shutter during elbow bending (Synthesized at speed 200 mm/s, power 20%).	77
Figure 4-34 Voltage of LIG-PU square during finger bending at 30° (Synthesized at speed 100, power 10%).	79
Figure 4-35 Voltage of LIG-PU square during finger bending at 90° (Synthesized at speed 100, power 10%).	79
Figure 4-36 Voltage of LIG-PU square during hand grip and stretch (Synthesized at speed 100 mm/s, power 10%).	82
Figure 4-37 Voltage of LIG-PU shutter during pulse detection (Original signal vs After filtering, Synthesized at speed 100 mm/s, power 10%)	85
Figure 4-38 Voltage of LIG-PU shutter during pulse detection (Signal after filtering, synthesized at speed 100 mm/s, power 10%, time duration: 30s to 35s).	85
Figure 4-39 Voltage comparison during pulse detection of LIG-PU square vs shutter (Signal after filtering, synthesized at speed 100 mm/s, power 10%, time duration: 30s to 35s).	86
Figure 4-40 LIG-ECG Electrodes with circular and fractal-like patterns (a) LIG-ECG electrodes with circular pattern, (b) LIG-ECG electrodes with fractal-like pattern, (c) ECG electrodes connected to ECG cables.	88
Figure 4-41 ECG signal processing: raw and denoised signals using wavelet transformation and high-pass filter (LIG-PI-Circle fabricated at 100 mm/s and 8% power).	92
Figure 4-42 Zoomed view of ECG signal features: P-wave, QRS complex, and T-wave identification.	92
Figure 4-43 Comparison of ECG signal features between circular and fractal-like patterns on PI substrates (100 mm/s, 10% Power): P-Wave, QRS Complex, and T-Wave identification.	93
Figure C-1 LIG strain sensor with different patterns on silicone protection tape.	110
Figure C-1 LIG strain sensor zigzag on medical tape (a) Normal sensor, (b) Sandwich covered with medical tape.	111
Figure C-3 Graphene square and shutter patterns on bandage (a) Initial state, (b) shutter pattern under stretch, and (c) square pattern under stretch.	113

## **Lists of Tables**

---

Table 2-1 Laser induced graphene materials, process and applications.	14
Table 3-1 Materials used in the experiment.	25
Table 4-1 Average and sheet resistance of various LIG sensor patterns.	42
Table 4-2 LIG-PI strain sensors evaluation with different patterns under various fabrication conditions.	60
Table 4-3 LIG-PU strain sensors evaluation with different patterns under various fabrication conditions.	72
Table 4-4 Change in resistance of LIG-PU sensor at different finger bending angles.	80
Table 4-5 Pulse detection performance comparison of LIG-PU shutter and square sensors fabricated at 100 mm/s and 10% power.	86
Table 4-6 Performance comparison of LIG-ECG electrodes with different patterns and power settings: true positives, false positives, false negatives, and cross-correlation scores.	93
Table A-1 Gantt chart.	104
Table A-2 Revised Gantt chart.	105
Table A-3 Risk Management.	106
Table A-4 Severity of the potential injury/damage.	106
Table C-1 Performance characteristics of LIG-based strain sensors with different patterns on silicone protection tape.	111

# **1. INTRODUCTION**

## **1.1. Background**

Graphene, a two-dimensional material composed of carbon atoms organized in a hexagonal pattern, has attracted significant interest in research and industrial sectors due to its remarkable mechanical attributes, optoelectronic behavior, thermal conductivity, and electromagnetic features [1]. Researchers have devised various conventional techniques for manufacturing graphene, such as physical exfoliation, chemical vapor deposition, and reduction of graphene oxide [2]. Despite their benefits, these techniques have apparent disadvantages, such as limited performance, increased energy consumption, significant waste byproducts, and complex processes that result in considerable costs and time consumption.

In response to these challenges, laser-induced graphene (LIG) has emerged as a promising alternative for synthesizing graphene. This novel method, which employs an infrared carbon dioxide ( $\text{CO}_2$ ) laser to convert commercial polymers into porous graphene directly, offers distinct advantages over traditional fabrication techniques [3]. The necessary apparatus for laser irradiation is widely accessible in the business community, and the process generates minimal waste. Additionally, the computer-controlled design allows for precise and straightforward management of the LIG pattern, enhancing the technique's versatility. Numerous studies have highlighted the simplicity, efficiency, and flexibility of the LIG approach [4].

Nevertheless, significant challenges remain in optimizing LIG technology, particularly for sensor applications. A key issue is the selection of suitable substrates for flexible sensors. Various carbon-based materials, including organic films, natural substances, and even food products, have been explored, but many fail to meet the necessary mechanical and operational standards [5]. Moreover, the choice of laser parameters, such as power, frequency, scanning speed, and beam diameter, critically impacts the quality of the synthesized LIG.

Notably, polyimide (PI) films, commonly used as substrates, lack the stretchability and sensitivity needed for effective strain sensing [6]. To address these issues, researchers have explored transferring the graphene pattern onto more stretchable materials like PDMS, rubber, and medical tape, which offer greater flexibility than PI. While these materials provide improved stretchability and sensitivity for strain sensing, their preparation involves complex procedures with multiple steps, requiring specialized equipment and resulting in high costs. Consequently, these factors make them impractical for mass production and widespread use in commercial applications [7].

## 1.2. Problem Statements

Given the limitations of current LIG sensor technologies—specifically, the inadequacies of traditional substrates and the complexities involved in their preparation—there is a clear need for improved methods to develop flexible, cost-effective, and high-performance LIG-based strain sensors. This project seeks to address these challenges by optimising the CO<sub>2</sub> laser cutting parameters using a compact laser cutting machine (Laserscript-LS3040 Desktop) and identifying appropriate materials to develop a wearable sensing system for health monitoring. The system will be designed to detect human motion and physiological signals with improved sensitivity and practicality. The goal is to streamline the production process by minimising the number of steps involved, reducing the need for complex equipment, and lowering both time and costs.

### **1.3.Aims and Objectives**

The objective of this project is to design and manufacture a wearable sensing system that uses LIG for health monitoring. This study will focus on improving two critical aspects: the parameters for CO<sub>2</sub> laser cutting and the materials used in the development of strain sensors to detect human motion. The research aims to simplify the process by using a laser to directly irradiate carbon-rich materials, eliminating multiple synthesis procedures, reducing the need for costly equipment and techniques, and decreasing both time and cost.

In order to accomplish the objectives of this project, three main areas need to be addressed:

- Determining the ideal parameters for producing LIG from PI involves optimizing laser power, scanning speed, and sensor patterns.
- Identifying the optimal substrate for the LIG sensor involves evaluating various materials such as PI film, polyurethane (PU) tape, protection tape, bandage, and polyethylene (PE) nonwoven tape. The goal is to select a substrate that exhibits mechanical and electrical properties suitable for biomedical sensing applications. These materials serve as independent variables in the assessment.
- Developing the capability for the strain sensor to detect physiological signals such as arterial pulse and human motion (finger bending, wrist rotation, knee bending) is the primary goal. If feasible, the sensor will also be designed to study other signals, including electrocardiography (ECG), electrooculography (EOG), and electromyography (EMG).

## **1.4.Scope and Limitation**

This project's scope is to streamline sensor production by implementing a low-cost, one-step fabrication method. The technology circumvents intricate procedures or apparatus, such as thermal vacuums or chemical doping. The laser machine used is a Laserscript-LS3040 Desktop, a tiny CO<sub>2</sub> laser system commonly found in laboratories and well-suited for a variety of applications.

The limits encompass financial restraints, which restrict the choice of materials and render costly testing procedures impractical. Consequently, other methods are required for sensor inspection. In addition, the study will focus on evaluating the electro-mechanical properties and applications of the sensors while excluding the assessment of other aspects, such as biocompatibility, due to time limitations.

## **1.5.Outline of Final Report**

The final report of this project is structured into five sections. The first section, Introduction, provides background information, outlines the problem statement, specifies the aims and objectives, and discusses the scope and limitations of the work. The second section, Literature Review, delves into LIG, covering its discovery, formation mechanisms, factors influencing LIG properties, and the morphology of sensors. It also explores sensor design considerations, precursor materials, and transfer substrates. Additionally, the review clarifies strain sensing mechanisms, performance metrics of strain sensor, and applications in healthcare signal detection.

Section 3 details the Materials and LIG Preparation, along with the examination of LIG-based strain sensors. This section provides experiment design and methods how sensor performance will be tested in this project. Section 4, Results and Discussion, presents the results. The final section, Conclusion and Further Work, summarizes the findings, discusses limitations encountered, and suggests avenues for future research.

## **2. LITERATURE REVIEW**

### **2.1. Introduction of LIG**

Graphene is a monolayer of carbon atoms arranged in a hexagonal lattice structure. The remarkable mechanical strength, electrical conductivity, and thermal stability of this material have prompted substantial research into several synthesis processes. The goal is to fully use its potential in a wide range of applications, including electronics and materials science.

Monolayer graphene was obtained by mechanical peeling. This exfoliation process entails attaching highly ordered pyrolytic graphite (HOPG) to scotch tape, which then sticks to the graphite. The graphite is gradually thinned by continuously applying and removing the tape, eventually reaching a transparent state [1]. This technique has the capability to generate graphene with a thickness of up to 100 nm, which includes sizable layers consisting of a single atom [2]. Despite its uncomplicated nature and minimum prerequisites, it exhibits a sluggish pace and requires significant manual effort.

Chemical vapour deposition (CVD), developed in 2006 [3], is a highly efficient method for producing graphene. It entails breaking down carbon sources from hydrocarbons in a high-temperature, high-vacuum environment. The process involves the deposition of carbon atoms in a gaseous form onto a medium, forming large graphene sheets that are well-suited for use in sensitive electronic devices [4]. Nevertheless, the high costs of equipment, substrate, and operational requirements impede this method's commercial feasibility, rendering it less economically viable compared to mechanical exfoliation.

In 2011, researchers developed a new chemical vapour deposition (CVD) method that uses propane gas as the carbon source. This method offers the advantage of attaining an ideal structure for graphene films while minimising the rate of development [5]. However, there are still significant challenges in minimising the possible harm to certain graphene parts during the transfer procedure [6].

### 2.1.1. Discover of LIG

James Tour's research team at Rice University discovered LIG while attempting to convert graphene oxide on a polyimide sheet using a CO<sub>2</sub> laser [8]. Surprisingly, the laser generated a charred area of a porous graphene network with less than five layers. The fortuitous discovery led to the creation of the term “laser-induced graphene,” which generated substantial enthusiasm and prompted additional investigation within the scientific community.

The LIG technology utilizes a CO<sub>2</sub> laser to generate elevated local temperatures, enabling the production of intricate patterns and developing a three-dimensional porous network structure. Furthermore, aside from CO<sub>2</sub> lasers, visible and ultraviolet lasers have proven to be effective in the synthesis of LIG [9]. Moreover, computer programs may readily facilitate pattern design, increasing the process's accuracy and adaptability.

Since its initial discovery, researchers have focused on improving the synthesis methods of LIG and exploring its various applications. The synthesized materials range from polyimide to commercial polymers, metal/plastic composites, and natural resources [10]. Researchers can produce functional composites with improved mechanical properties by integrating LIG into host materials, such as increased flexibility and stretchability.

### 2.1.2. Formation of LIG

Laser energy and polymer surfaces interact intricately to form LIG. Directing a laser beam at a polymer selectively absorbs energy at the irradiated spot, leading to localised decomposition, while the surrounding material remains relatively unaffected. This process is primarily driven by photothermal effects, especially when using long-wavelength lasers like CO<sub>2</sub> lasers in conjunction with PI [11]. However, photothermal and photochemical mechanisms can coincide, depending on the laser's fluence.

Photochemical delamination and photothermal carbonisation are the two main mechanisms involved. At lower laser fluences, photochemical reactions dominate. In this case, photons directly break chemical bonds with lower energies than the photons [12]. Conversely, at higher fluences, photothermal effects become more pronounced. Here, the absorbed photon energy induces atomic vibrations faster than the bond-breaking energy, leading to the carbonisation of the polymer [13, 14].

A theoretical framework incorporating key variables such as temperature, laser power, and polymer absorbance can understand the dynamics of LIG formation. Increasing the laser power or adjusting the scanning speed raises the average temperature of the irradiated area, enhancing the polymer's ability to absorb laser energy and facilitating efficient LIG formation. This optimisation can be achieved even with lower power densities [15]. As laser intensity increases, the interplay between photothermal and photochemical effects becomes more complex, illustrating the nuanced relationship between energy absorption and bond breaking in LIG synthesis.

## **2.2.Synthesis and Attribute Adjustment of LIG**

The synthesis process influences LIG's morphology, conductivity, and application versatility, which entails a diverse array of laser technologies and carbon-rich materials. The structural integrity and quality of graphene are affected by the different laser types and wavelengths [16–18]. The characteristics of LIG, such as porosity and electrical properties, are substantially affected by laser parameters such as power, scanning speed, and pulse frequency [21–24]. For their durability, thermal resistance, and conductivity, researchers almost always choose carbon-rich materials like PI and phenolic resin (PR). This means that LIG can be used in more areas, such as supercapacitors and sensors [10, 19, 25–26]. This review investigates the most effective synthesis methods and material selections to optimise LIG's performance in various applications.

### **2.2.1. Variety of laser technologies**

Based on the laser wavelengths, we can classify LIG into three primary categories: infrared, visible, and ultraviolet (UV). The CO<sub>2</sub> laser is the most popular LIG preparation option. It works at a wavelength of 10.6 μm. The infrared laser induces localised high temperatures, leading to the breakage of chemical bonds and subsequent recombination of carbon atoms. This process results in the production of porous LIG on the PI film [16].

In 2018, a UV laser with a wavelength of 355 nm and a pulse duration of 1 μs was used to achieve twice the spatial resolution as part of progress in LIG technology [17]. Moreover, LIG preparation has employed a range of lasers of varying wavelengths, including continuous-wave lasers functioning at 355 nm, 532 nm, and 1064 nm. The wide range of laser wavelengths means the LIG production technique can adapt to different laser sources [18].

The difficulty with laser energy is producing graphene at low power levels, frequently leading to insufficient graphene creation. On the other hand, increased power levels aid in the creation of graphene, but they also pose a potential threat to the integrity of the material's porous features. Hence, the laser's power is vital in influencing the shape of the resultant graphene. Studies have shown that when the products were exposed to a low laser fluence of  $4.4 \text{ J/cm}^2$ , their Raman spectra did not differ significantly from the original PI film. This suggests there was no carbonisation and only a small amount of graphene production occurred [8]. However, increasing the laser fluence to  $5.5 \text{ J/cm}^2$  led to the appearance of the characteristic 2D peak of graphene at  $2700 \text{ cm}^{-1}$  [21].

Furthermore, the laser flux  $\phi$  can be determined through a specific calculation

$$\phi = \frac{P}{\vartheta \cdot d} \quad (2.1)$$

where  $\phi$  is luminous flux,  $P$  is laser source power,  $\vartheta$  is scanning speed, and  $d$  is laser spot diameter [22]. This equation 2.1 underscores its critical role in determining the experimental parameters used in this study, including laser power and scanning speed.

Besides power and scanning speed, the number of scanning cycles and the frequency of a pulsed CO<sub>2</sub> laser also play critical roles in graphene synthesis. Research by Xing's team showed that with a laser power of 12.4 W, a pulse frequency of 20 kHz, and a scanning speed of 105 mm/s, varying the number of scanning cycles leads to different outcomes [23]. Images from an SEM (Figures 2-1a and 2-1b) showed that synthesised LIG with two scanning cycles made a porous structure that worked better than one cycle by creating more surface holes. However, despite an increase in the number of pores inside the LIG, its surface porosity remained consistently low after three or four cycles (Figures 2-1c and 2-1d). This lack of surface porosity is not advantageous for sensing applications.

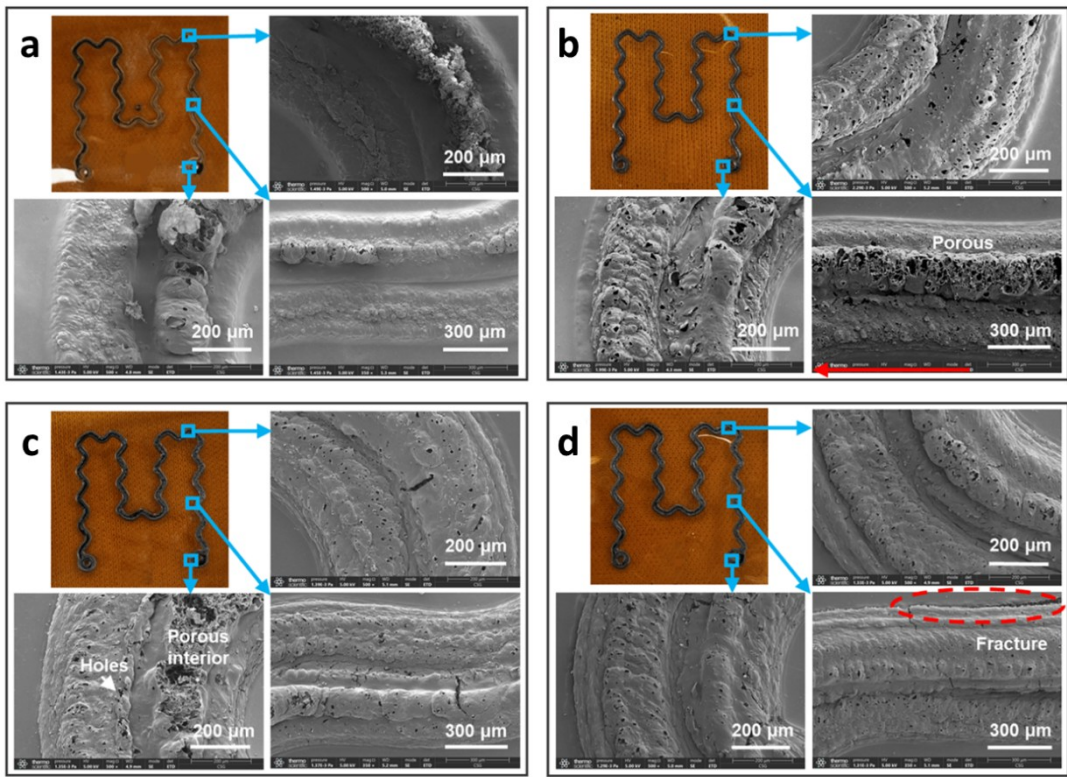


*Figure 2-1 SEM image of LIG morphology under different scanning cycles [46].*

- (a) Single scanning cycle.
- (b) Two scanning cycles.
- (c) Three scanning cycles.
- (d) Four scanning cycles.

Additionally, Wang's team observed that, after fixing the power, the electrical resistance of LIG (Figure 2-2a) remained high at lower frequencies but stabilised at higher frequencies, showing minimal morphological changes between 12 kHz and 20 kHz (Figures 2-2b-d) [24]. This highlights the frequency-dependent nature of LIG's electrical resistance, as described in equation 2.1. In contrast, Richard Group's study emphasises the need to assess laser power and scan speed simultaneously instead of focussing on individual optimisation.

Their machine-learning analysis revealed significant effects came from fifth-order terms related to scan speed and fourth-order terms pertaining to laser power [47]. This optimisation leads to lower sheet resistance, which improves electrode performance. Reduced sheet resistance enhances the sensitivity of humidity and strain sensors, allowing them to detect more minor environmental changes with greater accuracy [47, 48]. Additionally, lower resistance helps maintain signal integrity by reducing noise and interference in the sensor's circuitry, resulting in more precise and more reliable data. This is particularly important for high-frequency applications where signal clarity is crucial. Furthermore, sensors with lower sheet resistance are more energy-efficient because they offer less resistance to electrical current, thus consuming less power [48].

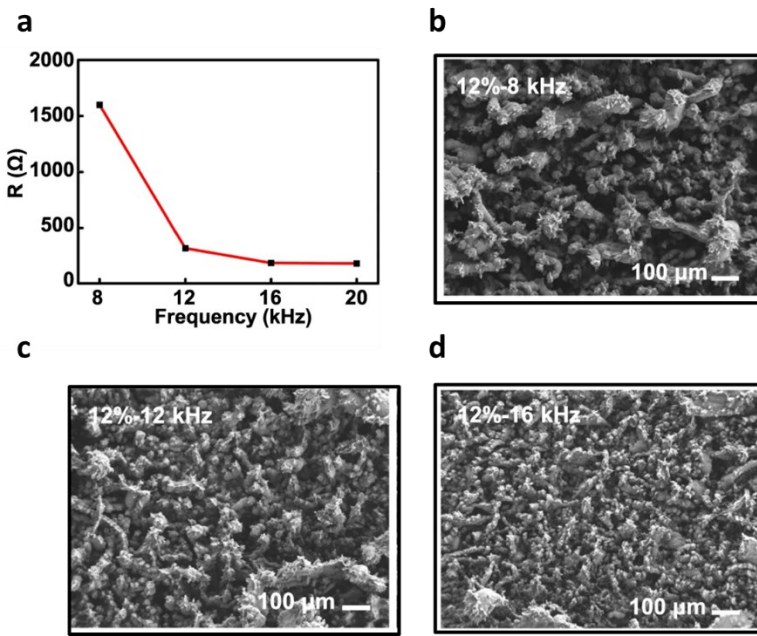


*Figure 2-2 Relationship between LIG resistance and frequency, alongside SEM images [24].*

- (a) Resistance variation with various frequency. (b) SEM image of LIG at 8 kHz.
- (c) SEM image of LIG at 12 kHz. (d) SEM image of LIG at 16 kHz.

### 2.2.2. Variety of carbon-rich materials

Carbon-rich materials, particularly polymers like PI, are used in LIG because of their capacity to endure heat, resist corrosion, and exhibit flexibility [19]. The careful selection of the precursor material is critical because it significantly impacts the shape, electrical conductivity, and contact area of the resultant Lithium-Ion Gate. LIG technology has grown and can now be used with more polymers, like thermosetting resin [10], polyetherimide (PEI) [11], polyether ether ketone (PEEK) [12], sulfonated polyether ether ketone (SPEEK) [13], and Kevlar [14]. Each of these materials' distinctive characteristics contribute to the improvement of LIG's performance and adaptability.

For instance, studies have shown that integrating aluminium nanoparticles into polyethylene terephthalate (PET) improves the electrical conductivity and mechanical stability of LIG. PET-based LIG has proven useful in applications such as thermal heaters, energy storage electrodes, bending sensors, and electrochemical sensors [36]. Similarly, PEEK is notable for its sensitivity, durability, wide operating range, and rapid response times, making it particularly effective in CLIG sensors. This versatility supports diverse applications and enables real-time monitoring of human movements [32, 34].

Further expanding the range of applications, SPEEK is employed in supercapacitors due to its uniform porous distribution of graphene [39]. Its functional composition enhances LIG/SPEEK's electrochemical performance by providing stable and high-capacitance charge-discharge cycles, making it a good choice for wearable supercapacitors [37]. This highlights the adaptability of LIG to various advanced energy storage technologies.

Similarly, textiles like Kevlar, known for their protective properties, are used in fabricating LIG. Flexible energy storage solutions for zinc use the resulting LIG/Kevlar composite, which offers a high open-circuit voltage and stable discharge characteristics. LIG/Kevlar can also be used as an accurate, selective, and stable NO<sub>2</sub> sensor that can pick up 100 ppm of NO<sub>2</sub> and as ECG electrodes to pick up P-waves, QRS complexes, and T-waves [40, 41]. This underscores the diverse applications of LIG in both energy storage and sensor technologies.

On a different front, phenolic resin (PR) emerges as a promising precursor for producing conductive LIG. PR offers advantages such as solubility, film-forming ability, high conductivity after conversion, and compatibility with various solvents and substrates. Moreover, doping PR with elements like boron and molybdenum allows for the creation of LIG with tailored properties. These features make PR-based LIG suitable for applications in supercapacitors and electrochemical sensors [35].

For materials with lower carbon content, a method involving repeated laser irradiations has been developed to enhance carbonization. This technique, which involves defocusing the laser to minimise temperature gradients, has successfully produced LIG from a variety of substances, including wood, plants, edibles, cellulose, and textiles. This method facilitates the recycling of waste materials into electronic components [25]. Table 2-1 summarizes possible carbon sources for forming LIG and their respective applications, providing an overview of LIG technology's range and versatility.

*Table 2-1 Laser induced graphene materials, process and applications.*

Materials	Type of Laser	Application	Refs
PI	10.6 $\mu\text{m}$ CO <sub>2</sub> laser	Micro supercapacitor, sensors, air filter	[10], [27]
	355nm UV laser	Strain sensor	[28]
	450nm laser diode	sound-sensing	[43]
	1064 nm infrared laser	Humidity sensor	[26]
PEI	10.6 $\mu\text{m}$ CO <sub>2</sub> laser	Strain sensor	[29]
PEEK	10.6 $\mu\text{m}$ CO <sub>2</sub> laser	Strain sensor	[32]
	10.6 $\mu\text{m}$ CO <sub>2</sub> laser	Pressure and strain sensors	[34]
SPEEK	10.6 $\mu\text{m}$ CO <sub>2</sub> laser	Supercapacitor	[37]
PPS	10.6 $\mu\text{m}$ CO <sub>2</sub> laser	Supercapacitor	[38]
Kevlar	10.6 $\mu\text{m}$ CO <sub>2</sub> laser	Batteries, ECG electrodes, NO <sub>2</sub> sensor	[40]
	1030 nm fibre laser	ECG electrodes and strain sensor	[41]
	1036 nm IR laser	Supercapacitor and temperature sensor	[45]
	348 nm UV laser	Strain sensor	[45]
PR	405 nm visible laser	Supercapacitor and electrochemical sensor	[35]
Papers	10.6 $\mu\text{m}$ CO <sub>2</sub> laser	Strain sensor	[30]
	355 nm UV laser	Humidity and temperature sensors	[31]
Woods and leaves	343 nm UV laser	Electronic interconnect and temperature sensor	[33]
Wood	10.6 $\mu\text{m}$ CO <sub>2</sub> laser	Supercapacitor	[42]
Silk	1064 nm fibre laser	Sensor	[44]

## 2.3. Strain Detection Using LIG-based Sensors

LIG is ideal for strain sensors due to its excellent electrical conductivity, mechanical flexibility, and simple fabrication. Its porous structure and large surface area enhance sensitivity and reliability in detecting mechanical deformations. These properties support applications in wearable electronics, structural health monitoring, and human motion detection. The next section covers LIG-based strain sensor synthesis, performance, and applications, showcasing their significant advancements and potential in various fields.

### 2.3.1. Strain sensing evaluation

The performance evaluation of stretchable strain sensors involves several critical parameters:

- 1) Sensitivity: The sensitivity is typically represented by the gauge factor (GF), which is determined by the slope of the curve plotting the relative change in resistance ( $\Delta R/R_0$ ) against the applied strain ( $\epsilon$ ). The GF is calculated using the equation:  $GF = (\Delta R/R_0) / \epsilon$ , where:
  - $R_0$  is the initial resistance without strain
  - $R$  is the resistance under strain
  - $\epsilon$  is the applied strain

Recent studies have shown that the conductive layer significantly influences sensitivity, with the tunnelling effect contributing to a larger increase in resistance compared to other mechanisms. For instance, Zhu et al reported a GF of 457 for their LIG-based strain sensor, which is significantly higher than many traditional metals foil strain gauges ( $GF \approx 2$ ) [48].

- 2) Stretchability: This parameter defines the maximum strain a sensor can withstand while remaining functional. It is particularly crucial for wearable healthcare devices that must accommodate skin deformation. Stretchability is often reported as a percentage, with some LIG-based sensors achieving stretchability up to 100% or more [49]
- 3) Linearity: The linearity of a sensor's response across its operating range is crucial for accurate measurements, as it simplifies calibration and data interpretation. A linear response ensures proportionality between the input and output. However, there is often a trade-off between achieving high sensitivity and maintaining linearity, as improving one can compromise the other. Balancing both factors is key to designing sensors that are both precise and responsive.
- 4) Response Time: Response time refers to how quickly a sensor can detect and react to changes in strain. Fast response times are essential for real-time monitoring applications. LIG-based sensors have demonstrated response times in the millisecond range [30, 32]. However, determining whether a sensor is truly real-time isn't solely dependent on the response time in the second range. It depends on the application; for example, when monitoring glucose levels, response times in the seconds range can still provide sufficient accuracy to track glucose concentration, as blood glucose levels don't change rapidly like ECG signals.
- 5) Durability: The ability of the sensor to maintain its performance over repeated cycles of strain is critical for long-term use. Some LIG-based sensors have shown stability over thousands or tens of thousands of strain cycles [30, 32]. This ensures reliable operation and durability in practical, real-world applications.

### 2.3.2. Fabrication techniques

The fabrication of LIG-based strain sensors typically involves the following steps:

- 1) Substrate Preparation: A PI film is commonly used as the starting substrate due to its thermal stability and flexibility.
- 2) Laser Irradiation: A CO<sub>2</sub> infrared laser is used to selectively irradiate the PI film. The laser parameters (power, speed, and focus) are optimized to achieve the desired LIG structure. Multiple scanning cycles may be employed to enhance the graphene quality.
- 3) Pattern Design: The laser path can be programmed to create specific patterns, allowing for customized sensor designs tailored to different applications.
- 4) Transfer Process: For improved stretchability, the LIG pattern is often transferred onto a stretchable substrate. This can be achieved through various methods:
  - Direct transfer using adhesive tapes
  - Wet transfer using a PMMA support layer
  - In-situ formation on stretchable substrates
- 5) Encapsulation: To protect the LIG and improve durability, sensors are often encapsulated with a thin layer of stretchable material like PDMS.

Recent advancements in fabrication techniques have resulted in significant improvements in sensor performance. For instance, selecting the correct power and scanning speed during the laser processing of LIG-PI can lead to a higher performance, with LIG-PI achieving a GF of 228.5, whereas films processed with other power settings typically result in a GF around 50 [50].

### 2.3.3. Applications of strain sensors in Health Monitoring

LIG-based strain sensors have shown remarkable potential in various health monitoring applications:

#### 1) Cardiovascular Monitoring:

- Pulse Detection: As shown in Figure 2-3a, LIG sensors can detect wrist pulses with high precision. This capability allows for the capture of photoplethysmogram (PPG) signals, which are used to calculate heart rate and assess blood flow dynamics.
- Blood Pressure Estimation: By combining pulse transit time measurements from multiple body locations, some researchers have demonstrated the potential for non-invasive blood pressure estimation using LIG sensors [51].

#### 2) Respiratory Monitoring:

LIG sensors are promising for respiratory and airflow monitoring due to their flexibility and customizable design. A conical microdot array 3D structure provides a fast response under 60 ms and a low detection limit of 11.4 Pa [52]. Additionally, graphene-based strip-line face masks with strain sensors can detect normal and abnormal breathing rates, enhancing real-time respiratory monitoring [53].

#### 3) Human Motion Detection:

Large-scale Movements: As illustrated in Figures 2-3c and 2-3d, LIG sensors can detect hand grips and finger bending. This capability is valuable for rehabilitation monitoring and human-machine interfaces.

#### 4) Ocular Monitoring:

Figure 2-3b demonstrates the sensor's ability to detect electrooculography (EOG) signals from eye blinking. This application could be useful for monitoring fatigue or developing assistive technologies for individuals with limited mobility.

#### 5) Sweat Analysis:

Recent developments have integrated LIG-based strain sensors with electrochemical sensors to create multifunctional patches for monitoring body movement and sweat composition. The LIG-based sensor, combined with a flexible printed circuit board and a custom Android application, enables real-time, *in situ* monitoring of pH, Na<sup>+</sup>, and K<sup>+</sup> levels in sweat [54].

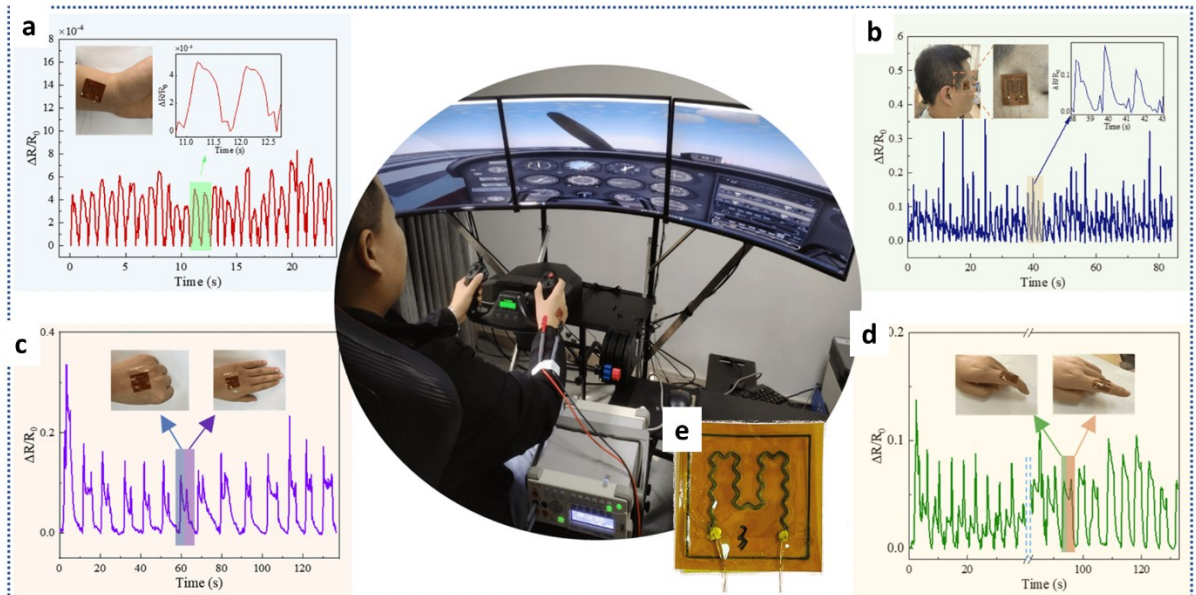


*Figure 2-3 LIG-based strain sensors for human motion detection [46].*

- (a) Pulse detection (b) Blink detection. (c) Hand holding and stretching detection
- (d) Finger bending detection, and (e) LIG-based strain sensor.

#### 2.3.4. Current Challenges and Future Directions

Despite the significant progress in LIG-based strain sensors, several challenges remain:

- 1) Long-term Stability: Ensuring consistent performance over extended periods, especially under repeated strain cycles and varying environmental conditions, remains a challenge.
- 2) Sensitivity-Stretchability Trade-off: While progress has been made, further improvements in achieving both high sensitivity and high stretchability are needed for certain applications.
- 3) Signal Processing and Noise Reduction: As these sensors are often used to detect subtle physiological signals, advanced signal processing techniques are required to filter out noise and motion artifacts.
- 4) Biocompatibility and Skin Adhesion: For long-term wearable applications, improving the biocompatibility of materials and developing skin-friendly adhesives that maintain sensor performance are crucial.
- 5) Energy Efficiency: Developing self-powered or low-power consumption LIG-based sensors is an important direction for enabling long-term, continuous monitoring.

In conclusion, LIG-based strain sensors represent a promising technology for health monitoring applications. Their unique combination of high sensitivity, flexibility, and ease of fabrication positions them as a key enabling technology for the next generation of wearable health devices. As research in this field continues to advance, we can expect to see increasingly sophisticated and integrated systems that leverage the capabilities of LIG sensors to provide comprehensive, real-time health monitoring solutions.

### **3. EXPERIMENTAL METHODOLOGIES**

#### **3.1. Materials and Preparation**

##### **3.1.1. LIG Fabrication Parameters**

The LIG fabrication process was optimized through systematic variation of key laser parameters. A CO<sub>2</sub> laser system (Laserscript-LS3040 Desktop, HPC Laser Ltd, UK) operating at a wavelength of 10.6 μm was utilized for LIG fabrication on PI sheets (thickness: 75 μm, Kapton HN, DuPont, RS Components, UK) under ambient conditions. The position was secured with masking tape (3M SCOTCH 101E Beige, RS Components, UK). The following parameters were investigated:

- 1) Laser Power: A range from 10% to 30%, with increments of 5%, was explored. This range was selected based on literature review, ensuring sufficient energy for graphene formation while avoiding substrate damage.
- 2) Scanning Speed: Speeds varied from 100 mm/s to 400 mm/s, with 100 mm/s increments. This wide range allowed investigation of the trade-off between fabrication speed and LIG quality.

According to Equation 2.1, laser flux, calculated from laser power, laser spot diameter (120 μm), and scanning speed, significantly influences LIG morphology. The minimum laser flux occurred at 5% power and a speed of 400 mm/s, resulting in a laser fluence of 3.64 J/cm<sup>2</sup>. Conversely, the maximum laser flux occurred at 30% power and a speed of 200 mm/s, producing a fluence of 48.75 J/cm<sup>2</sup>. Review findings suggest that carbonization of LIG using a CO<sub>2</sub> laser necessitates a fluence of 5.5 J/cm<sup>2</sup>. Therefore, at 5% power, carbonization will likely not occur on the LIG surface due to insufficient laser fluence.

3) Pattern Design: Four distinct patterns were investigated for their impact on sensor performance:

- Square pattern
- Shutter pattern
- Serpentine pattern
- Zigzag pattern

Each pattern was designed to explore different aspects of sensor functionality, such as strain sensitivity, directional response, and overall flexibility. The patterns were designed using computer-aided programs like CorelDraw and then imported to LightBurn for engraving and cutting. The length of the sensor is controlled to be 23 mm, and the width is controlled to be 10 mm for every pattern. Chapter 4 will present all evaluated patterns, while this chapter will showcase one representative pattern for each category: square, shutter, Serpentine, and zigzag, as shown in Figure 3-2.

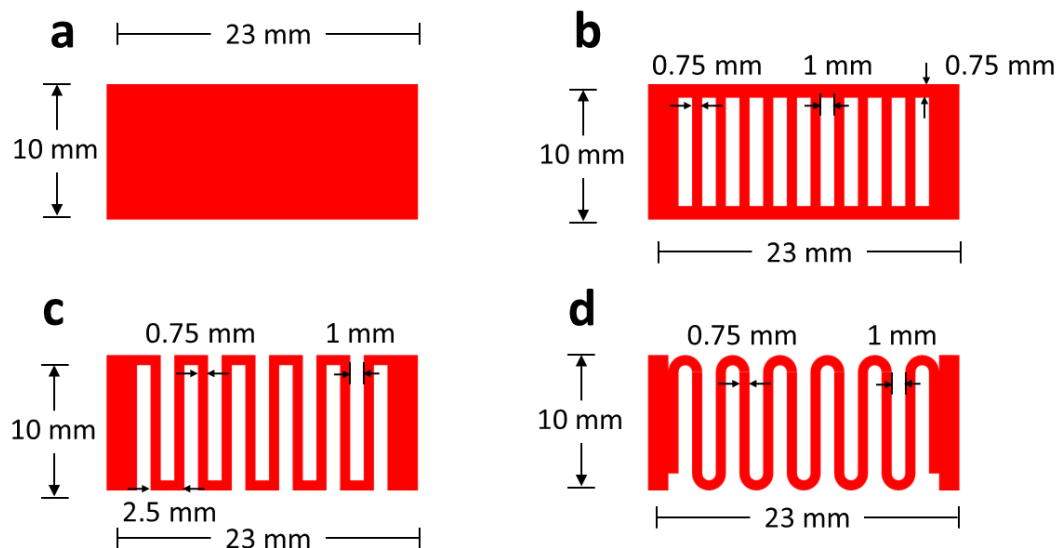


*Figure 3-1 LIG Strain sensor patterns.*

### 3.1.2. Transfer Materials

This study investigated four distinct transfer materials to enhance the performance of LIG strain sensors:

- 1) Silicone protection tape
- 2) PE nonwoven medical tape (4076 Extended-Wear Medical Tape, Digi Key, UK)
- 3) PU tape (3M 8671HS, Self Adhesive Supplies, UK)
- 4) Bandage

Each material was selected based on specific properties and potential to improve sensor performance.

The silicone protection tape offers excellent flexibility and durability, crucial for wearable applications. With a thickness of approximately 3 mm, this material presents an interesting test case for sensor integration.

PE nonwoven medical tape provides breathability and skin-friendliness, essential for long-term health monitoring applications. The tape measures 101.60 mm in width and 9.1 m in length, with a polyester nonwoven backing 0.254 mm thick. The breathable, soft, and flexible nature of this material, similar to ECG electrode substrates, combined with its single-sided adhesive property, allows direct contact for pattern transfer.

PU tape combines elasticity with water resistance, potentially enhancing sensor stability in various environments. The tape dimensions are 50 mm x 1 m (width x length) with a thickness of 0.35 mm. It exhibits a tensile strength of 1,401 N/100 mm and 500% elongation at break. The single-sided adhesive nature of this tape facilitates graphene transfer from polyimide substrates, making it an intriguing option despite its relatively high cost per unit area.

The bandage material was selected for its comfort and ease of application, potentially facilitating integration into existing medical practices. This material offers advantages in terms of elongation and stretchability; however, the process of transferring graphene to this substrate presents significant challenges.

A comparative analysis of these materials was conducted to determine their effects on sensor performance, focusing on aspects such as adhesion to the LIG, electrical resistance, flexibility, and impact on sensor sensitivity. The results of this analysis will be presented and discussed in detail in Section 4. To illustrate this, Figure 3-2 shows the percussion material, PI, and the transfer materials, which aim to improve the performance of the LIG-based strain sensor.

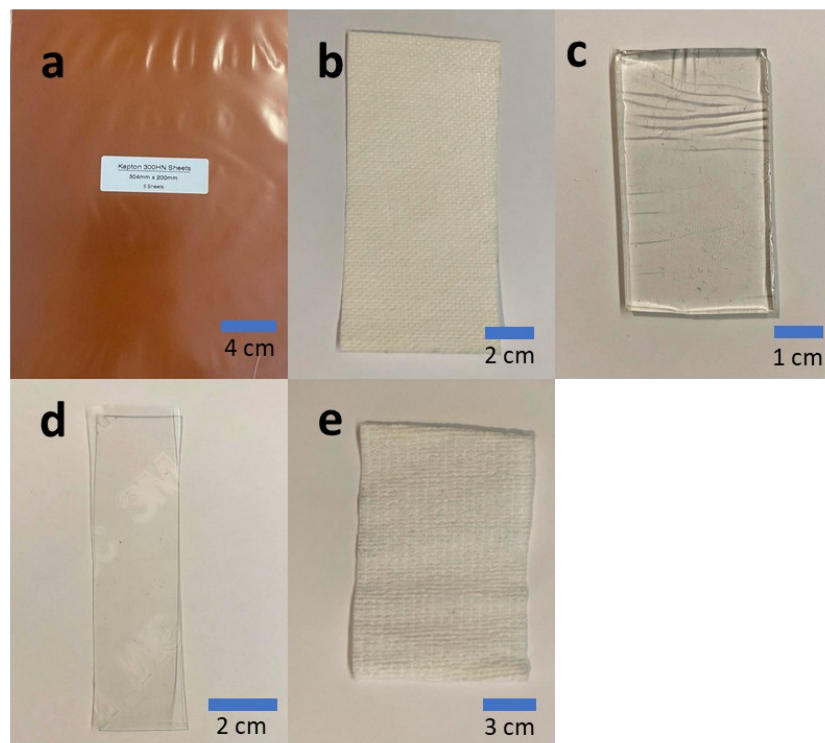


*Figure 3-2 Precursor material and transfer materials.*

- (a) *Kapton HN PI film*, (b) *PE nonwoven medical tape*,  
(c) *protection tape*, (d) *PU tape*, and (e) *bandage*.

Table 3-1 lists the materials used in this experiment. PI film and tapes are utilized for LIG strain sensor synthesis, while silver paste and copper wire serve as connectors and electrodes. An ECG monitoring add-on interface is used as the receiving module for human signals.

*Table 3-1 Materials used in the experiment.*

Materials	Description	Purchase from
Commercial PI film	Kapton HN thermal insulating film - 75 µm in thickness (£105)	RS Components
Medical tape	Spunlace extended wear nonwoven tape - 254 µm in thickness (£25)	Digi Key
PU tape	3M 8671HS – 350 µm in thickness (£10)	Self Adhesive Supplies
Bandage	Standard fabric bandage for medical use	Not available
Silicone protection tape	Silicone tape used for providing protection	Not available
Tape	Masking tape - 120 µm in thickness (£5)	RS Components
Silver paste	Electrolube Silver Conductive Lacquer for Electronics (£19)	Onecall (Farnell & CPC)
Copper wire	0.15 mm Copper wire (£13)	Onecall (Farnell & CPC)
ECG monitoring sensor	DFROBOT SEN0213, Digital interface (£19)	Onecall (Farnell & CPC)

## **3.2.Design and Characterization of LIG Strain Sensors**

The characterization of LIG strain sensors primarily involved measuring their electrical resistance under varying bending conditions, with particular attention to the sensor's initial resistance. The initial resistance is a critical parameter, as excessively high resistance can result in increased power consumption, while lower resistance helps preserve signal quality by reducing noise and minimizing interference within the system. Due to the complexity of strain distribution during bending, direct strain measurement and gauge factor calculation were not feasible. Consequently, a systematic methodology was developed to evaluate sensor performance based on changes in resistance.

### **3.2.1. Resistance Measurement Setup**

A voltage divider circuit was employed to measure the resistance of the LIG sensors. This circuit included the LIG sensor as one resistor and a known reference resistor. The reference resistance was selected based on the sensor's initial resistance: if the initial resistance was below  $1\text{ k}\Omega$ , a  $1\text{ k}\Omega$  resistor with a 5% tolerance was used. The voltage across the reference resistor was measured, and the LIG sensor's resistance was calculated using Ohm's law. To ensure suitability for wearable applications, the circuit operated at a low input voltage of 5V, minimizing power consumption.

### **3.2.2. Bending Test Methodology**

To evaluate the sensor's response to bending, tests were conducted under different bending radii. The sensor was bent to form a curved shape, simulating the range of deformations expected in wearable applications, such as finger joint movement.

The test involved the following bending radii: flat (sensor length of 2.3 cm), 1.25 cm, 1 cm, 0.75 cm, 0.5 cm, 0.25 cm, and flat again, with decrements of 25 mm between each radius. This range was chosen to cover a variety of potential applications, from small joints to larger body parts.

For each bending radius, the following steps were performed:

- 1) Measure the initial resistance ( $R_0$ ) when the sensor is flat and at its initial length of 23 mm.
- 2) Compress the sensor to the desired bending radius.
- 3) Continuously measure the resistance ( $R$ ) for 30 seconds while the sensor is bent.
- 4) Return the sensor to the flat position and allow it to stabilize for 30 seconds.
- 5) Repeat steps 2-4 five times for each bending radius to assess repeatability.

### 3.2.3. Continuous Bending Test Method

The continuous bending test followed a similar procedure to Section 3.2.2 but omitted the 30-second stabilization in step 4. This aimed to simulate real-world conditions, such as monitoring continuous movements as described by Xing et al.

### 3.2.4. Data Acquisition and Processing

Data acquisition was carried out using a National Instruments (NI) USB-6001 system with a sampling rate of 1000 Hz. This high sampling rate allowed for detailed observation of transient resistance changes during bending and unbending events. The system's 14-bit resolution ensured precise resistance measurements. The software utilized for data acquisition is FlexLogger.

The measured voltage data was converted back to resistance using Ohm's law, based on the voltage divider circuit described in Section 3.2.1. A MATLAB-based signal processing pipeline was implemented to enhance data quality:

- 1) Notch Filter: Applied to eliminate 50 Hz power line interference.
- 2) Median Filter: Used to remove sporadic spikes or outliers.
- 3) Outlier Removal: Any remaining noise or spikes deviating significantly from the median were discarded.

After filtering, the average resistance over each 30-second bending period was calculated, along with the standard deviation to quantify the measurement's stability.

### 3.2.5. Performance Metrics

As direct strain measurement was not feasible, performance metrics were based on changes in electrical resistance:

- 1) Relative Resistance Change ( $\Delta R/R_0$ ): This metric quantifies the percentage change in resistance of the sensor due to bending. It is defined as  $\frac{(R-R_0)}{R_0}$ , where R represents the average resistance measured during bending and  $R_0$  denotes the initial resistance when the sensor is flat. This measure is used to assess how significantly the resistance deviates from its baseline value under various bending conditions.
- 2) Sensitivity to Bending (S): Quantified as the change in relative resistance per unit curvature, calculated as  $S = \left( \frac{\Delta R/R_0}{1/r} \right)$  where r is the bending radius. This metric reflects how resistance changes in response to varying degrees of curvature applied to the sensor.
- 3) Repeatability: Repeatability assesses the consistency and reliability of the sensor's performance across multiple measurements. It can be calculated by computing the coefficient of variation (CV) for resistance measurements taken at each bending radius. The CV is defined as the ratio of the standard deviation ( $\sigma$ ) to the mean ( $\mu$ ) of the resistance measurements, expressed as  $CV = \frac{\sigma}{\mu} \times 100\%$ . Lower CV values indicate greater repeatability and stability in the sensor's performance.
- 4) Response Time: Defined as the time taken for the sensor to reach 90% of its final resistance value during bending. This metric is crucial for evaluating how promptly the sensor responds to environmental changes.

### 3.2.6. Limitations and Considerations

While the characterization method provides valuable insights, several limitations should be acknowledged:

- 1) The bending tests create a complex strain field that is not uniform across the sensor surface.
- 2) The actual strain experienced by the graphene layer cannot be directly measured without advanced modelling techniques.
- 3) Performance metrics such as sensitivity to bending are specific to this test setup and may not be directly comparable to standard strain gauge factors.
- 4) Despite these limitations, the chosen methodology offers a consistent and repeatable approach for evaluating LIG-based strain sensors, particularly for wearable technology applications.

### **3.3.Evaluation of Sensor Performance for Health Applications**

In the absence of commercial devices for direct comparison, a robust methodology was developed to evaluate the performance of LIG strain sensors in three physiological applications: finger bending monitoring, hand grip measurement, and pulse detection. Additionally, LIG-based ECG electrodes were designed and tested.

#### **3.3.1. Finger Bending Monitoring**

The LIG sensor was attached to a flexible substrate worn on the finger joint. Resistance changes were recorded as the finger was bent at predefined angles: 0° (straight), 30°, 45°, and 90° (fully bent).

Evaluation metrics:

- 1) Sensitivity: Calculated as the change in resistance ( $\Delta R/R_0$ ) per degree of bending.
- 2) Repeatability: Assessed by the CV for 10 repeated measurements at each angle.

#### **3.3.2. Hand Grip Measurement**

The LIG sensor was integrated on a hand to measure and evaluate the sensor's response to high-force actions, assessing its functionality and reliability under such conditions.

### 3.3.3. Pulse Detection

The LIG sensor was placed on the wrist over the radial artery. To ensure consistent pressure, a bandage wristband was used to hold the sensor in place.

Evaluation metrics:

- 1) Pulse detection accuracy: Compared the number of pulses detected by our sensor with those counted manually using the traditional palpation method over a 60-second period.
- 2) Waveform consistency: Assessed the similarity of pulse waveforms across multiple measurements using cross-correlation analysis.
- 3) Accuracy, Selectivity, Specificity, and Positive predictivity were calculated to further evaluate sensor performance.

### 3.3.4. ECG Electrode Design and Evaluation

LIG electrodes were fabricated in a circular pattern with a diameter of 12 mm and a fractal-like pattern with an outer diameter of 12 mm and an inner diameter of 8 mm, as shown in Figure 3-3. These electrodes were integrated onto the body according to Einthoven's triangle derivation for easy application. The hole in the middle of each electrode is designed for a snap connector to connect to the ECG sensor cable. The performance of these electrodes was compared with commercial electrodes. Both the LIG ECG electrodes and the Ag/AgCl commercial electrodes were connected to the DFROBOT SEN0213, which incorporates an AD8232 chip.

Evaluation metrics:

- 1) Accuracy, Selectivity, Specificity, and Positive predictivity were calculated to analysing the clarity of key ECG features (P wave, QRS complex, and T wave).
- 2) Waveform consistency: Assessed the similarity of pulse waveforms across multiple measurements using cross-correlation analysis.

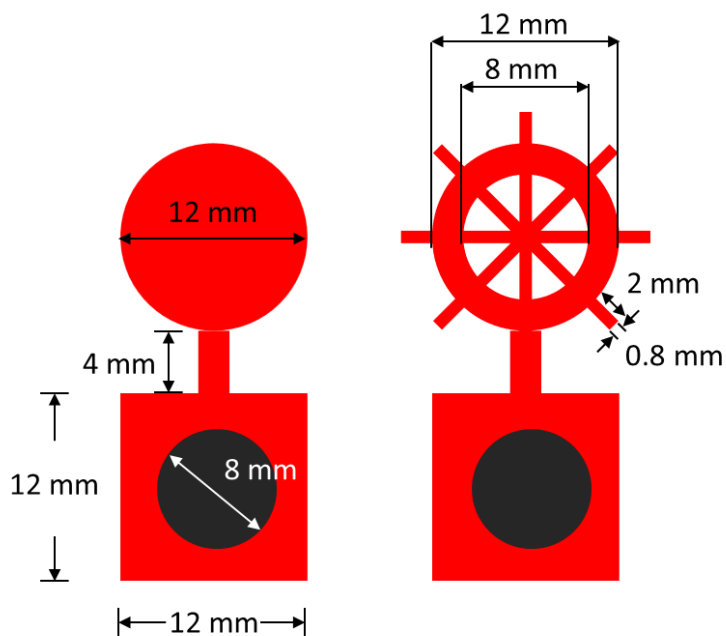


*Figure 3-3 ECG electrode patterns.*

*Right – Circular pattern, Left – Fractal-like pattern, Black – Hole*

In the signal recording for healthcare applications, data will be analysed in MATLAB. The analysis begins by filtering high-frequency noise using wavelet decomposition and reconstruction. A Daubechies wavelet of order 6 is employed, with the wavelet decomposition performed at level 5. Following this, the signal is processed through a high-pass filter with a cutoff frequency of 0.5 Hz, using an 8th-order infinite impulse response (IIR) filter (highpassiir). This step helps to maintain a stable baseline level.

Peak analysis is then conducted to detect uptrends and downtrends in the signal, highlighting voltage changes resulting from variations in resistance due to motion, bending, or pulse signals.

### 3.3.5. Metrics in Classification

To evaluate the sensors' performance in detecting specific physiological events, the following classification metrics were used:

- 1.) Accuracy is one of the most straightforward metrics. Accuracy defined as the proportion of correct predictions among the total number of cases examined. It provides an overall measure of how often the classifier is correct across all outcomes. Accuracy can be calculated by:

$$\text{Accuracy} = \frac{(TP + TN)}{(TP + TN + FP + FN)}$$

While accuracy offers a general performance overview, it can be misleading in cases of imbalanced datasets where one class significantly outnumbers the other.

- 2.) Sensitivity (Se), also known as recall or true positive rate, focuses on the model's ability to correctly identify positive cases. Sensitivity defined as the proportion of actual positive cases correctly identified by the model or test. Sensitivity can be calculated by:

$$Se = \frac{TP}{(TP + FN)}$$

- 3.) Specificity (Sp) measures the model's ability to correctly identify negative cases. Specificity defined as the proportion of actual negative cases correctly identified by the model or test. Specificity can be calculated by:

$$Sp = \frac{TN}{(TN + FP)}$$

4.) Positive Predictive Value (PP), also known as precision, focuses on the reliability of positive predictions. PP defined as the proportion of positive results that are true positives. PP can be calculated by:

$$PP = \frac{TP}{(TP + FP)}$$

PPV is particularly important in contexts, where acting on false positives could be costly or harmful.

### 3.3.6. Comparative Analysis

To evaluate the performance of the sensors for comparison, the following strategies were employed:

- 1) Literature Benchmarking: Results were compared with published data on similar sensors, while acknowledging methodological and material differences.
- 2) Statistical Analysis:
  - Paired t-tests were used to compare the LIG sensor performance with manual measurements or commercial electrodes.
  - One-way ANOVA was employed to determine if differences in sensor performance across applications were significant.
- 3) Repeatability and Reliability: Each test was repeated at least five times per application. Means, standard deviations, and 95% confidence intervals were calculated to quantify result variability and reliability.

## 4. RESULTS AND DISCUSSION

### 4.1. Influence of Power and Scanning Speed on LIG Performance

The influence of laser power and scanning speed on the formation of LIG was studied using a CO<sub>2</sub> laser engraving system with a maximum power of 35W. The experimental setup, depicted in Figure 4-1a, shows the process in which PI film is exposed to different combinations of laser power and scanning speed. These parameters were varied to optimize the quality and electrical conductivity of the resulting LIG.

#### 4.1.1. Preliminary Experimental Setup

The laser parameters were systematically varied as follows:

- The scanning speed was set at 200 mm/s in the top row, 300 mm/s in the second row, and 400 mm/s in the third row.
- Across these rows, the power increased from 10% to 30% in increments of 5% from left to right.
- The bottom row maintained a speed of 400 mm/s, with power settings of 5%, 7.5%, 6%, and 5.5% from left to right.
- A blank PI segment was positioned in the lower right corner of the arrangement to serve as a control.

#### 4.1.2. Preliminary Results and Discussion

Figure 4-1b presents the resulting LIG samples. Detailed observations include:

High power: LIG samples generated at 30% power with scanning velocities of 200 mm/s and 300 mm/s exhibited substantial damage as a result of excessive laser exposure. Furthermore, samples generated at a power level of 25% and a scanning speed of 200 mm/s also exhibited indications of damage.

Moderate power, low speed combinations: The LIG sample generated at a power of 20% and a scanning speed of 200 mm/s exhibited some lines that were destroyed, while other lines remained structurally intact and could be utilized for resistance measurements.

Low power, high speed combinations: LIGs generated at 5% and 5.5% power, with a scanning speed of 400 mm/s, exhibited poor carbonization due to inadequate exposure to laser energy.

Optimal parameter range: Other samples showed the expected carbonization characteristic of LIG sensors. When comparing samples at the same speed, areas with higher power had a more pronounced blackened appearance than those with lower power. Similarly, at the same power level, areas with slower scanning speeds were more extensively blackened because the laser lingered longer, resulting in more material burn.

These findings highlight the critical influence of laser parameters on the quality and integrity of LIG synthesis. A clear correlation emerged between laser parameters and LIG quality. At constant speed, higher power resulted in more pronounced blackening. At constant speed, higher power resulted in more pronounced blackening.

Moreover, to assess the precision of the laser cutting machine, Figure 4-1b shows a LIG pattern with four straight lines separated at various y-axis lengths. Each line is spaced 1 mm, 2 mm, or 3 mm apart to establish the cutting machine's minimum reliable distance. For this small laser cutting machine, the y-axis spacing must be at least 2 mm to accurately function and assess the machine's precision in making minimal gaps between engraved lines.

**a**

Speed 200 Power 10%	Speed 200 Power 15%	Speed 200 Power 20%	Speed 200 Power 25%	Speed 200 Power 30%
Speed 300 Power 10%	Speed 300 Power 15%	Speed 300 Power 20%	Speed 300 Power 25%	Speed 300 Power 30%
Speed 400 Power 10%	Speed 400 Power 15%	Speed 400 Power 20%	Speed 400 Power 25%	Speed 400 Power 30%
Speed 400 Power 5%	Speed 400 Power 7.5%	Speed 400 Power 6%	Speed 400 Power 5.5%	PI

**b**

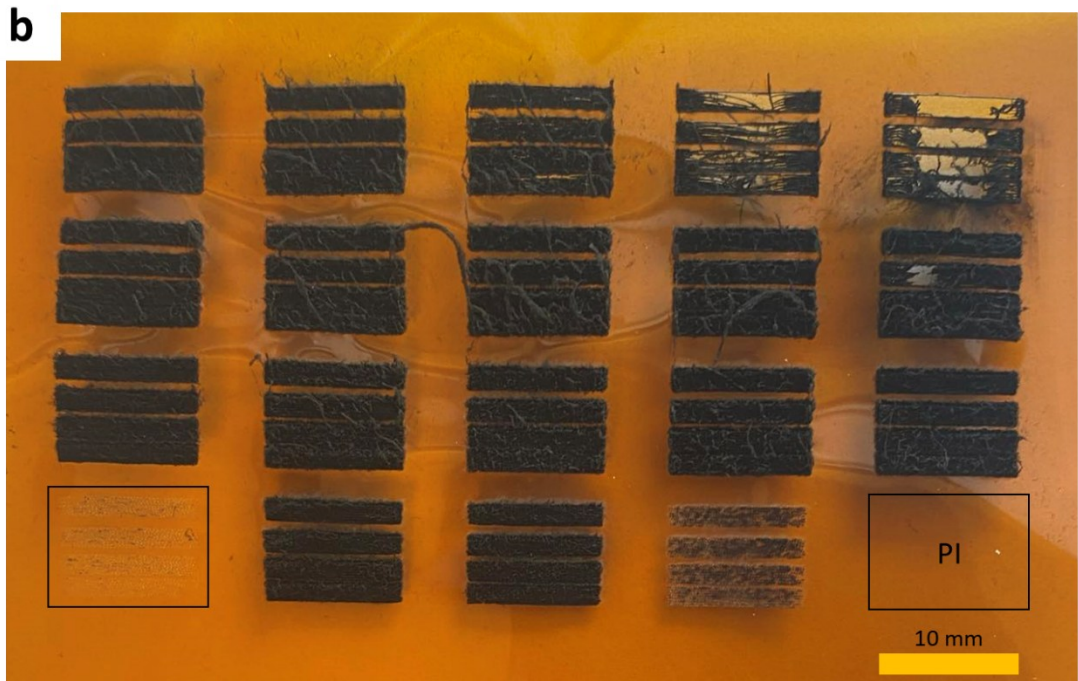


*Figure 4-1 Photograph of LIG and layout with different laser power and scanning speed.*

- (a) Layout of LIG with their power and scanning speed,
- (b) Photograph of LIG samples.

#### 4.1.3. Verification and Resistance Measurements

A second fabrication process was carried out to verify the consistency of the results and ensure accurate resistance measurements, as shown in Figure 4-2. In this step, at least three samples were fabricated for each combination of power and scanning speed. This repetition aimed to verify the consistency of previous results and to accurately measure the resistance of the samples. Key findings include:

Samples fabricated at laser powers of 5% and 5.5% exhibited inadequate carbonization, characterized by insufficient blackened areas on the PI substrate, as observed in the left column of Figure 4-2b.

In contrast, at a power level of 25% and a scanning speed of 200 mm/s, the excessive power caused damage to the PI substrate, leading to partial destruction.

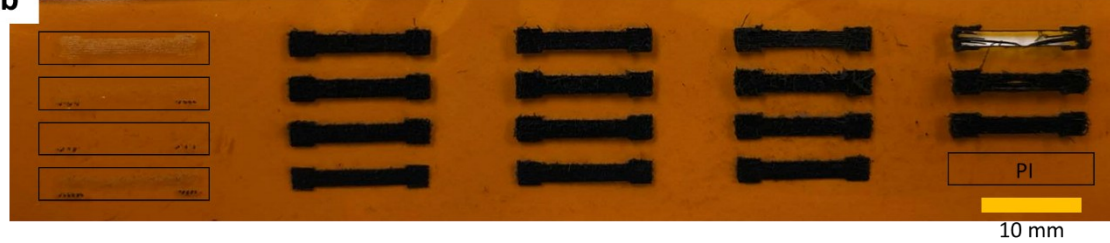
LIG samples created with laser powers between 10% and 20% achieved satisfactory carbonization, as depicted in the second to fourth columns of Figure 4-2b. These results are consistent with those shown in Figure 4-1b. However, in this experiment, LIGs formed at 20% power and a scanning speed of 200 mm/s did not exhibit any signs of damage.

Unexpectedly, faster scanning speeds resulted in more burnt carbon ash on the PI sheet, despite reducing the laser intensity. Conversely, slower scanning speeds produced less carbon ash. At a similar laser fluence of  $29.17 \text{ J/cm}^2$ , the LIG formed at 100 mm/s with 10% power exhibited a blackened area comparable to that of LIG formed at 200 mm/s with 20% power. However, the LIG at 100 mm/s and 10% power generated less carbon ash.

Tactile examination revealed that touching the LIG formed at 100 mm/s and 10% power left no black carbon residue on the finger, whereas touching the LIG formed at 200 mm/s and 20% power resulted in noticeable black carbon transfer. These observations suggest that lower scanning speeds with proportionally reduced power settings may achieve an optimal balance between effective LIG formation and minimal carbon ash production, potentially yielding more stable and cleaner LIG structure.

**a**

Speed 200 Power 5%	Speed 200 Power 10%	Speed 200 Power 15%	Speed 200 Power 20%	Speed 200 Power 25%
Speed 300 Power 5%	Speed 300 Power 10%	Speed 300 Power 15%	Speed 300 Power 20%	Speed 300 Power 25%
Speed 400 Power 5%	Speed 400 Power 10%	Speed 400 Power 15%	Speed 400 Power 20%	Speed 400 Power 25%
Speed 400 Power 5.5%	Speed 400 Power 6%	Speed 400 Power 7.5%	Speed 400 Power 8.5%	PI

**b**

*Figure 4-2 Photograph of LIG and layout with power from 5% to 25% and scanning speed from 200 mm/s to 400 mm/s.*

(a) Layout of LIG with their power and scanning speed and (b) Photograph of LIG

#### 4.1.4. Resistance Analysis

Three samples for each power and scanning speed combination were examined, and the resistance measurements for the LIG samples are summarized in Figure 4-3. A detailed analysis revealed the following:

- 1) Within the power range of 15% and 20% at a scanning speed of 400 mm/s, the resistance values showed no significant variation.
- 2) At a power of 10%, the resistance values at scanning speeds of 300 mm/s and 400 mm/s overlapped.

Statistical analysis using the F-test and t-test for observation 1 confirmed that there are no significant differences in the means of the samples, indicating consistency across different experimental conditions. However, for observation 2, the F-test and t-test revealed that the mean resistance at 400 mm/s with 10% power is statistically higher than that at 300 mm/s with 10% power, with a 95% confidence level.

Based on the observed carbonization quality and resistance consistency, the following parameters were identified as optimal for strain sensor analysis:

- At a scanning speed of 100 mm/s, a laser power of 10% will be used.
- For a scanning speed of 200 mm/s, the laser power should be set to 15% and 20%.
- At a scanning speed of 400 mm/s, a laser power of 20% will be employed.

These conditions are selected based on the observed carbonization quality and resistance consistency, ensuring effective performance of the strain sensors.

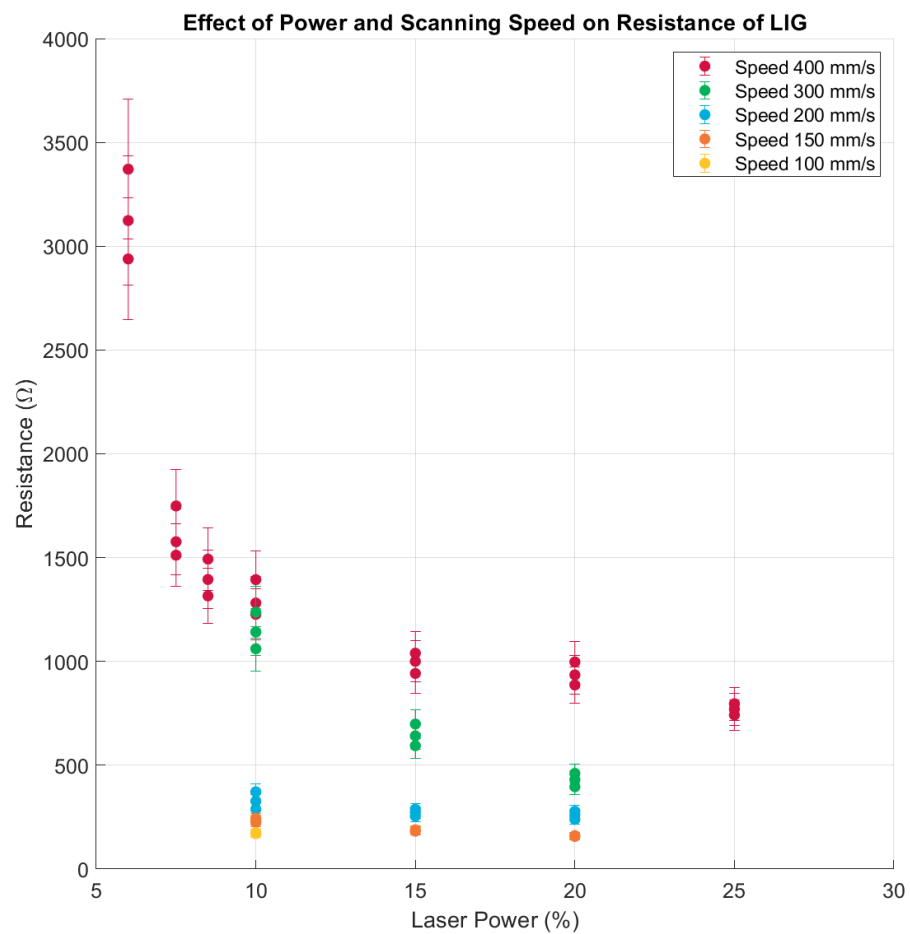


Figure 4-3 LIG Resistance with different laser power and scanning speed.

## **4.2.Influence of Sensor Pattern on LIG Performance**

The second objective of this research endeavour is to elucidate the impact of different sensing pattern on the performance characteristics of LIG sensors. Figure 4-4 (a-d) illustrates four distinct pattern geometries: square, shutter, Serpentine, and zigzag, each defined by specific morphological parameters, including finger quantity, inter-finger spacing, and finger width. A detailed summary of these pattern characteristics is presented in Figures 4-4 (e-f). The sheet resistance measurements for each pattern configuration were obtained using the four-point probe method and are documented in Table 4-1.

### **Challenges in the Pattern Transfer Process**

The transfer of patterns from the PI film to flexible substrates presents several challenges, primarily due to the intrinsic physical properties of the carbon material used in LIG formation. The narrow gaps between fingers in the shutter (sh1, sh2, and sh3) and zigzag (z1, z2, and z3) patterns are particularly prone to expansion during the transfer process. This expansion can result in a loss of pattern fidelity, causing these designs to morph into shapes that resemble square patterns, thereby compromising the intended geometric integrity of the sensors.

### **Selection of Representative Patterns**

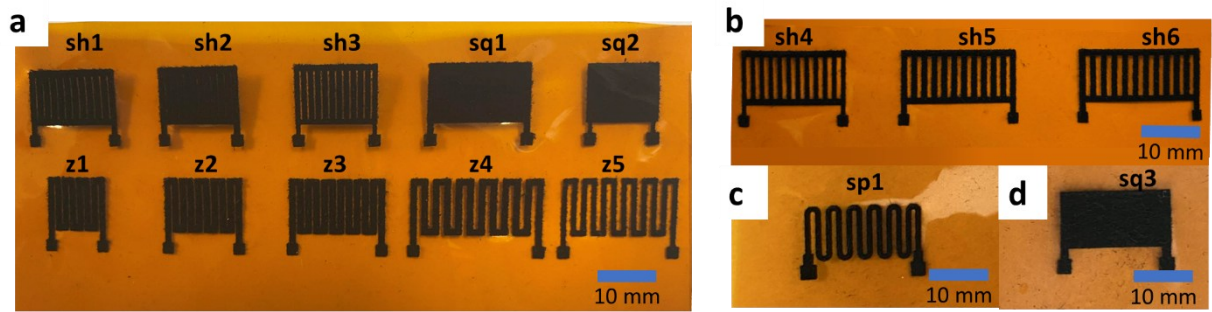
To mitigate the aforementioned transfer challenges, specific patterns demonstrating improved dimensional stability and reduced carbon expansion were selected for further analysis. The shutter patterns sh4, sh5, and sh6, along with the zigzag patterns z4 and z5, were chosen based on their ability to maintain well-defined features post-transfer. These patterns exhibited superior structural integrity and are therefore more suitable for continued evaluation.

Based on the sheet resistance data presented in Table 4-1, pattern sh6, which demonstrates the lowest sheet resistance among the shutter configurations, is selected as the representative shutter pattern. For the zigzag pattern category, z5 is chosen to ensure consistent width across the patterns. Additionally, the square pattern sq3 and the Serpentine pattern sp1 are designed to match the width and length dimensions of the other patterns, enabling a more rigorous comparative analysis.

Additional issues were identified during testing, specifically concerning the connection area between the graphene and the copper wire (highlighted in green in Figure 4-4f). The contact in this area was found to be inadequate, leading to increased electrical noise in the measurements. To address this issue, the connection section at the bottom of each pattern will be removed and repositioned on the left and right sides of the pattern. This adjustment is illustrated in Section 3, Figure 3-1, which depicts the revised configuration selected as the representative for each pattern.

*Table 4-1 Average and sheet resistance of various LIG sensor patterns.*

Pattern	Average Resistance ( $\Omega$ )	SD of Average Resistance	Sheet Resistance ( $\Omega \text{ sq}^{-1}$ )
<b>z1</b>	1.32E+04	17	158
<b>z2</b>	1.25E+04	173	120
<b>z3</b>	1.41E+04	84	112
<b>z4</b>	3.31E+04	104	253
<b>z5</b>	4.63E+04	108	471
<b>sh1</b>	3.61E+03	90	28
<b>sh2</b>	2.49E+03	166	20
<b>sh3</b>	3.83E+03	57	39
<b>sh4</b>	4.09E+03	95	24
<b>sh5</b>	3.95E+03	108	28
<b>sh6</b>	2.04E+03	17	19



	No. finger	a	b	w1	length	width	Sensing area	unit: mm	mm <sup>2</sup>
sh1	6	1.00	0.50		10.00	17.50	131.00		
sh2	6	1.00	0.25		10.00	14.75	125.50		
sh3	6	0.75	0.50		10.00	14.50	98.25		
sq1					10.00	17.50	175.00		
sq2					10.00	12.55	125.50		
z1	4	1.00	0.50	2.50	10.00	11.50	83.50		
z2	5	1.00	0.50	2.50	10.00	14.50	104.50		
z3	6	1.00	0.50	2.50	10.00	17.50	125.50		
z4	6	1.00	1.00	3.00	10.00	23.00	131.00		
z5	6	0.75	1.00	2.50	10.00	20.00	98.25		
sh4	6	1.20	1.00		10.00	25.40	170.40		
sh5	6	1.00	1.00		10.00	23.00	142.00		
sh6	6	0.75	1.00		10.00	20.00	106.50		
sp1	6	0.75	1.00	2.50	10.00	20.00	98.25		
sq3					10.00	20.00	200.00		

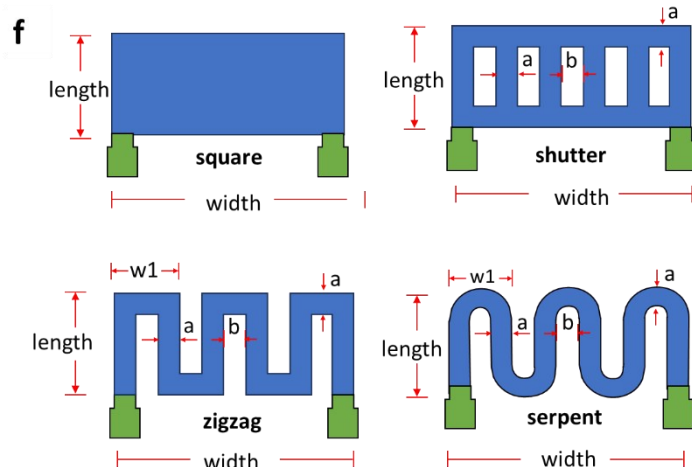


Figure 4-4 Photograph of LIG with different sensing patterns.

(a-d) Photographs of LIG with different patterns, and (e-f) Details of the designed patterns.

## **4.1. Performance of LIG-based Strain Sensors Fabricated on PI Substrates**

The performance of LIG-based strain sensors can be significantly influenced by the choice of fabrication parameters, and pattern designs. To thoroughly evaluate these factors, the study investigates the sensors' behaviour under various conditions, including different power levels, scanning speeds, and geometric patterns.

The study initially focused on LIG-based strain sensors fabricated directly on PI substrates without transferring to alternative materials. This approach enabled a controlled assessment of the intrinsic properties of LIG under different synthesis settings and pattern designs.

Four distinct LIG patterns — square, Serpentine, shutter, and zigzag — were synthesized using varied laser power and speed settings: 15% power at 200 mm/s, 20% power at 200 mm/s, 10% power at 100 mm/s, and 20% power at 400 mm/s. These configurations were chosen to evaluate the impact of laser power and speed on the electrical properties and mechanical durability of the LIG structures.

The evaluation was conducted under the constraints of available equipment, focusing on the measurement of electrical resistance of LIG patterns under different bending radii. This method provided insights into the material's strain-sensing capabilities under mechanical deformation.

Figure 4-5 presents the variation in electrical resistance behaviour of a LIG sensor fabricated at a speed of 200 mm/s and a laser power of 15%, employing a Serpentine pattern under various bending radii. The graph depicts the average change in resistance relative to the initial sensor resistance, along with the standard deviation of the percentage change. At the maximum bending deflection of 0.25 cm, the resistance increased by approximately 2.33% from its initial value. During the recovery phase, when the bending force was released, the resistance decreased to around 0.5% above the initial level, which is also lower than the resistance observed after bending to a radius of 1.25 cm. These observations highlight the sensor's ability to return close to its baseline resistance, demonstrating some degree of elasticity and resilience under mechanical stress.

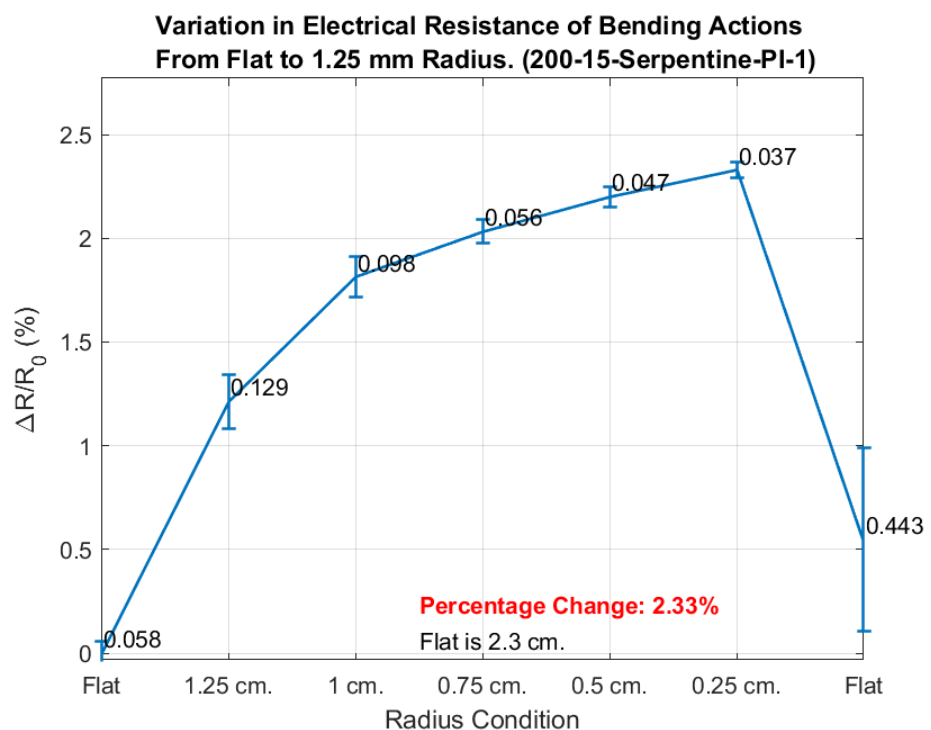


*Figure 4-5 Variation in electrical resistance of LIG serpentine during bending (Flat to 1.25 mm radius, synthesized at speed 200 mm/s, power 15%).*

Figure 4-6 displays the raw and filtered signals collected from the National Instruments system during the experiment. The data unit were change from voltage to resistance using Ohm's law. The bending radius of the sensor was systematically varied every 30 seconds, following a sequence from flat to 1.25 cm, 1 cm, 0.75 cm, 0.5 cm, 0.25 cm, and then back to flat. The top subplot shows the original signal, captured with 14-bit resolution, which includes the electrical resistance data along with noise sources such as human movement, wire interference, and AC electrical noise. To mitigate these noise effects, a notch filter was applied, resulting in the filtered signal presented in the bottom subplot. This process aims to isolate the true resistance changes due to bending from other external noise sources.

Even after applying the notch filter, some noise remained in the signal, making it unsuitable for precise analysis. Given that the resistance is expected to remain constant within each 30-second segment, a median filter was subsequently applied to further refine the signal, as depicted in the top subplot of Figure 4-7. To address the remaining noise, particularly spikes resulting from sudden movements or wire interference, an outlier removal technique was employed, producing the final cleaned signal shown in the bottom subplot. This multi-step filtering approach ensures that the analysed data accurately reflects the true changes in resistance due to bending, without being confounded by noise artifacts.

The cleaned signal reveals that the initial resistance of the sensor is 11.4 k $\Omega$ . Upon bending to a radius of 1.25 cm, the resistance increases to 11.55 k $\Omega$  and continues to incrementally rise as the bending radius is further reduced. At the smallest bending radius of 0.25 cm, the resistance reaches its peak value of over 11.65 k $\Omega$ , representing the highest reading recorded in this experiment. This change corresponds to a 2.35% increase from the initial resistance, consistent with the data presented in Figure 4-5. During the recovery phase, when the bending force is released, the resistance drops to below 11.5 k $\Omega$ , though it does not return entirely to its initial value. This incomplete recovery is likely due to residual noise from wire interference, human movement, and instability in the connection between the electrode and the LIG pattern. Despite these factors, the recovered resistance remains lower than the levels observed during bending, indicating the sensor's responsiveness to mechanical strain and partial elastic recovery.

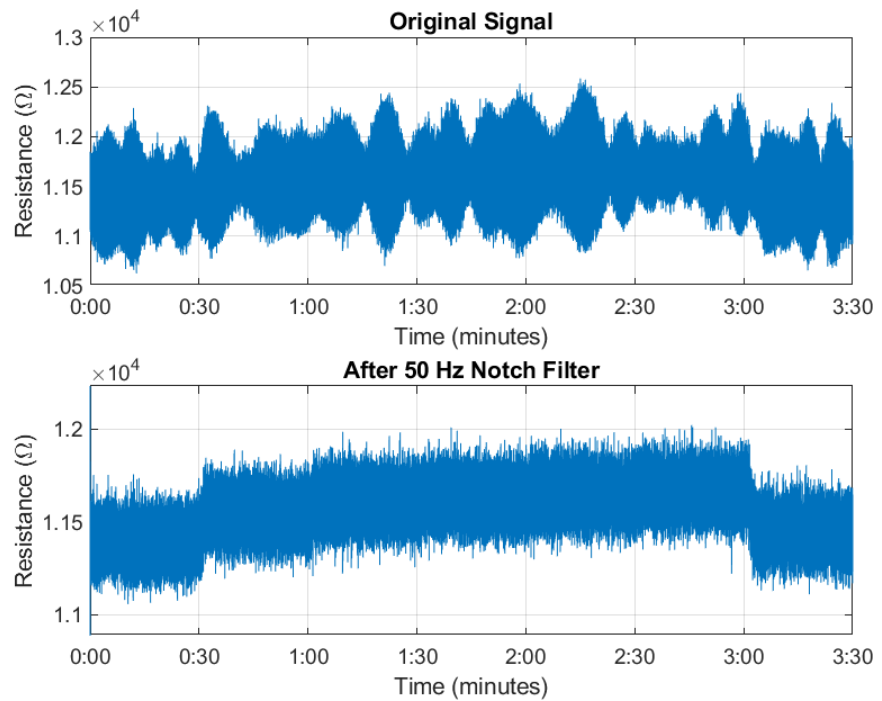


*Figure 4-6 Electrical resistance of LIG serpentine at different bending radii  
(Original signal vs. After notch filter, synthesized at speed 200 mm/s, power 15%)*

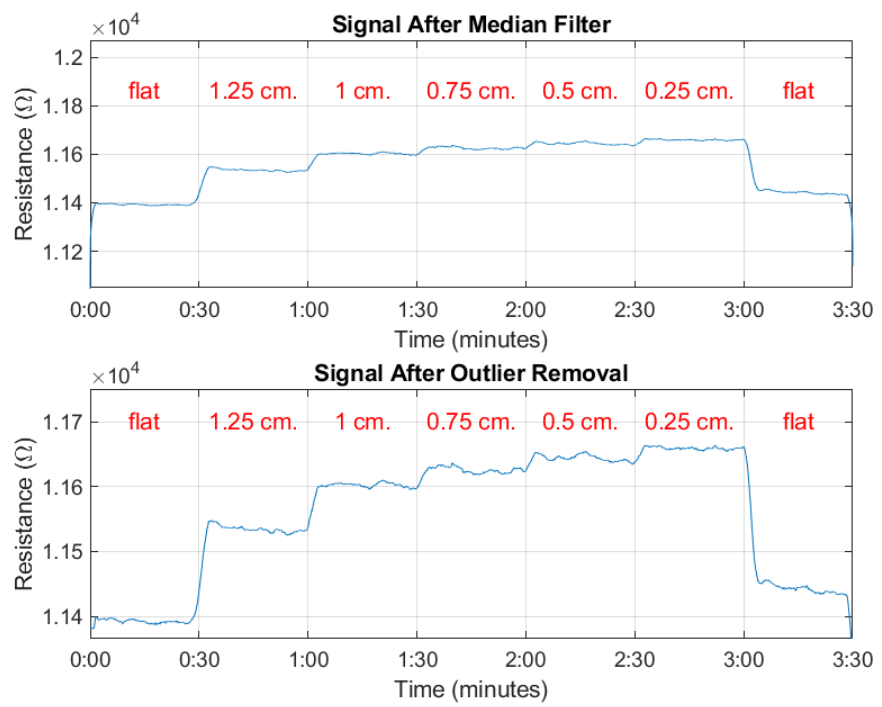


*Figure 4-7 Electrical resistance of LIG serpentine at different bending radii  
(Signal after median filter vs. After outlier removal, synthesized at speed 200 mm/s,  
power 15%)*

After the initial cycle measurement, nine additional measurements were conducted on the same sensor to evaluate its performance over multiple cycles. Figure 4-8 illustrates the variation in resistance compared to the initial resistance across these cycles. It was observed that in some cycles, the change in resistance at a bending radius of 0.25 cm was lower than in others. For instance, during the fifth cycle, the maximum change was only 2%, indicating less sensitivity compared to other cycles.

Moreover, the recovery behaviour varied significantly between cycles. For example, in the third and seventh cycles, the recovery points were higher by more than 0.5% compared to other cycles, suggesting variability in the sensor's ability to return to its baseline resistance. In contrast, the tenth cycle exhibited a recovery segment with a minimal change of 0.05%, nearly matching the initial resistance value. These observations highlight the sensor's inconsistent response and recovery behaviour over multiple cycles, likely due to factors such as material fatigue, sensor instability, or variations in environmental conditions.

**Variation in Electrical Resistance of Bending Actions over Multiple Cycles**  
200-15-Serpentine-PI

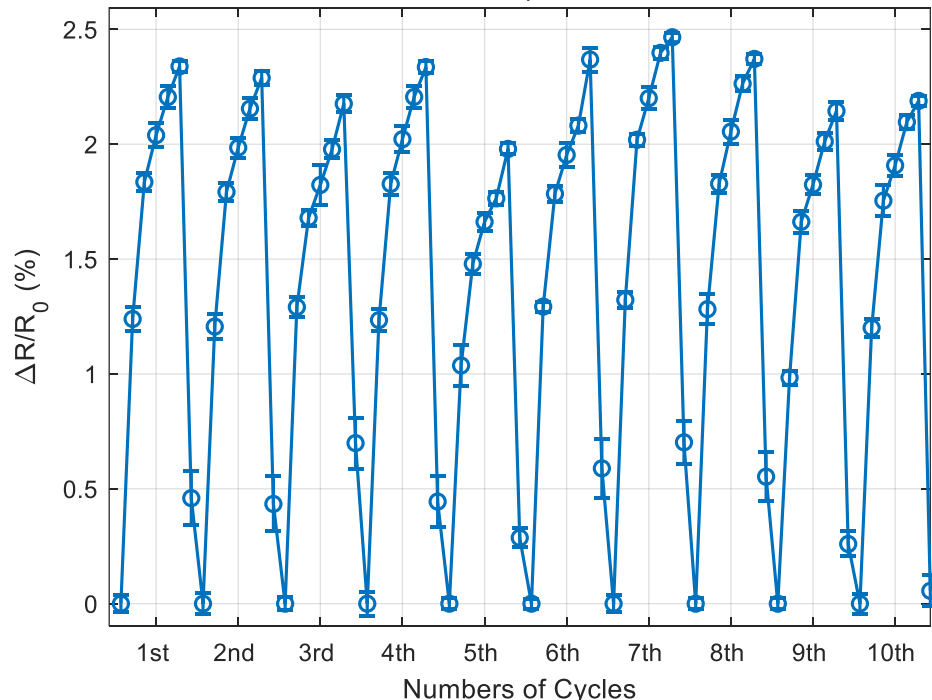


*Figure 4-8 Variation in electrical resistance of LIG serpentine at different bending radii over multiple cycles (Synthesized at speed 200 mm/s, power 15%)*

Figure 4-9 shows the percentage change in electrical resistance of an LIG sensor with a square pattern, fabricated at a speed of 200 mm/s and a laser power of 15%. The graph illustrates the average change in resistance relative to the initial value across various bending radii, including the standard deviation of the percentage changes. Specifically, at a bending radius of 1.25 cm, the resistance increased by 2.17%, while at a radius of 0.25 cm, it rose by approximately 6.80%. During the recovery phase, after the bending force was released, the resistance returned to about 0.003% above the initial value. These results highlight the sensor's sensitivity to mechanical strain and its capability to nearly return to baseline resistance, demonstrating its effectiveness and resilience under mechanical stress. Details on signal processing, including raw and filtered signals as well as cycle data, are provided in the appendix.

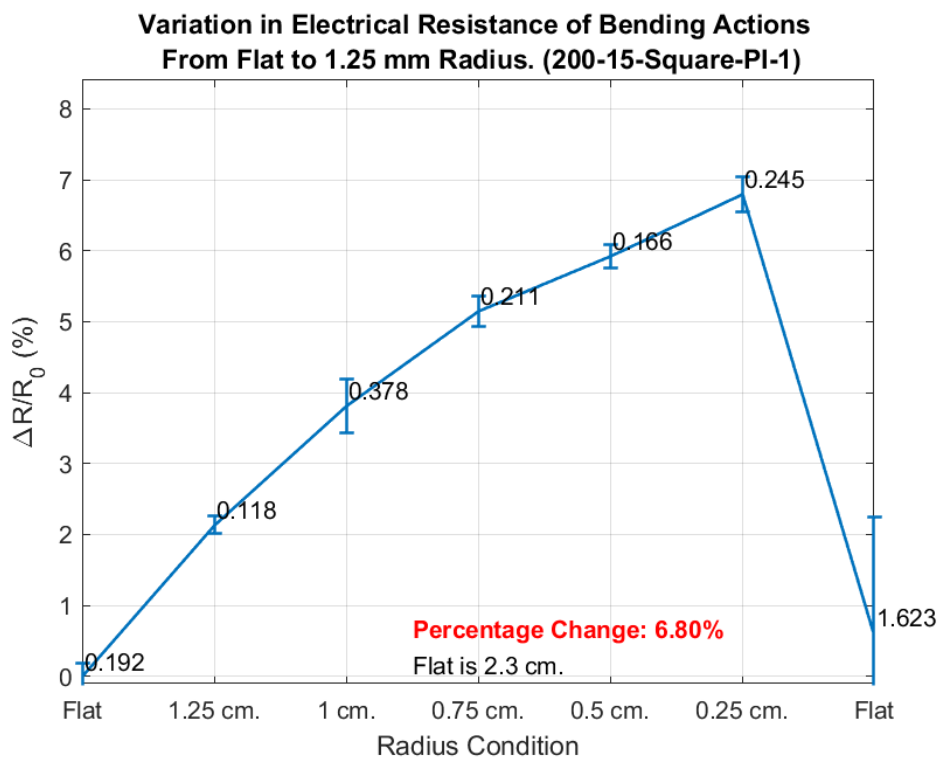


Figure 4-9 Variation in electrical resistance of LIG square during bending (Flat to 1.25 mm radius, synthesized at speed 200 mm/s, power 15%).

Figure 4-10 shows the variation in electrical resistance of an LIG sensor with a shutter pattern, fabricated at a speed of 200 mm/s and a laser power of 15%. The graph depicts the average change in resistance relative to the initial value across various bending radii, including the standard deviation of these changes. At a bending radius of 0.25 cm, the resistance increased by approximately 3.82%. During the recovery phase, after the bending force was released, the resistance returned to about 0.88% above the initial value. This post-bending resistance is higher than the resistance observed at a bending radius of 1.25 cm, which was 0.73%. This indicates that the sensor's recovery is not as effective as its response to bending, suggesting room for improvement in its recovery behaviour.

Figure 4-11 illustrates the percentage change in electrical resistance of the same LIG sensor with a shutter pattern, specifically during the fourth cycle of testing. At a bending radius of 0.25 cm, the resistance increased by 3.13%, which is lower than the increase observed in the first cycle. During the recovery phase, after the bending force was released, the resistance returned to approximately 0.43% above the initial value. Although this cycle demonstrates better recovery ability compared to previous cycles, it exhibits reduced sensitivity to mechanical strain. These results emphasize the sensor's capacity for near-baseline recovery but highlight a decrease in sensitivity in the later cycles.

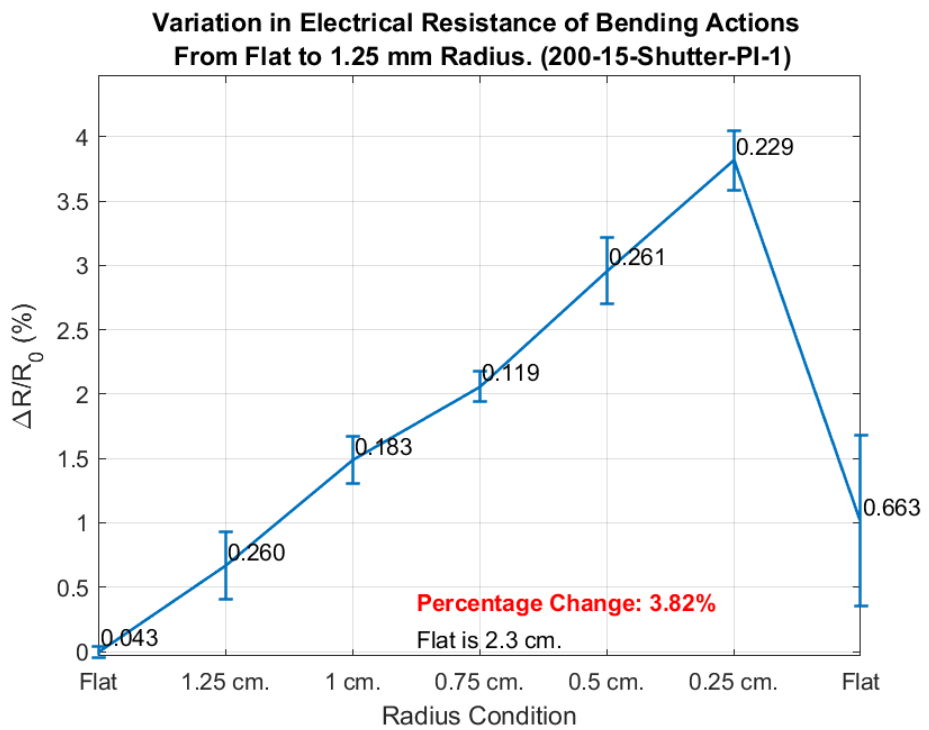


Figure 4-10 Variation in electrical resistance of LIG shutter during bending (Flat to 1.25 mm radius, synthesized at speed 200 mm/s, power 15%, 1<sup>st</sup> cycle).

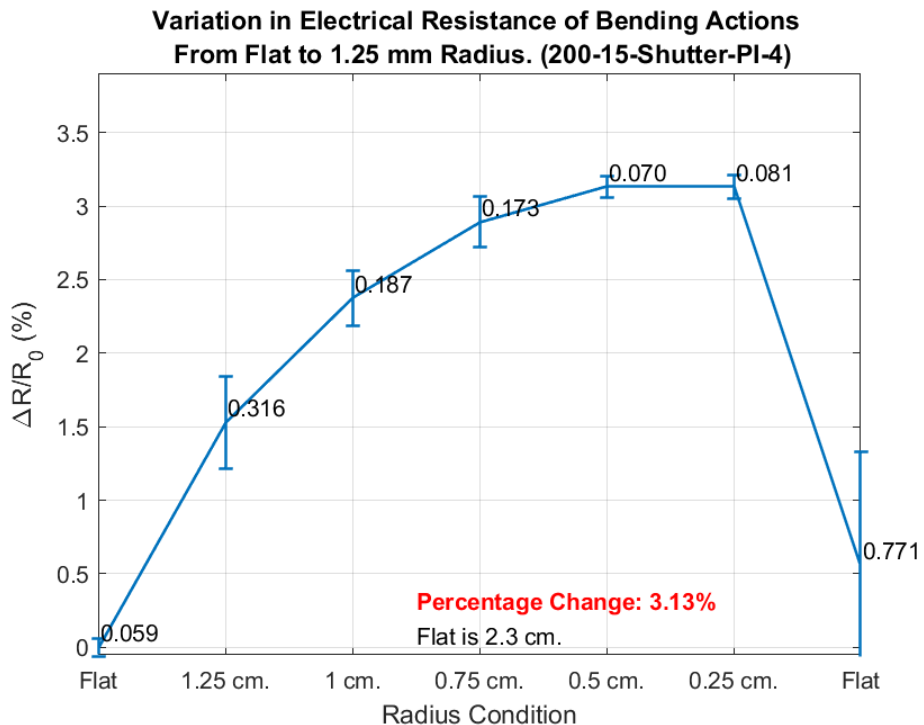
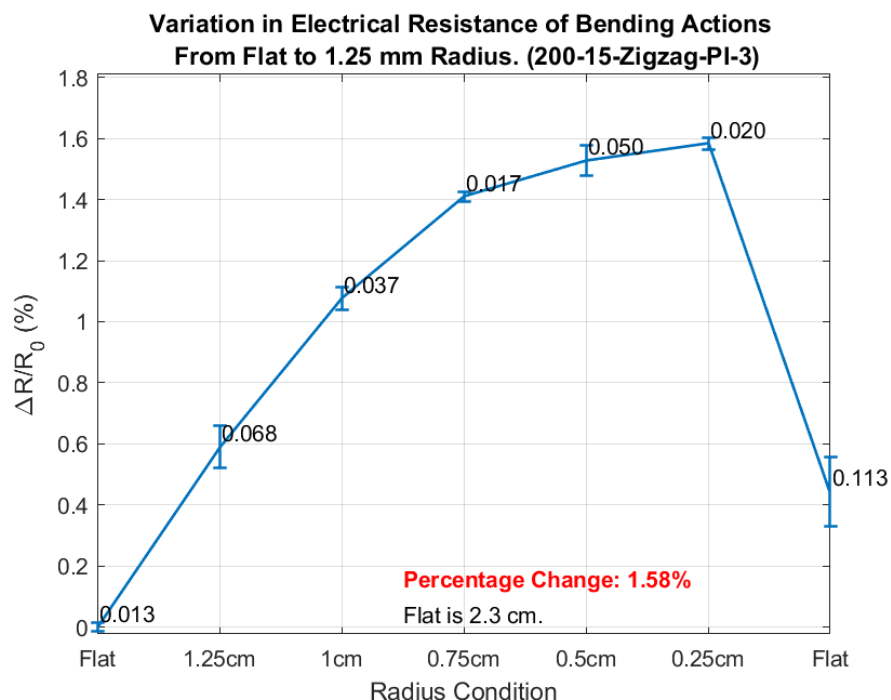


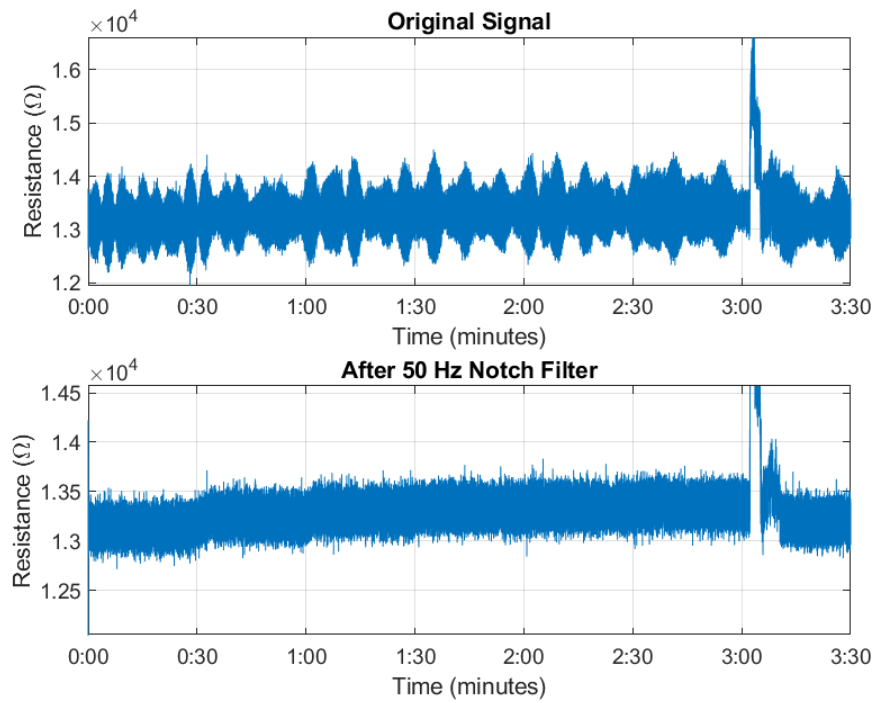
Figure 4-11 Variation in electrical resistance of LIG shutter during bending (Flat to 1.25 mm radius, synthesized at speed 200 mm/s, power 15%, 4<sup>th</sup> cycle).

Figure 4-12 shows the variation in electrical resistance of an LIG sensor with a zigzag pattern, assessed during the fourth test cycle. At a bending radius of 0.25 cm, the resistance increased by 1.58%, which is lower compared to other patterns fabricated with the same parameters. Remarkably, during the recovery phase, the resistance returned to only 0.41% above the initial value after the bending force was released, achieving the best recovery performance among all tested cycles.

Figure 4-13 shows the raw and filtered signals during the experiment where the sensor's bending radius was varied every 30 seconds. The data unit were change from voltage to resistance using Ohm's law. The top subplot displays the original signal with noise spikes from human movement. After applying a notch filter, the bottom subplot reveals some residual high spikes. Figure 4-14 illustrates the signal further processed with a median filter, which effectively reduces noise and residual spikes. The cleaned signal, shown in the bottom subplot, is achieved through outlier removal, ensuring that the data accurately reflects resistance changes due to bending and minimizing noise artifacts.



*Figure 4-12 Variation in electrical resistance of LIG shutter during bending (Flat to 1.25 mm radius, synthesized at speed 200 mm/s, power 15%, 3<sup>rd</sup> cycle).*



*Figure 4-13 Electrical resistance of LIG zigzag at different bending radii  
(Original signal vs. After notch filter, synthesized at speed 200 mm/s, power 15%)*

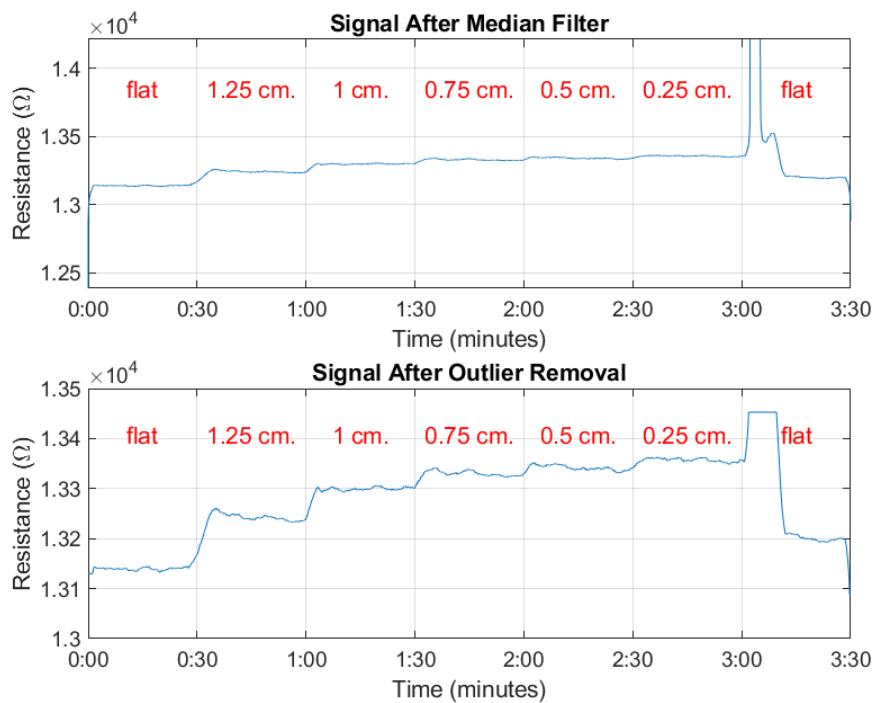


*Figure 4-14 Electrical resistance of LIG zigzag at different bending radii  
(Signal after median filter vs. After outlier removal, synthesized at speed 200 mm/s,  
power 15%)*

Figure 4-15 illustrates the percentage change in electrical resistance characteristics of an LIG sensor with a Serpentine pattern, fabricated at 20% laser power and a speed of 200 mm/s. The graph shows the average resistance change relative to the initial value across different bending radii, along with the standard deviation of these changes.

At a bending radius of 1.25 cm, the resistance increased by 4.19%, which is higher than the maximum increase seen with lower power fabrications. At a smaller bending radius of 0.25 cm, the resistance rose by approximately 6.77%. After the bending force was released, the sensor's resistance returned to about 0.71% above the initial value. This resistance after deformation is notably different from the values observed during bending, highlighting a distinct difference between the resistance levels at 1.25 cm and 0.25 cm radii and the post-deformation readings.

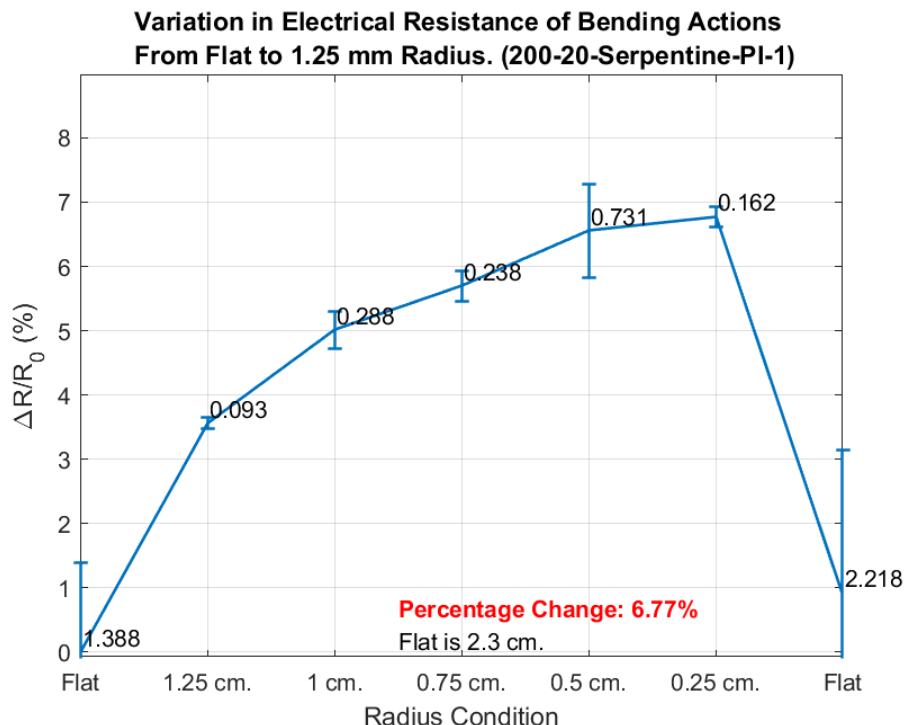


*Figure 4-15 Variation in electrical resistance of LIG serpentine during bending (Flat to 1.25 mm radius, synthesized at speed 200 mm/s, power 20%).*

Figure 4-16 presents the relative change in electrical resistance characteristics of an LIG sensor with a square pattern, produced at a laser power of 20% and a speed of 200 mm/s. The graph depicts the average change in resistance relative to the initial value across a range of bending radii, including the standard deviation for each measurement.

When bent to a radius of 1.25 cm, the resistance showed an increase of 1.56%. At a tighter radius of 0.25 cm, the resistance rose more sharply, by approximately 4.41%. Following the release of the bending force, the sensor's resistance nearly returned to its original level, settling at just 0.19% above the initial value. This minimal deviation indicates that the sensor effectively regains its original resistance after being deformed.

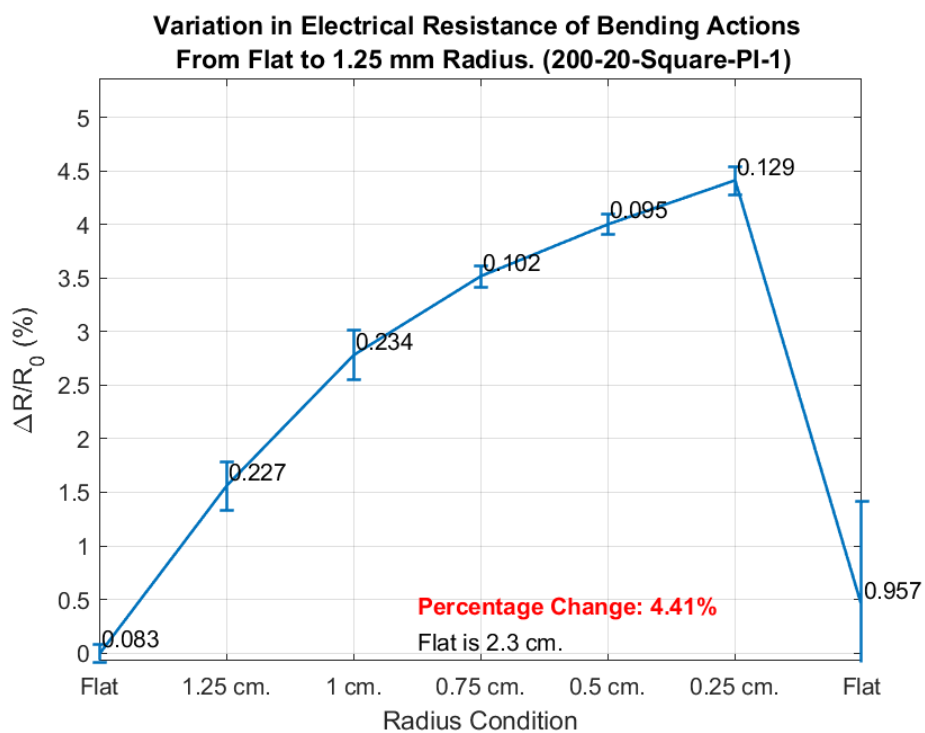


Figure 4-16 Variation in electrical resistance of LIG square during bending (Flat to 1.25 mm radius, synthesized at speed 200 mm/s, power 20%).

Figure 4-17 showcases how an LIG sensor with a shutter pattern responds to mechanical strain, created using a laser power of 20% and a speed of 200 mm/s. As the graph reveals, resistance changes depend on the bending radius, with the data including both average shifts from the initial resistance and the corresponding standard deviations.

At a bending radius of 1.25 cm, the sensor's resistance increased by 3.39%. When the radius tightened to 0.25 cm, resistance climbed more steeply to 6.86%, exceeding the rise observed for the same pattern produced at a lower power setting. Interestingly, once the bending force was removed, the resistance nearly returned to its baseline, settling at only 0.52% above the starting value. This small difference suggests that the sensor can reliably recover its original resistance even after significant deformation.

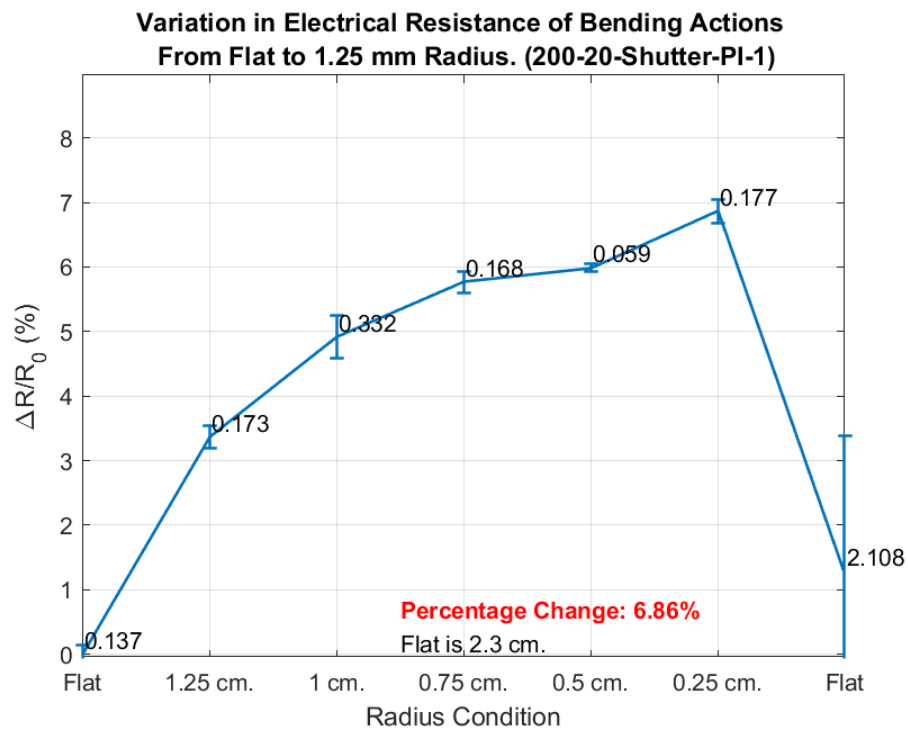


Figure 4-17 Variation in electrical resistance of LIG shutter during bending (Flat to 1.25 mm radius, synthesized at speed 200 mm/s, power 20%).

A LIG sensor with a zigzag pattern's dynamic response to mechanical deformation is depicted in Figure 4-18. Built with 20% laser power and 200 mm/s speed, the resistance response of this sensor changes dramatically with the bending radius. Various bending circumstances are shown on the graph, together with the average change from the initial resistance and the standard deviations.

A more moderate 1.25 cm bend results in a 3.59% increase in resistance. However, when the bend is only 0.25 cm tight, the resistance increases sharply to 2.69%, which is more than what is observed at lower power levels for the same pattern. Upon releasing the bending force, the sensor nearly returns to its initial state, with resistance ending up just 0.14% higher than where it started. This slight shift shows that the sensor keeps its shape and consistently rebounds to its initial resistance, even when subjected to high stress.

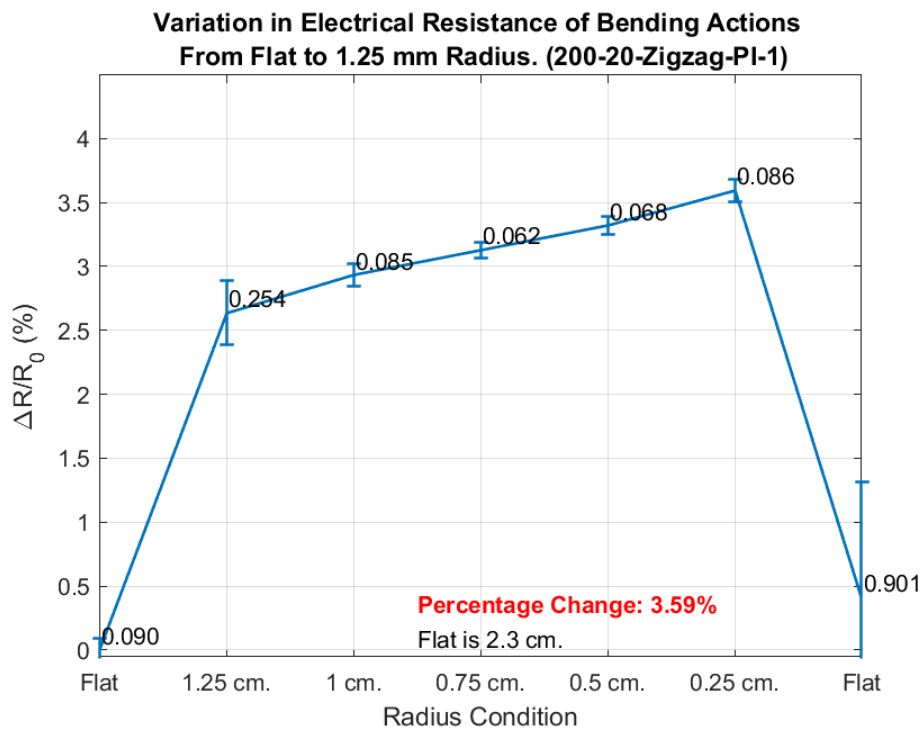


Figure 4-18 Variation in electrical resistance of LIG zigzag during bending (Flat to 1.25 mm radius, synthesized at speed 200 mm/s, power 20%).

Table 4-2 summarises a detailed analysis of the electrical resistance response of LIG sensors with various patterns—square, shutter, Serpentine, and zigzag—fabricated under different laser powers (10%, 15%, and 20%) and speeds (100, 200, and 400 mm/s). The data captures the percentage change in resistance relative to the initial value across different bending radii, with the maximum change consistently observed at the smallest bending radius of 0.25 cm. This observation highlights that smaller bending radii exert higher mechanical stress on the sensors, leading to more significant changes in resistance.

### Sensitivity Analysis

The percentage change in resistance is a critical metric for evaluating the sensitivity of LIG-based strain sensors. Across all sensor patterns, the most remarkable shift in resistance occurred at a bending radius of 0.25 cm. At a laser power of 10% and a speed of 100 mm/s, the square pattern exhibited the highest resistance change of 28.97%, followed by the shutter (21.27%), Serpentine (13.62%), and zigzag (9.68%) patterns. These results suggest that the square pattern demonstrates the highest responsiveness to mechanical strain, indicating its potential suitability for applications requiring the detection of small deformations.

### Baseline Resistance and Recovery Capacity

A strain sensor's practical efficacy is contingent upon its baseline resistance and recovery capacity; despite showing lower percentage changes in resistance, patterns such as the Serpentine and zigzag exhibit substantially higher baseline resistances (15,925.50  $\Omega$  and 19,135.50  $\Omega$ , respectively, at 10% power and 100 mm/s). High baseline resistance can diminish a sensor's sensitivity to small changes and increase power consumption, which is typically undesirable for applications requiring precise strain measurement. However, these patterns may offer advantages in terms of durability and resistance to mechanical fatigue, rendering them suitable for scenarios where long-term stability is prioritized over sensitivity.

## **LIG-Pi: Patterns and Fabrication Factors Comparison**

As the laser power decreases, the sensors' resistance generally increases. At a laser power of 15% and a speed of 200 mm/s, there is a notable decrease in the percentage change in resistance across all sensor patterns. For example, the square pattern's resistance change falls from 28.97% at 10% power to 6.98% at 15% power, while the Serpentine pattern's change drops from 13.62% to 2.27%. This reduction indicates that lower laser power and faster fabrication speeds decrease sensitivity to mechanical deformation, as the increased speed shortens fabrication time but impacts strain responsiveness.

Moreover, recovery rates at 10% laser power are lower than other factors but still high at more than 95%. At 15% power, the square pattern shows good recovery, and the Serpentine pattern recovers 99.6% of its baseline resistance. Higher recovery rates suggest that these sensors better return to their original resistance post-deformation, which is advantageous for applications needing precise and frequent strain recovery. However, the response time of these LIG sensors, approximately 2 seconds, is slower than expected compared to theoretical predictions and existing literature. This discrepancy requires further investigation.

At the highest laser power of 20%, fabrication speed reveals an influence on sensor performance. At 200 mm/s, the serpentine pattern exhibits a resistance change of 7.52%, whereas the zigzag pattern shows a lower change of 3.68%. Increasing the speed to 400 mm/s results in even more minor resistance changes, with the square pattern showing just 0.56%. This trend demonstrates that higher laser power and slower speeds produce sensors with more significant resistance changes. Slower speeds facilitate a more controlled graphene deposition, enhancing sensitivity, whereas faster speeds may result in less uniform deposition and reduced sensitivity.

The data highlight the complex interactions between laser power, fabrication speed, and sensor pattern on performance. For applications requiring high sensitivity to minor deformations, patterns with lower baseline resistances and higher percentage changes—such as the square pattern at lower laser powers—are ideal. Conversely, patterns with higher resistances and lower percentage changes, like the Serpentine and zigzag, are more suitable for applications demanding durability and consistent performance.

*Table 4-2 LIG-PI strain sensors evaluation with different patterns under various fabrication conditions.*

Power (%)	Speed (mm/s)	Pattern	Percentage Change (%) (SD)	Average Resistance ( $\Omega$ ) (SD)	Recovery (%)	Average Response Time (s) (SD)
10	100	Square	28.97 (0.67)	319.4 (23.1)	98.4	3.12 (1.96)
10	100	Shutter	21.27 (1.03)	1217.6 (52.3)	95.8	1.61 (1.12)
10	100	Serpentine	13.62 (0.90)	15925.5 (650.6)	94.2	1.78 (1.32)
10	100	Zigzag	9.68 (0.70)	19135.5 (803.1)	98.9	3.12 (3.53)
15	200	Square	6.98 (0.11)	188.3 (15.4)	100.0	4.12 (5.00)
15	200	Shutter	3.54 (0.17)	811.7 (34.8)	99.1	2.12 (1.12)
15	200	Serpentine	2.27 (0.15)	10617.0 (433.8)	99.6	2.49 (1.59)
15	200	Zigzag	1.61 (0.12)	12757.0 (535.4)	99.4	4.12 (3.45)
20	200	Square	4.47 (0.07)	214.6 (16.6)	99.8	2.49 (1.30)
20	200	Shutter	7.06 (0.08)	700.6 (17.5)	99.5	1.61 (0.87)
20	200	Serpentine	7.52 (0.03)	17726.0 (297.4)	99.3	1.46 (0.83)
20	200	Zigzag	3.68 (0.06)	13994.0 (1121.6)	99.9	2.25 (1.18)
20	400	Square	0.56 (0.06)	1792.0 (289.9)	99.2	3.43 (2.30)
20	400	Shutter	2.35 (0.08)	2152.5 (212.8)	97.9	2.62 (1.15)
20	400	Serpentine	2.51 (0.03)	24356.5 (3601.3)	97.1	2.50 (1.20)
20	400	Zigzag	1.23 (0.06)	22334.5 (664.0)	99.4	3.65 (3.20)

## 4.2.Performance of LIG-based Strain Sensors on PU Substrates

The choice of sensor patterns and materials can significantly influence the performance of LIG-based strain sensors on PU substrates. Transferring patterns from PI to a more flexible material, such as PU, is commonly used to enhance the strength and sensitivity of strain sensors. This study examines the transfer of LIG patterns initially created on PI substrates to PU. Specifically, patterns produced on PI at a laser speed of 100 mm/s and power of 10% will be transferred to PU. Additionally, patterns made on PI with a higher speed of 200 mm/s and power of 20% will be transferred to PU. This approach aims to leverage PU's enhanced stability to improve the performance and durability of the strain sensors.

Figure 4-19a illustrates the transfer of various patterns from PI to PU substrates. All carbon areas were observed to maintain good shape, with fingers, gaps, and lines visible and well-defined. In contrast, Figure 4-19b demonstrates the application of a PU top layer over the sensor shown in Figure 4-19a. This PU layer is a protective tape, preventing the carbon from vanishing and enhancing the sensor's stability and durability, especially for cyclic applications.

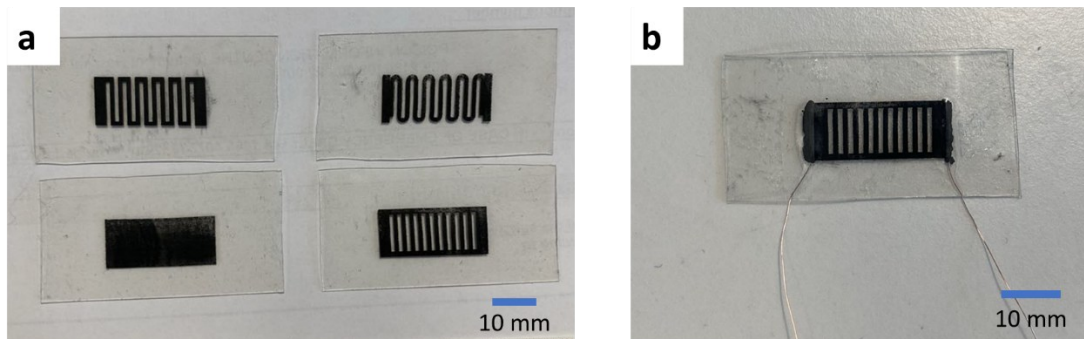


Figure 4-19 LIG-PU strain sensor with various sensing patterns.

(a) LIG-PU sensor showcasing different sensing patterns., and(b) LIG-PU sandwich sensor with PU top layer, enhancing stability and durability for cyclic applications.

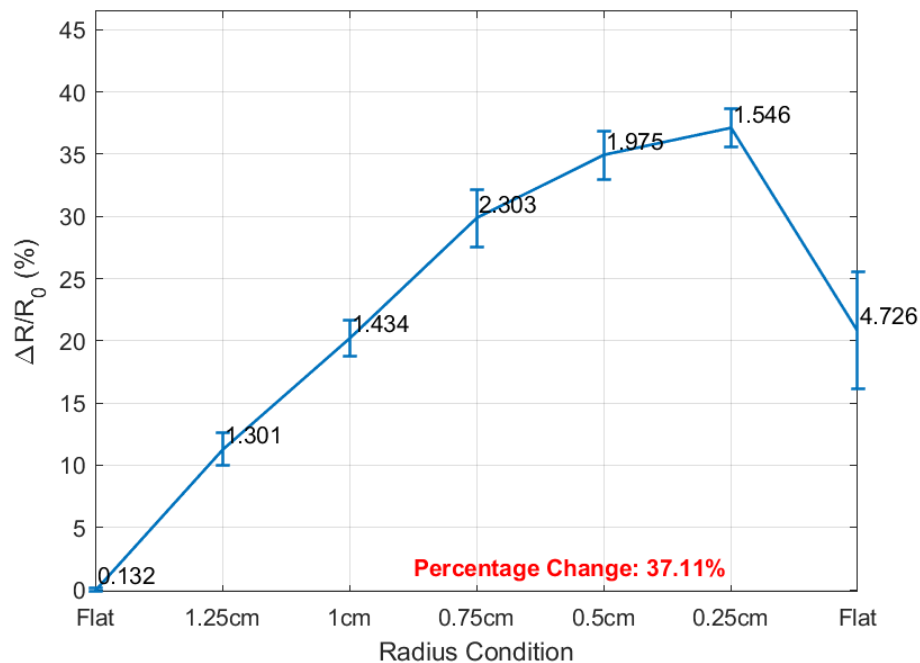
Figure 4-20 illustrates the proportional change in electrical resistance behaviour of a Serpentine-patterned LIG sensor fabricated at a scan speed of 200 mm/s and a laser power of 20%, then transferred to a PU substrate. The graph shows the percentage change in resistance relative to the initial value across various bending radii, including standard deviations. At a bending radius of 1.25 cm, the sensor exhibited an 11.29% increase in resistance, while a more acute radius of 0.25 cm led to a 37.11% increase. Following removing the bending force, the resistance did not return to its original level but stabilized at approximately 20.85% above the initial value.

Figure 4-21 depicts the resistance response of a square-patterned LIG sensor fabricated under the same conditions and transferred to a PU substrate. The resistance increased by 17.86% at a bending radius of 1.25 cm and by about 22.77% at a radius of 0.25 cm. After removing the bending force, the resistance increased to approximately 25.37% above the initial value. These observations suggest that the sensor does not fully revert to its original resistance after deformation, potentially due to residual stress or static forces affecting the sensor structure or wire connections.

Figure 4-22 illustrates the percentage difference in resistance of a shutter-patterned LIG sensor fabricated at a scan speed of 200 mm/s with a laser power of 20% and transferred to a PU substrate. The sensor shows a resistance increase of 17.43% at a bending radius of 1.25 cm, which intensifies to 57.58% at a 0.25 cm radius. Remarkably, after bending, the resistance stabilizes around 36.36% above the initial value, indicating a significant residual effect and suggesting that full recovery is not achieved.

Figure 4-23 presents the performance of a zigzag-patterned LIG sensor manufactured under the same conditions and transferred to a PU substrate. Resistance increases by 18.46% at a 1.25 cm bending radius and 25.95% at 0.25 cm. Following deformation, the resistance settles at 22.38% above the initial value but does not return to the baseline. This pattern of behavior, observed in both shutter and zigzag designs, points to difficulties in achieving complete resistance recovery post-deformation.

**Variation in Electrical Resistance of Bending Actions From Flat to 1.25 mm Radius.  
(200-20-Serpentine-PU)**



*Figure 4-20 Variation in electrical resistance of LIG-PU Serpentine during bending  
(Flat to 1.25 mm radius, synthesized at speed 200 mm/s, power 20%).*

**Variation in Electrical Resistance of Bending Actions From Flat to 1.25 mm Radius.  
(200-20-Square-PU)**

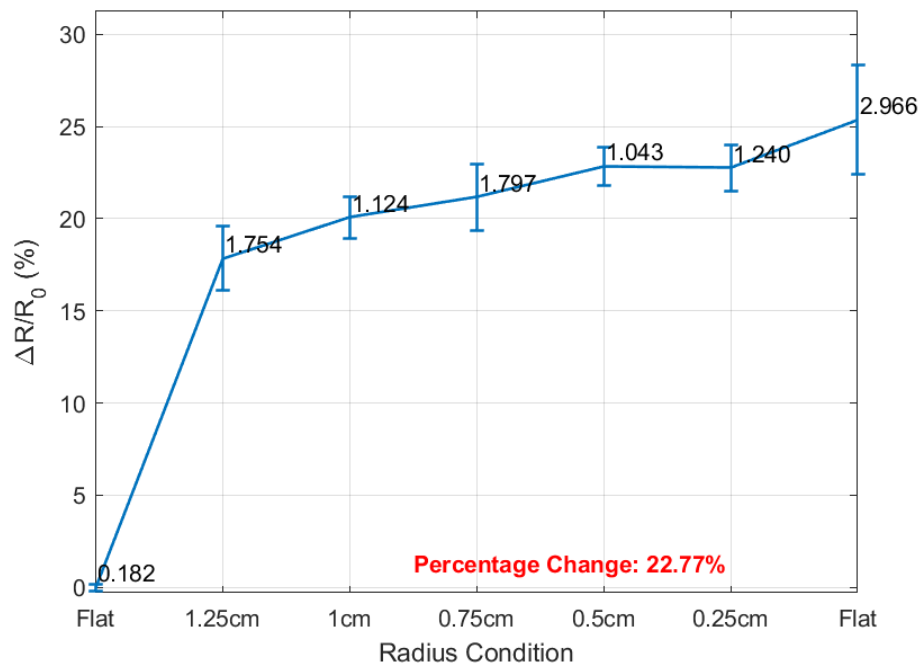


*Figure 4-21 Variation in electrical resistance of LIG-PU square during bending  
(Flat to 1.25 mm radius, synthesized at speed 200 mm/s, power 20%).*

**Variation in Electrical Resistance of Bending Actions From Flat to 1.25 mm Radius.  
(200-20-Shutter-PU)**

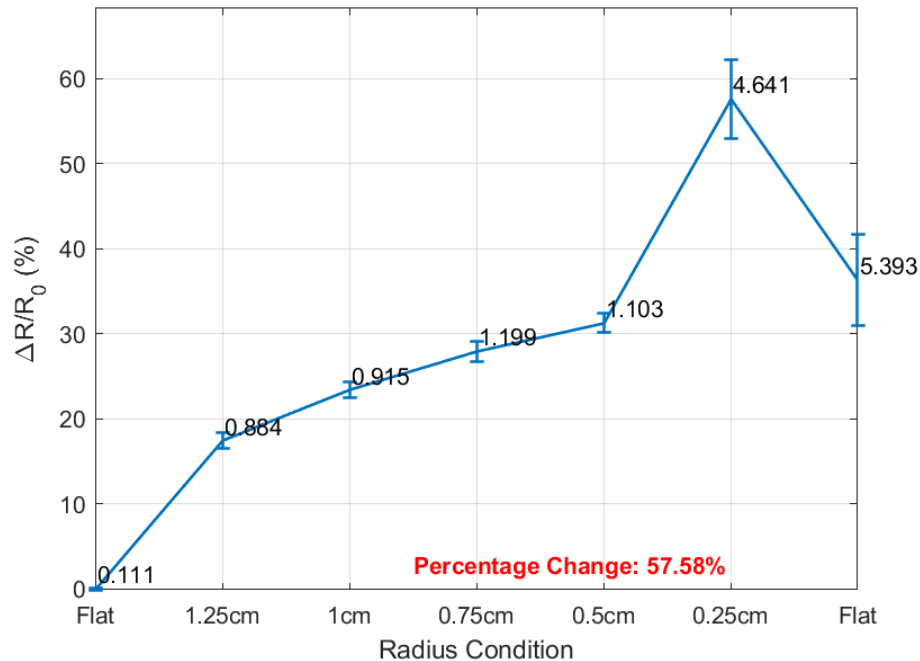


*Figure 4-22 Variation in electrical resistance of LIG-PU shutter during bending (Flat to 1.25 mm radius, synthesized at speed 200 mm/s, power 20%).*

**Variation in Electrical Resistance of Bending Actions From Flat to 1.25 mm Radius.  
(200-20-Zigzag-PU)**

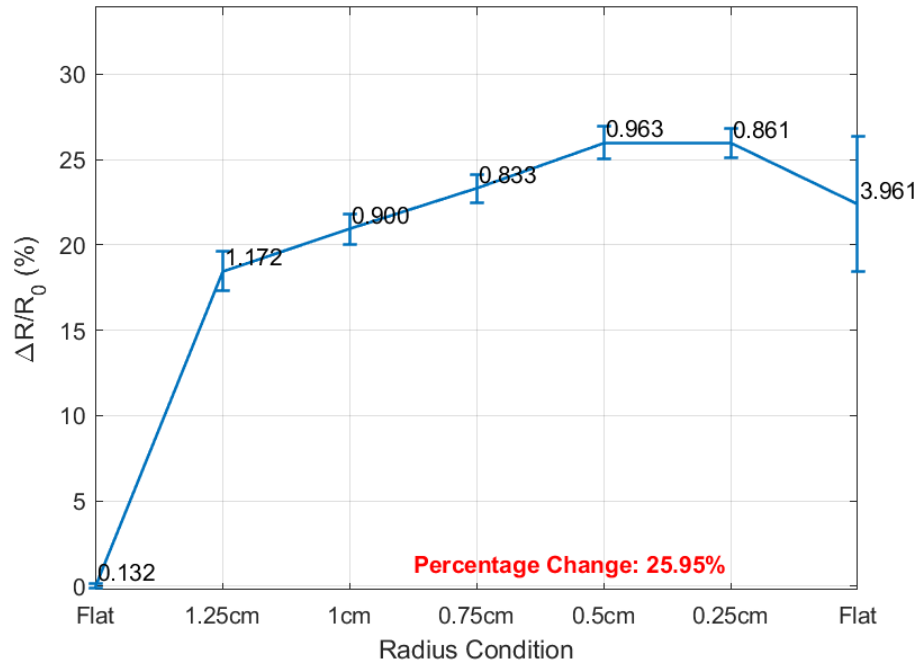


*Figure 4-23 Variation in electrical resistance of LIG-PU zigzag during bending (Flat to 1.25 mm radius, synthesized at speed 200 mm/s, power 20%).*

Figure 4-24 depicts the variation in resistance of a serpentine-patterned LIG sensor fabricated at a scan speed of 100 mm/s with a laser power of 10% and transferred to a PU substrate. The data reveal a dramatic increase in resistance: 132% at a bending radius of 1.25 cm, escalating to an astonishing 722% at a radius of 0.25 cm. After bending, the resistance stabilizes approximately 99% above the initial value. This substantial residual resistance indicates a significant impact of deformation on the sensor's performance, suggesting that the serpentine-patterned design may suffer from limited recovery capabilities and prolonged residual effects.

Figure 4-25 presents the resistance characteristics of a square-patterned LIG sensor manufactured under identical conditions and transferred to a PU substrate. The resistance shows a notable increase of 169% at a bending radius of 1.25 cm and an extreme 4091% at 0.25 cm. After deformation, the resistance stabilizes at 43% higher than its initial value. The high resistance change, particularly at smaller bending radii, and the incomplete recovery suggest that the square-patterned sensor exhibits even greater sensitivity to deformation and residual effects than the serpentine-patterned sensor. This behaviour underscores the difficulty in achieving full resistance recovery, potentially due to the complex stress distribution and structural deformation specific to the square pattern.

Figure 4-26 illustrates the filtered signal at different bending radii, revealing a minimal difference in voltage change between 0.5 cm and 0.25 cm bending radii. After releasing the bending force, the voltage decreases but does not revert to its initial value. The sensor's high sensitivity makes it easier to detect variations in bending and recovery. This voltage after bending, which fails to return to the baseline, is consistent with the observations in Figures 4-24 and 4-25. Similarly, Figure 4-27 shows the performance of a square-patterned sensor, where voltage changes with different bending radii are distinct due to the sensor's high sensitivity. After deformation, the voltage decreases but remains above the initial value, reflecting the sensor's inability to recover fully. The consistent pattern across different designs indicates that high sensitivity contributes to noticeable voltage changes during and after bending, but all sensors face challenges in achieving complete recovery.

**Variation in Electrical Resistance of Bending Actions From Flat to 1.25 mm Radius.  
(100-10-Serpentine-PU)**

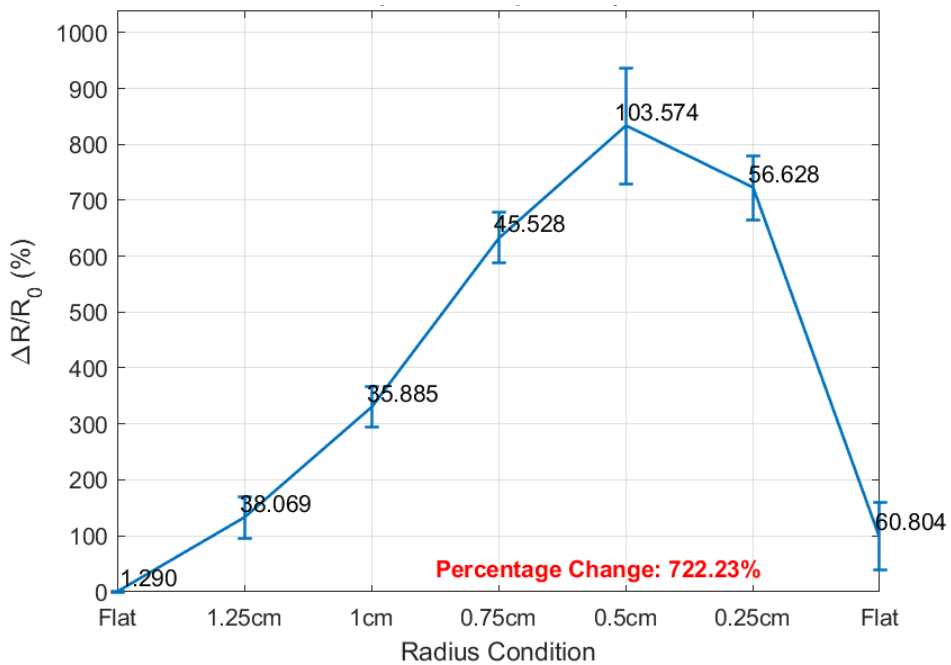


Figure 4-24 Variation in electrical resistance of LIG-PU Serpentine during bending (Flat to 1.25 mm radius, synthesized at speed 100 mm/s, power 10%).

**Variation in Electrical Resistance of Bending Actions From Flat to 1.25 mm Radius.  
(100-10-Square-PU)**

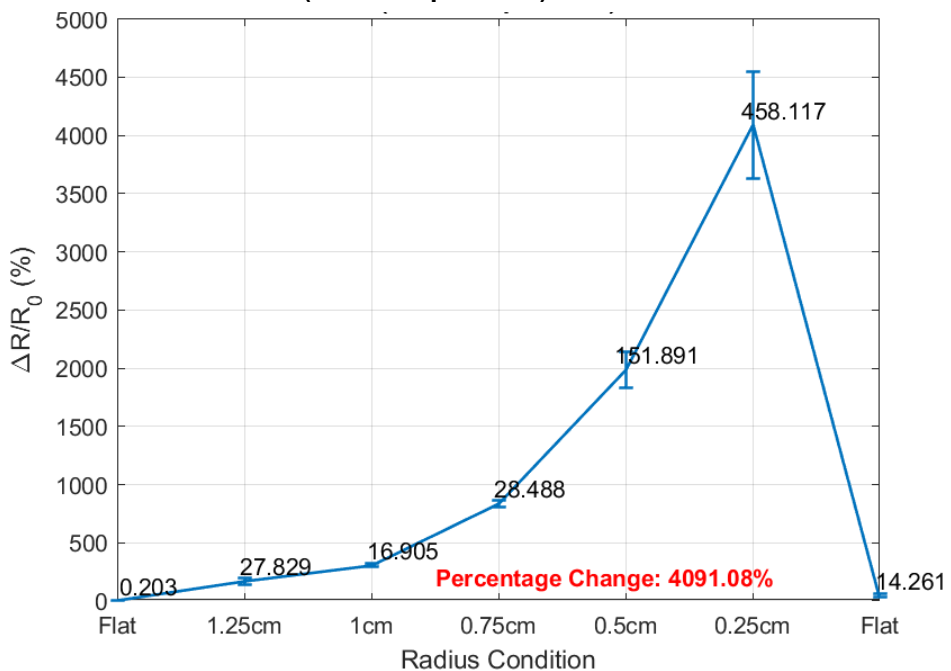
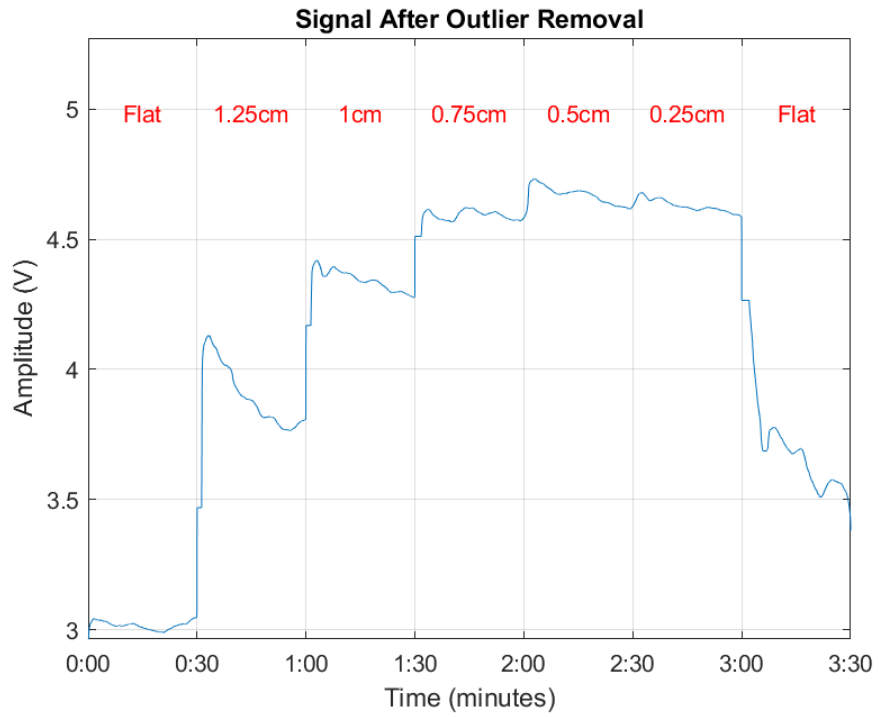
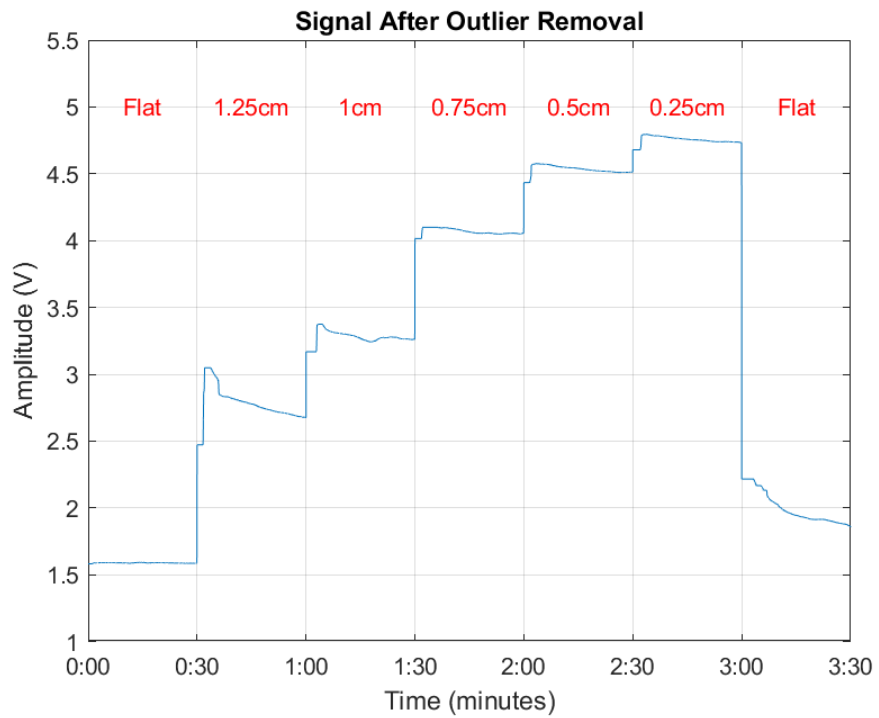


Figure 4-25 Variation in electrical resistance of LIG-PU square during bending (Flat to 1.25 mm radius, synthesized at speed 100 mm/s, power 10%).



*Figure 4-26 Voltage of LIG-PU Serpentine at different bending radii  
(Signal after outlier removal, synthesized at speed 100 mm/s, power 10%).*



*Figure 4-27 Voltage of LIG-PU square at different bending radii  
(Signal after outlier removal, synthesized at speed 100 mm/s, power 10%).*

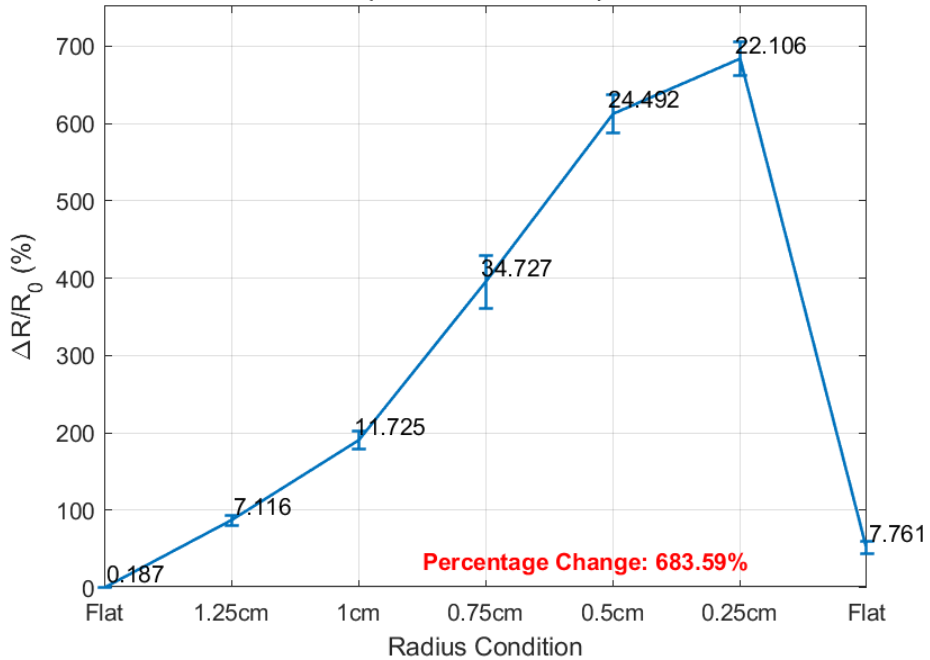
Figure 4-28 captures the resistance dynamics of a shutter-patterned LIG sensor, manufactured at a scan speed of 100 mm/s with a laser power of 10% and transferred to a PU substrate. The sensor demonstrates a marked resistance increase of 87% at a bending radius of 1.25 cm, which surges to 684% at a radius of 0.25 cm. After the bending force is released, the resistance levels off at about 52% above the initial value, signalling a substantial residual shift and a partial inability to revert to the original state.

Figure 4-29 showcases the performance of a zigzag-patterned LIG sensor, fabricated under the same parameters and also transferred to a PU substrate. Here, resistance increases by 15% at a bending radius of 1.25 cm and by 69.5% at a 0.25 cm radius. Once bending ceases, the resistance stabilizes at 20.5% higher than the starting value, reflecting a less pronounced residual effect compared to the shutter pattern.

Figure 4-30 explores voltage signals after filtering at various bending radii, revealing significant differences between different radii. After removing the bending force, voltage drops but fails to return to its baseline. The sensor's high sensitivity allows precise detection of bending effects, yet the inability to fully recover underscores the persistent challenges in sensor design.

Figure 4-31 examines the zigzag-patterned sensor's response, where voltage changes at different bending radii are noticeable but show the lowest sensitivity of all tested patterns. Following force release, the voltage drops but remains high compared to the initial state. The similarity in voltage during bending at 1.25 cm and 1 cm, as well as post-bending, highlights the sensor's limitations, making it less practical for applications requiring full recovery.

**Electrical Resistance of Bending Actions From Flat to 1.25 mm Radius.  
(100-10-Shutter-PU)**



*Figure 4-28 Electrical resistance of LIG-PU shutter during bending (Flat to 1.25 mm radius, synthesized at speed 100 mm/s, power 10%).*

**Electrical Resistance of Bending Actions From Flat to 1.25 mm Radius.  
(100-10-Zigzag-PU)**

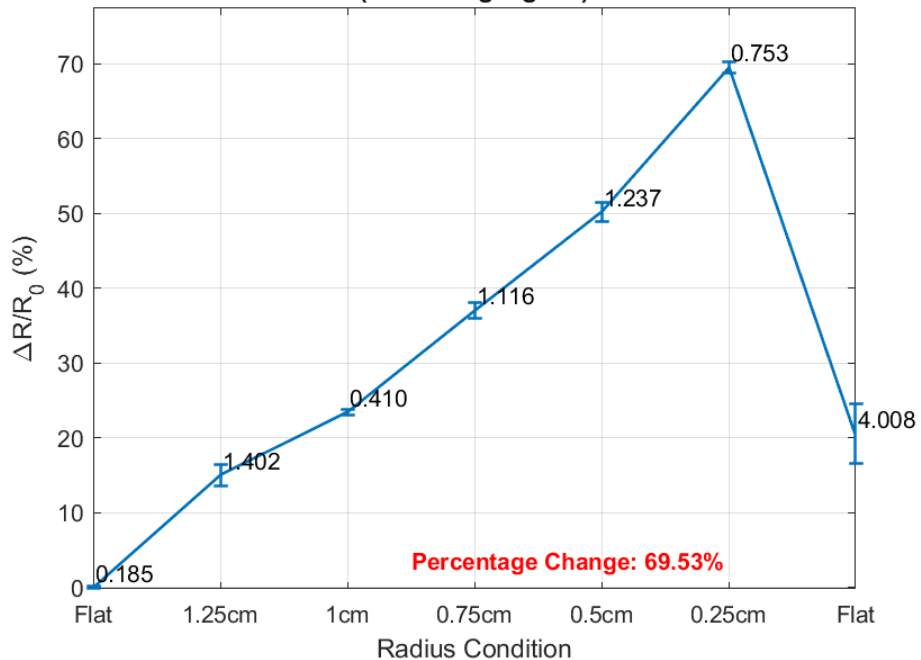


*Figure 4-29 Electrical resistance of LIG-PU zigzag during bending (Flat to 1.25 mm radius, synthesized at speed 100 mm/s, power 10%).*

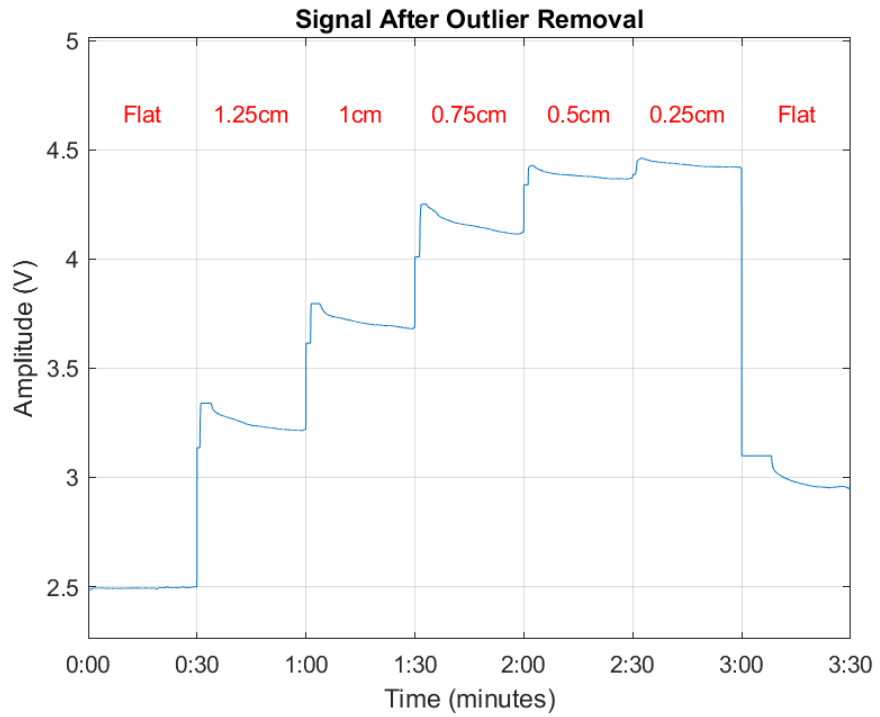


*Figure 4-30 Voltage of LIG-PU shutter at different bending radii  
(Signal after outlier removal, synthesized at speed 100 mm/s, power 10%).*

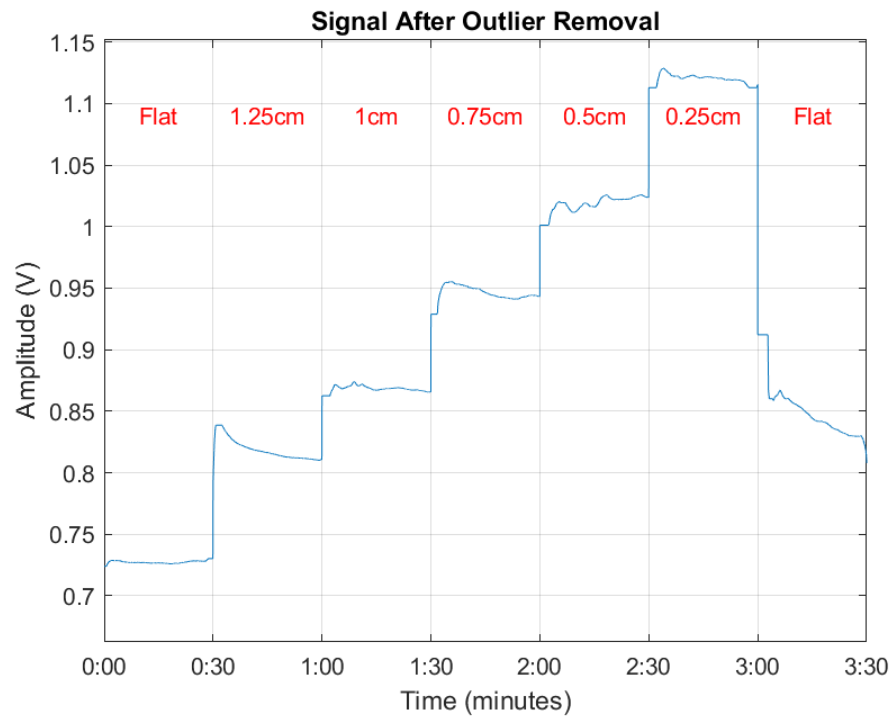


*Figure 4-31 Voltage of LIG-PU zigzag at different bending radii  
(Signal after outlier removal, synthesized at speed 100 mm/s, power 10%).*

Table 4-3 represents the performance characteristics of four distinct patterns—square, shutter, serpentine, and zigzag—under varying power and speed conditions on a PU substrate. The investigation measures three key parameters: percentage change, average resistance, and recovery rate. The data reveals complex relationships between pattern geometry, power input, and processing speed, offering insights into optimizing material processing techniques.

At low power (10%) and speed (100 mm/s), the square pattern exhibits an extraordinarily high percentage change (3,977.80%), far exceeding other patterns. This suggests that the square pattern is highly responsive to energy input under these conditions. As power and speed increase, the percentage change for all patterns decreases significantly, with the shutter pattern showing the highest values at higher settings (57.58% at 20/200).

The serpentine and zigzag patterns consistently demonstrate the highest average resistance across all conditions. At 10/100, the serpentine pattern shows  $1.5\text{ M}\Omega$  resistance, while the zigzag pattern reaches  $3.6\text{ M}\Omega$  at 15/200. In contrast, square and shutter patterns exhibit much lower resistance, generally from  $576\Omega$  to  $4,456\Omega$ . This stark difference suggests that serpentine and zigzag patterns might suit applications requiring high electrical or thermal insulation. In contrast, square and shutter patterns are ideal for low-power applications like sensing.

Recovery rates show less dramatic variations compared to other parameters. The Zigzag pattern generally exhibits the highest recovery rates, peaking at 79.5% at 10/100 and maintaining high rates across all conditions. The shutter pattern consistently shows the lowest recovery rates, ranging from 54.55% to 64.81%. This difference could be attributed to each pattern's unique structural properties.

Due to their high percentage change and low resistance, the LIG-PU square and shutter patterns will be utilized to evaluate healthcare applications. Their distinct characteristics make them particularly suited for this purpose, offering valuable insights into performance and reliability under varying conditions.

*Table 4-3 LIG-PU strain sensors evaluation with different patterns under various fabrication conditions.*

Power (%)	Speed (mm/s)	Pattern	Percentage Change in % (SD)	Average Resistance ( $\Omega$ ) (SD)	Recovery (%)
<b>10</b>	100	Square	3,977.80 (36.67)	576 (2)	76.78
<b>10</b>	100	Shutter	618.22 (35.09)	1,262 (1)	64.81
<b>10</b>	100	Serpentine	722.23 (17.22)	1.5 M (19,634)	Not available
<b>10</b>	100	Zigzag	69.53 (2.24)	170 k (314)	79.5
<b>15</b>	200	Square	18.21 (0.84)	4,456 (8)	68.28
<b>15</b>	200	Shutter	46.07 (3.26)	2,182 (2)	54.55
<b>15</b>	200	Serpentine	29.69 (1.93)	950 k (1,253)	73.94
<b>15</b>	200	Zigzag	20.76 (1.41)	3.6 M (4,832)	72.02
<b>20</b>	200	Square	22.77 (0.28)	3,565 (7)	74.62
<b>20</b>	200	Shutter	57.58 (4.45)	1,745 (2)	63.64
<b>20</b>	200	Serpentine	37.11 (1.89)	760 k (1,002)	79.15
<b>20</b>	200	Zigzag	25.95 (2.04)	2.9 M (3,866)	77.62

### **4.3. Performance of LIG-based Strain Sensors on protection tape, bandage, and PE nonwoven tape.**

The performance of LIG-based strain sensors was evaluated using different transfer materials: protection tape, bandage, and PE nonwoven tape. Each material exhibited unique characteristics affecting the sensor's sensitivity and functionality.

The protection tape, characterized by its high thickness, significantly compromised the sensor's sensitivity and recovery. Although the material is soft, its lack of stretchability prevents it from effectively conforming to the human body's contours—this mismatch between the sensor and the protection tape results in poor alignment and inaccurate strain measurements. Furthermore, the tape's inflexibility and thickness inhibit the sensor's ability to recover to its original state after deformation, leading to suboptimal performance.

The highly stretchable bandage shows promising initial performance for strain sensing. It can accommodate multiple stretches and return to its original length, demonstrating good elasticity. However, challenges arise during the pattern transfer process. The transfer of the LIG pattern onto the bandage is suboptimal, potentially due to inadequate pressure or temperature during the transfer process. As a result, while the sensor exhibits good sensitivity during the first bending cycle, its performance deteriorates with repeated cycles. After multiple deformations, the resistance increases significantly, often exceeding 1M ohm, rendering the sensor unreliable for continuous monitoring.

The PE nonwoven tape is stretchable but only within a limited range. Repeated stretching causes noticeable changes in the sensor's length from its initial state. This material's limited stretchability and the resulting elongation of the sensor affect its ability to maintain consistent performance. The changing size of the sensor upon stretching introduces variability in the resistance measurements, making it challenging to ensure accurate and reliable strain detection over time.

In summary, while each material has its advantages, they also present specific limitations that impact the performance of LIG-based strain sensors. Protection tape's thickness and rigidity result in poor sensitivity and recovery, bandage offers good initial performance but suffers from degradation with repeated use, and PE nonwoven tape's limited stretchability affects the sensor's length and measurement consistency. Addressing these challenges is crucial for improving the reliability and functionality of LIG-based strain sensors in practical applications. Further details and images of the sensors can be found in Appendix C.

#### **4.4. Application of LIG-based Strain Sensors.**

LIG-based strain sensors are emerging as a transformative technology in flexible and wearable electronics, providing exceptional capabilities for monitoring mechanical deformations with high sensitivity and adaptability. These sensors capitalize on LIG's outstanding electrical conductivity, mechanical flexibility, and lightweight properties, making them suitable for diverse applications. They are precious in health monitoring, where they can track physiological signals, including muscle movements, joint flexion, respiration, ECG, and arterial pulse. Moreover, LIG-based strain sensors offer a cost-effective and scalable solution for integration into soft robotics, electronic skins, and intelligent textiles, demonstrating their potential to revolutionize next-generation technologies that demand real-time, precise, and responsive strain detection.

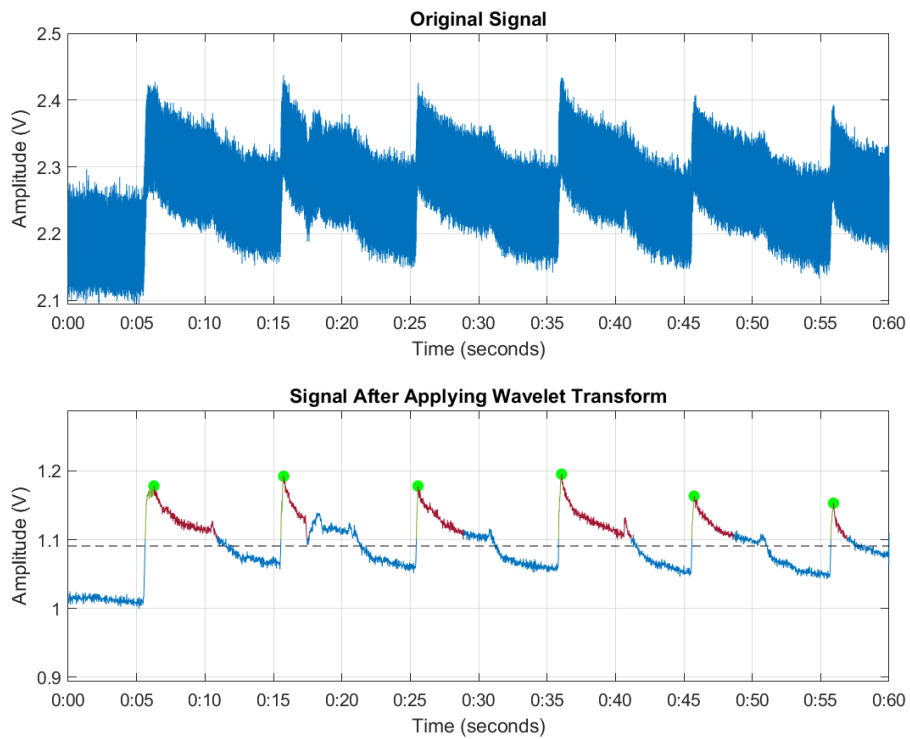
The third objective in this project focuses on developing a sensor to primarily detect arterial pulses and monitor various human motions, such as finger bending, hand gripping and releasing, and elbow flexion. If possible, the sensor will also be designed to capture additional physiological signals, such as ECG. Given their high sensitivity, LIG-PU sensors will primarily be focused on detecting human signals.

Figure 4-32 illustrates the voltage of a LIG-PU shutter sensor, synthesized at a speed of 200 mm/s and a laser power of 20%, during finger-bending activities. The figure captures the voltage changes during a series of finger-bending events: At 5 seconds, 15 seconds, and every subsequent 10 seconds.

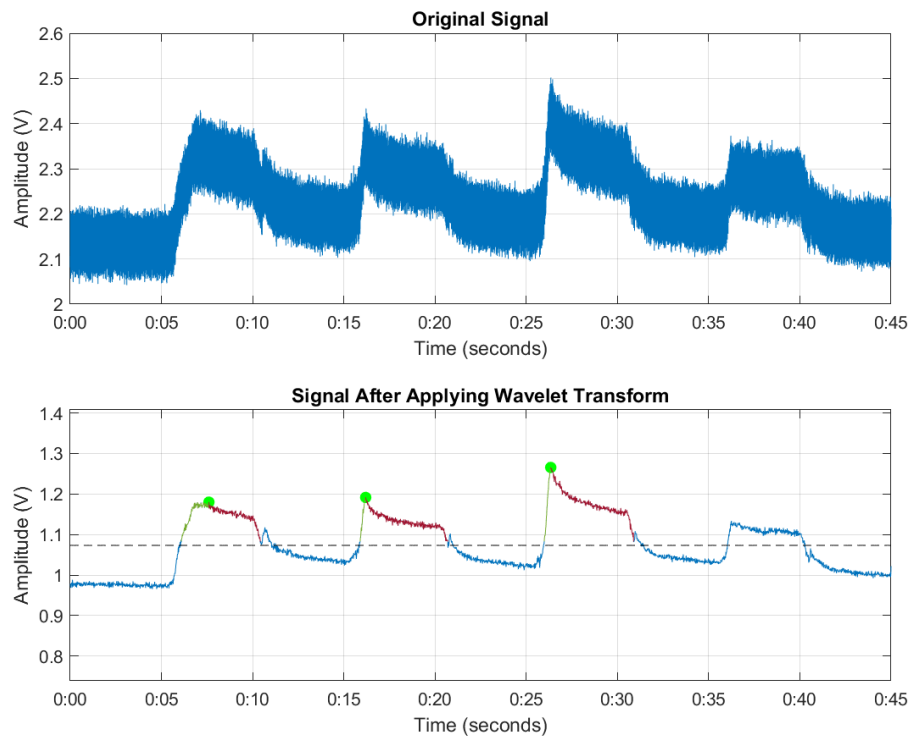
The bottom subplot shows the cleaned signal during finger bending and stretching, processed using wavelet decomposition and reconstruction. In this subplot, the green trendline illustrates the increase in voltage when the finger is bent. This increase is due to the sensor's resistance rising, which, according to Ohm's Law, causes a corresponding increase in the voltage reading. Conversely, the red trendline depicts the decrease in voltage as the finger is stretched, reflecting a return of the sensor's resistance to nearly its initial value.

Figure 4-33 illustrates the voltage of the same LIG-PU shutter sensor during elbow bending activities. The figure captures voltage variations at intervals of 5 seconds, 15 seconds, and every subsequent 10 seconds as the elbow is bent. In the plot, the green trendline indicates the periods of elbow bending, while the red trendline represents the elbow in its normal state.

The bottom subplot, which presents the filtered signal, highlights a significant challenge: at 35 seconds, the sensor's response to elbow bending is diminished due to lower sensitivity relative to the noise level. This reduced sensitivity may impair the sensor's ability to detect subtle resistance changes during elbow movements accurately, suggesting a potential limitation in its performance for this application.



*Figure 4-32 Voltage of LIG-PU shutter during finger bending  
(Synthesized at speed 200, power 20%).*



*Figure 4-33 Voltage of LIG-PU shutter during elbow bending  
(Synthesized at speed 200 mm/s, power 20%).*

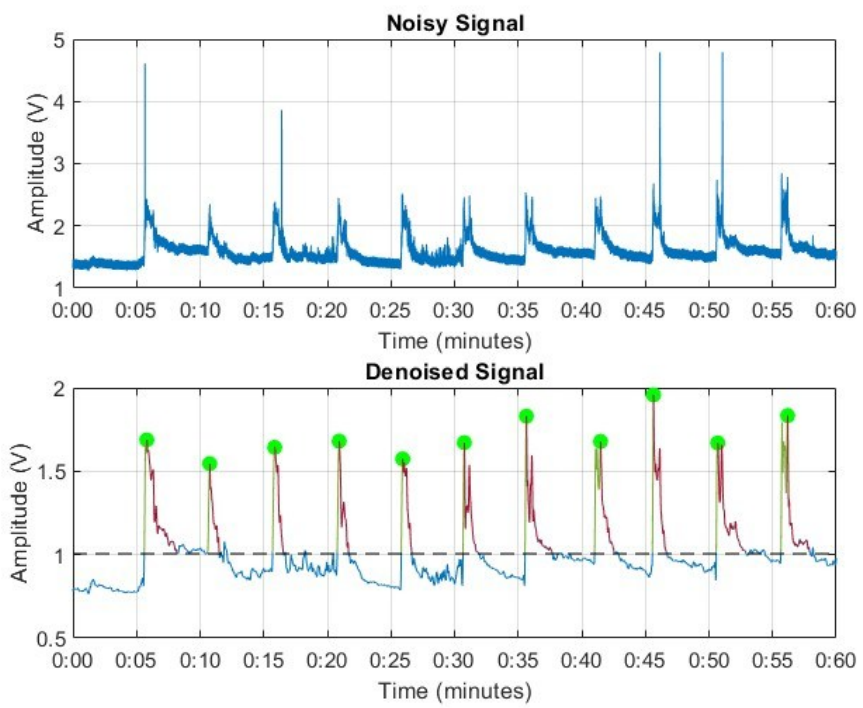
Figure 4-34 illustrates the voltage output of the LIG-PU square sensor, which was fabricated with 10% power and a scanning speed of 100 mm/s. This data was collected during a physical activity where the finger was bent to 30 degrees. The figure shows the voltage variations at intervals of 5 seconds, 10 seconds, and every subsequent 5 seconds as the finger is bent. The green trendline in the plot indicates periods of finger bending, while the red trendline represents the finger returning to its normal state.

Figure 4-35 shows the voltage recorded by the same sensor during finger bending at 90 degrees. The voltage change at 90 degrees is higher than at 30 degrees due to the increased force required to bend the finger further.

Table 4-4 represents the sensor's resistance change when bent at different angles. It provides data for two sensor patterns: shutter and square. The observed values illustrate the percentage change in resistance at various bending angles of 30°, 45°, and 90°.

At each bending angle, the square pattern exhibits a more significant change in resistance than the shutter pattern. For example, at a 30° bending angle, the square pattern shows a 105.73% change in resistance, whereas the shutter pattern shows a 45.36% change. This trend is consistent across all measured angles, indicating that the square pattern is more sensitive to bending than the shutter pattern.

Within each pattern, an increase in bending angle results in a more tremendous change in resistance. For instance, the resistance change moves from 45.36% at 30° to 70.52% at 90° for the shutter pattern and from 105.73% at 30° to 148.86% at 90° for the square pattern. This suggests that as the bending angle increases, the sensor experiences more significant changes in resistance, likely due to the increased strain or deformation on the sensor material. This implies that the square pattern may be more suitable for applications requiring higher sensitivity to bending or deformation.



*Figure 4-34 Voltage of LIG-PU square during finger bending at 30°  
(Synthesized at speed 100, power 10%).*

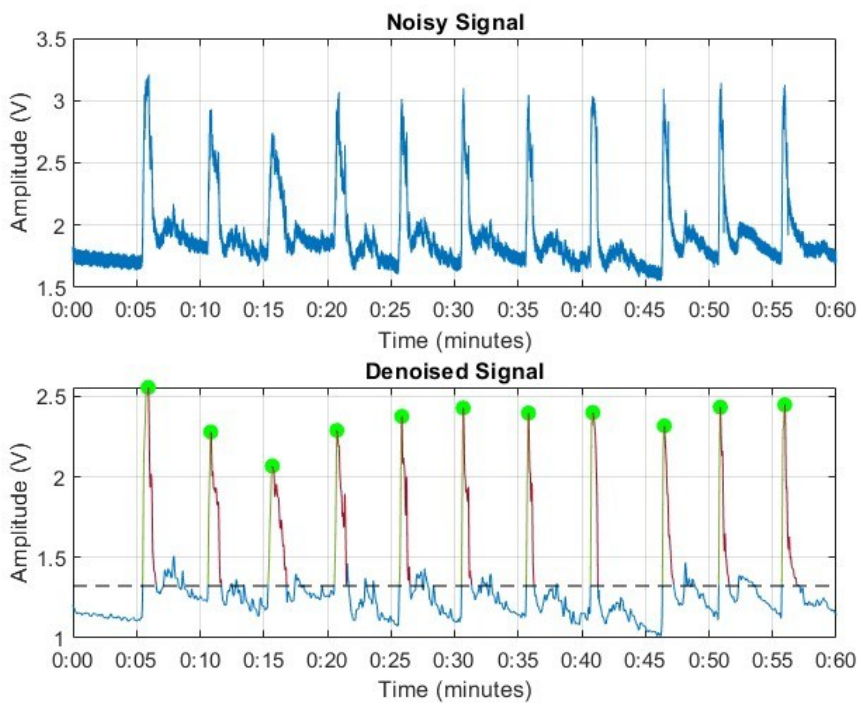


*Figure 4-35 Voltage of LIG-PU square during finger bending at 90°  
(Synthesized at speed 100, power 10%).*

*Table 4-4 Change in resistance of LIG-PU sensor at different finger bending angles.*

<b>Degree of bending angle (<math>\Theta</math>)</b>	<b>Change in Resistance</b>	
	Shutter	Square
<b>30</b>	45.36%	105.73%
<b>45</b>	60.30%	121.09%
<b>90</b>	70.52%	148.86%

Figure 4-36 illustrates the voltage change of the LIG-PU square sensor during hand grip and stretch activities over 60 seconds. The figure captures the sensor's response continuously, with hand grips occurring every 5 seconds and additional grips at 10 seconds, 15 seconds, and so on.

The graph shows distinct peaks corresponding to each hand grip event. These peaks represent significant increases in voltage due to the increased force applied during the grip. The data reveal that the resistance variation during hand gripping is 288.5% higher than the resistance change observed at a 90-degree finger bend. This substantial difference highlights that the force gripping the hand is significantly greater than that required for finger bending.

The green trendline in the figure represents the sensor's response during each hand grip. It shows how the sensor's voltage increases with each grip event, reflecting the sensor's sensitivity to the force applied. The red trendline depicts the sensor's response during the hand's return to the normal position after each grip, demonstrating how the sensor detects the return to baseline voltage levels.

The continuous capture of data over 60 seconds, with intermittent hand grips, demonstrates the LIG-PU sensor's ability to accurately track the intensity of hand grips and the recovery phases. This shows that the sensor effectively captures dynamic movements and varying force applications.

The LIG-PU sensor's ability to handle repeated hand grips and stretches makes it well-suited for integration into wearable devices like gloves. This capability could be leveraged to develop gesture recognition systems, which have potential applications in health care and rehabilitation.

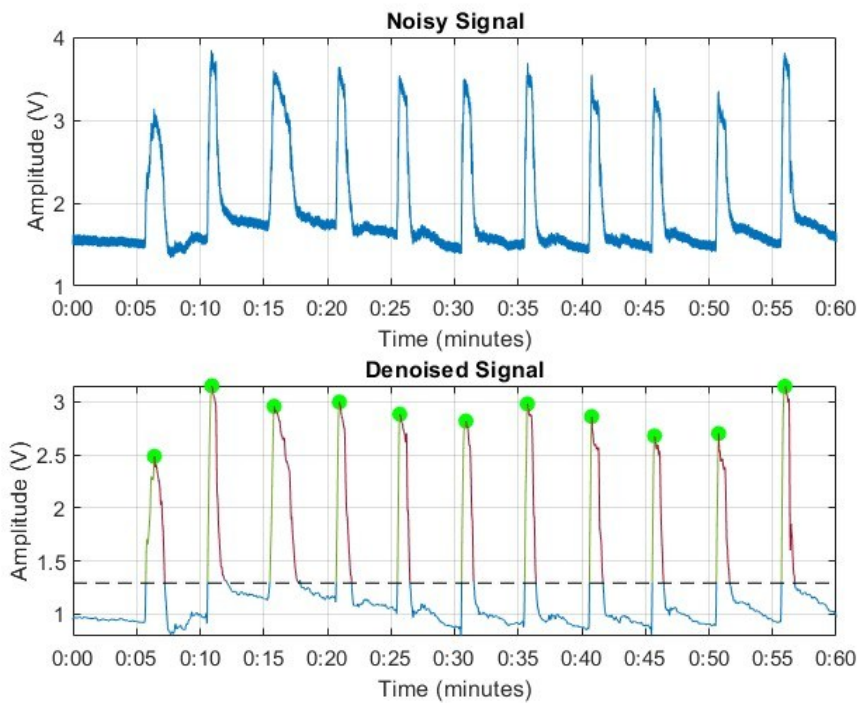


*Figure 4-36 Voltage of LIG-PU square during hand grip and stretch  
(Synthesized at speed 100 mm/s, power 10%).*

For pulse detection experiments, the initial attempts with the LIG-PU shutter sensor, synthesized at a scan speed of 200 mm/s and a laser power of 20%, were insufficient for reliably detecting arterial pulses. Therefore, the experiment continued with a revised LIG-PU shutter sensor fabricated at a slower scan speed of 100 mm/s and a reduced % laser power of 10%.

Figure 4-37 illustrates the collected signal, noise, and signal after applying a wavelet transformation. The wavelet transformation effectively removed the 50 Hz AC noise, which had obscured the arterial pulse. With the noise eliminated, the arterial pulse becomes visible, demonstrating the filter's effectiveness in isolating the pulse signal.

The bottom subplot depicts the signal after using a 0.5 Hz high-pass filter, which mitigates baseline shifts and stabilizes the signal, enhancing the clarity of the pulse peaks detection algorithm. Accurate peak detection is crucial for calculating heart rate, and these filtering techniques significantly aid in identifying the pulse peaks.

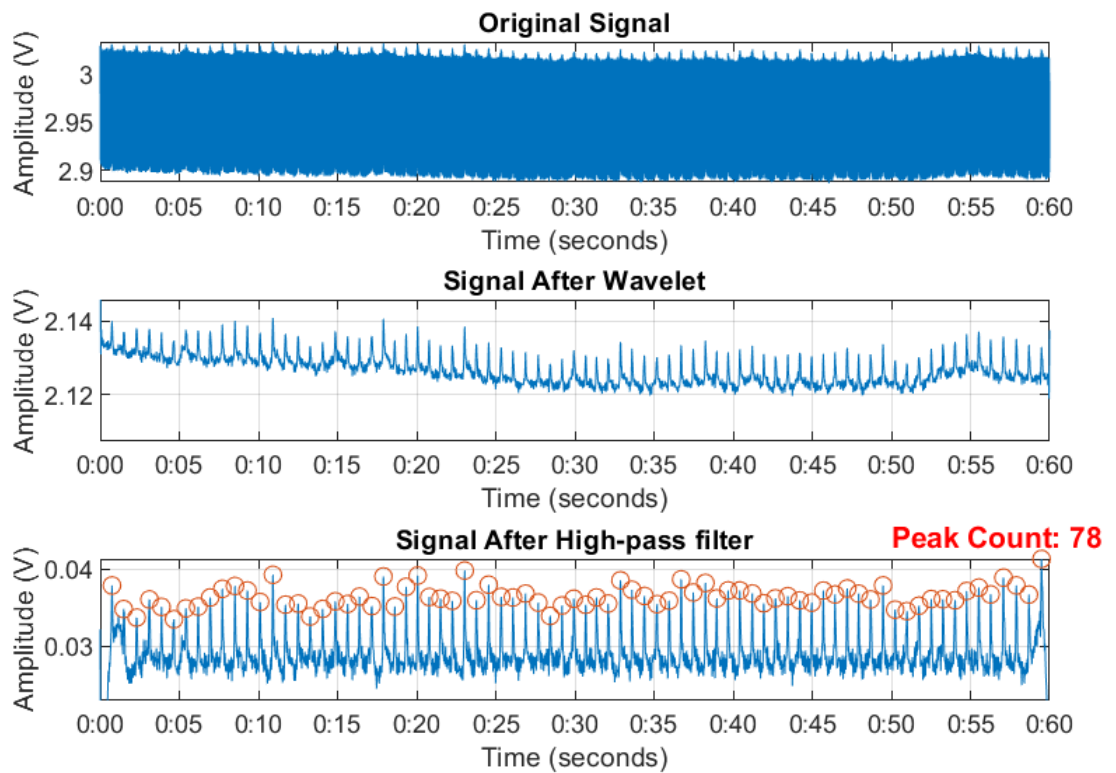
Figure 4-38 provides a detailed view of the signal from 30 to 35 seconds, highlighting the pulse characteristics. The accompanying algorithm analyzes pulse peaks, which are essential for heart rate calculation. Moreover, the experiment also included the LIG-PU square sensor, synthesized with the same parameters, which successfully detected the arterial pulse.

To evaluate performance differences, metrics such as sensitivity, positive predictive value, and accuracy will be compared between the LIG-PU shutter sensor and the LIG-PU square sensor. This comparison will help determine which sensor design is more effective for practical pulse detection applications.

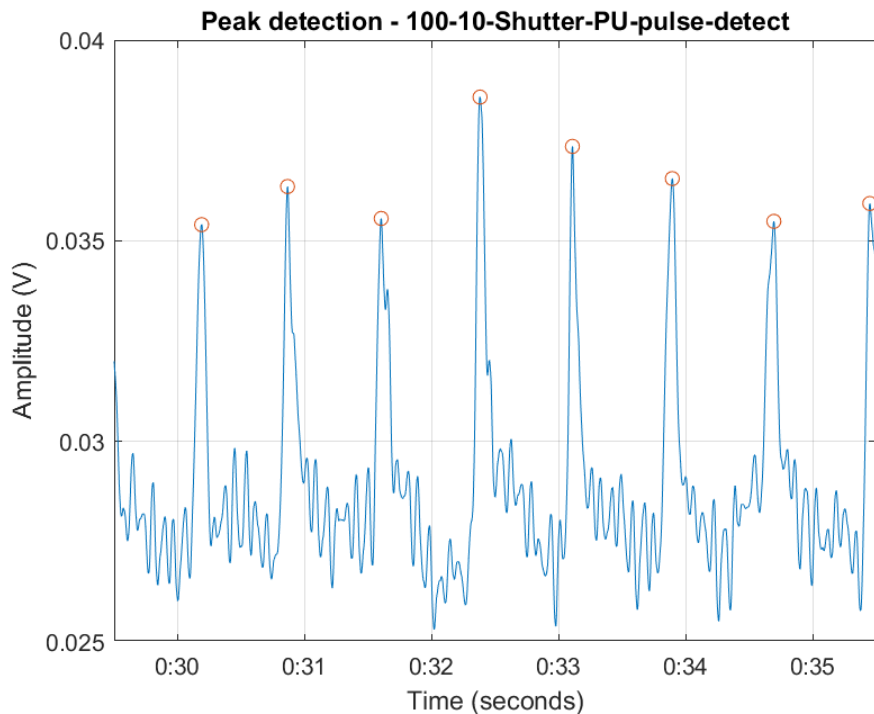
Figure 4-39 shows the voltage signals from the LIG-PU square and shutter sensors during pulse detection between 30 and 35 seconds. The LIG sensors were synthesized at a speed of 100 mm/s and a power setting of 10%. The signals are shown after filtering to eliminate baseline noise. The analysis indicates that both sensors effectively detect clear and distinct peaks, demonstrating their capability to capture pulse events accurately. The close alignment of peak patterns between the two sensors suggests that both accurately represent pulse characteristics within the observed time frame. The filtering method successfully reduced baseline drift and noise, ensuring that the peaks depicted represent genuine pulse events.

Table 4-3 compares pulse detection performance between LIG-PU shutter and square sensors fabricated at a scan speed of 100 mm/s and a laser power of 10%. The table includes critical performance metrics: True Positives (TP), False Positives (FP), False Negatives (FN), Sensitivity (Se), Positive Predictive Value (PP), and Accuracy (A). The LIG-PU shutter sensor achieved 784 true positives, 33 false positives, and three false negatives, resulting in a sensitivity of 99.62%, a positive predictive value of 95.96%, and an accuracy of 95.61%. In comparison, the LIG-PU square sensor recorded 796 true positives, 20 false positives, and one false negative, yielding a sensitivity of 99.84%, a positive predictive value of 97.55%, and an accuracy of 97.40%. The data indicate that while both sensor patterns perform exceptionally well, the LIG-PU square sensor slightly outperforms the LIG-PU shutter sensor regarding sensitivity, positive predictive value, and overall accuracy.

However, from the mean cross-correlation score, the LIG-PU shutter sensor has a score of 0.28 compared to 0.23 for the LIG-PU square sensor, suggesting that the LIG-PU shutter sensor may provide a more precise characterization of the waveform than the LIG-PU square sensor. A higher mean cross-correlation score typically indicates that the sensor's detected waveforms have a more consistent shape and are better aligned with the expected pulse characteristics. The data confirms that the LIG-PU square and shutter sensors perform well in pulse detection.



*Figure 4-37 Voltage of LIG-PU shutter during pulse detection (Original signal vs After filtering, Synthesized at speed 100 mm/s, power 10%)*



*Figure 4-38 Voltage of LIG-PU shutter during pulse detection (Signal after filtering, synthesized at speed 100 mm/s, power 10%, time duration: 30s to 35s).*

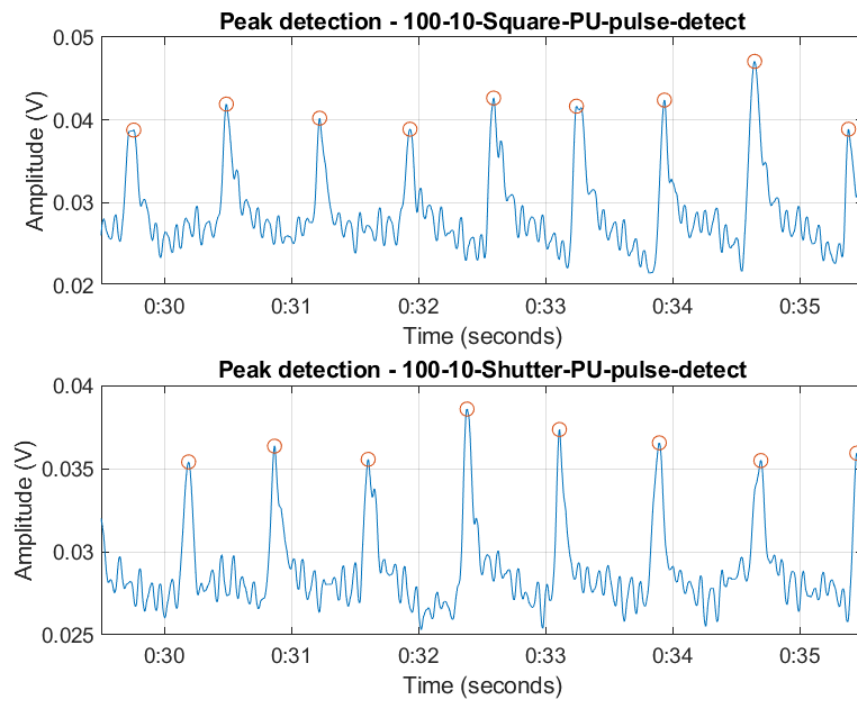


*Figure 4-39 Voltage comparison during pulse detection of LIG-PU square VS shutter (Signal after filtering, synthesized at speed 100 mm/s, power 10%, time duration: 30s to 35s).*

*Table 4-5 Pulse detection performance comparison of LIG-PU shutter and square sensors fabricated at 100 mm/s and 10% power.*

<b>LIG-PU-100-10</b>		
	Shutter	Square
<b>TP</b>	784	796
<b>FP</b>	33	20
<b>FN</b>	3	1
<b>Se</b>	99.62	99.84
<b>PP</b>	95.96	97.55
<b>A</b>	95.61	97.40
<b>Mean Cross-Correlation</b>	0.28	0.23
<b>SD of Cross-Correlation</b>	0.103	0.087

The LIG-ECG electrodes are connected to the ECG cable via snap buttons for ECG detection. Two types of LIG-ECG electrodes are created by engraving a PI sheet with a laser at different power levels: 8% and 10%, with a scanning speed of 100 mm/s. The electrodes feature two distinct patterns: circular and fractal-like. The ECG measurements are conducted over 2 minutes, as described in the ethical protocol, with only the middle 1-minute segment being analyzed to ensure stable data collection. This experiment was repeated ten times to determine the best-performance electrode configuration. Figure 4-40 illustrates the LIG-ECG electrodes used in the study. Figure 4-40a shows the electrode with a circular pattern, while Figure 4-40b displays the fractal-like pattern. Figure 4-40c depicts how the electrodes are connected to the ECG cables.

During ECG measurements, the side of the electrode with graphene contacts the skin. Due to the specific properties of LIG-PI at 10% power, no black ash residue is left on the skin, and the electrodes remain blackened. Zooming into Figures 4-40a and 4-40b reveals the snap button traces on the electrodes used in the experiment, whereas Figure 4-40c shows the unused electrodes.

Figure 4-41 presents the voltage of the ECG signal recorded using the DFROBOT SEN0213, which incorporates an AD8232 chip designed for heart rate monitoring. The top subplot shows the raw ECG signal, which contains noise and baseline wander, common artifacts in ECG recordings due to patient movement, respiration, or other external factors. The bottom subplot displays the cleaned signal after applying wavelet transformation.

Wavelet transformation is an effective method for ECG signal denoising as it separates signal components at different scales. This technique is particularly suitable for removing high-frequency noise while preserving the critical features of the ECG, such as the P-wave, QRS complex, and T-wave. After wavelet reconstruction, the signal is further processed using a 0.5 Hz high-pass filter to eliminate baseline drift, a low-frequency artifact that can obscure the valid ECG signal. The cleaned ECG signal, shown in the figure, effectively highlights the key features, with green dots marking the peaks of the QRS complexes.

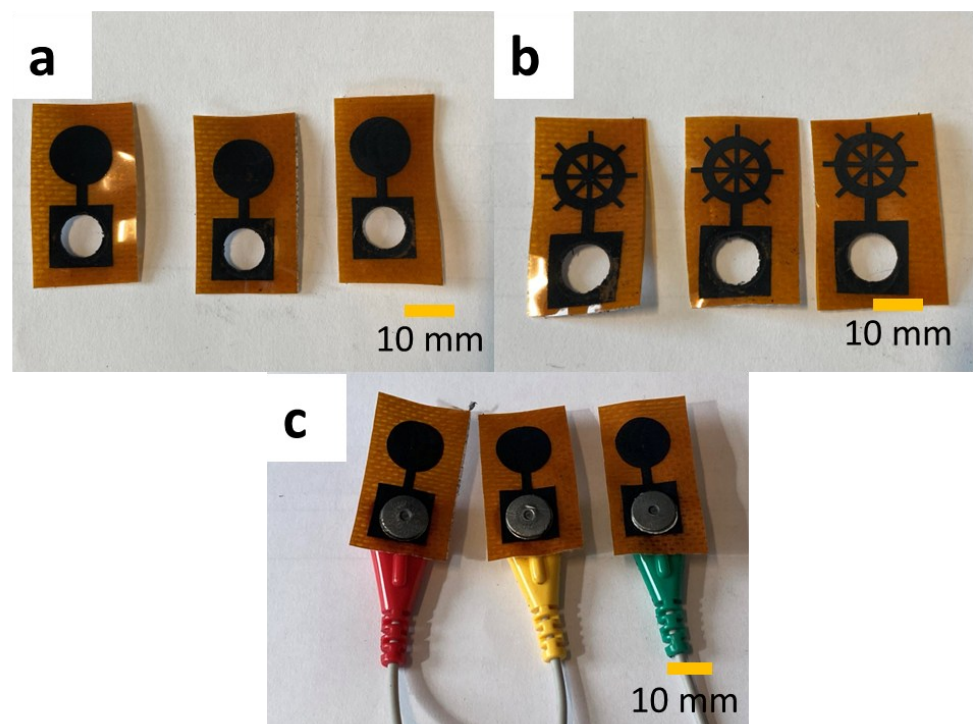


*Figure 4-40 LIG-ECG Electrodes with circular and fractal-like patterns  
(a) LIG-ECG electrodes with circular pattern, (b) LIG-ECG electrodes with fractal-like pattern, (c) ECG electrodes connected to ECG cables.*

Figure 4-42 provides a zoomed-in view of the ECG signal from 30 to 33 seconds, allowing for a closer examination of its characteristics. In this subplot, the P-wave, QRS complex, and T-wave are clearly visible:

- P-Wave: Represents atrial depolarization, indicating the onset of atrial contraction.
- QRS Complex: Corresponds to ventricular depolarization and is the most significant feature in ECG signal analysis due to its high amplitude and sharpness.
- T-Wave: Reflects ventricular repolarization, which follows the QRS complex.

The red circles highlight the peaks of the QRS complexes, while the green lines represent the ascending segment (QR) and the red lines denote the descending segment (RS) of the QRS complex. Identifying these features is crucial for detecting arrhythmias and other heart conditions.

Figure 4-43 presents a comparison of the voltage output from two types of LIG-ECG electrodes, both fabricated at the same laser power (10%) and scanning speed (100 mm/s), but with different patterns: a fractal-like pattern and a circular pattern. The top subplot illustrates the voltage signal captured by the electrode with a fractal-like pattern. This electrode successfully detects all QRS complexes, which are critical for identifying heartbeats, and shows the P-wave and T-wave, though these latter waves are less distinct compared to the QRS complex.

In contrast, the bottom subplot shows the voltage signal from the circular pattern electrode. This electrode also captures the QRS complexes; however, there are two false positives where the T-wave peaks are mistakenly detected as QRS complexes due to their relatively high amplitude. This misidentification of the T-wave as the QRS complex is a significant issue observed in this study, as the T-waves are unusually larger than the QRS complexes, leading to erroneous peak detection.

While these two figures provide insights into the performance of the electrodes with different patterns, they alone are not sufficient to fully summarize the performance across all tested electrode types. Table 4-6 offers a comprehensive performance summary of the four types of LIG-ECG electrodes used in this work, fabricated with different laser power settings (8% and 10%) and patterns (circular and fractal-like) at a scanning speed of 100 mm/s.

The table includes key performance metrics such as true positives, false positives, and false negatives, along with selectivity, positive predictive value, accuracy, and the mean cross-correlation score.

The results indicate that the LIG-ECG electrode fabricated with a circular pattern at 100 mm/s speed and 10% power demonstrates the highest overall performance in terms of selectivity (99.6%), positive predictive value (99.2%), and accuracy (98.8%). However, despite its superior performance in these metrics, this electrode exhibits the lowest mean cross-correlation score of 0.12, with a SD of 0.04. A lower mean cross-correlation score suggests less consistency in waveform morphology when compared to a standard ECG template, indicating variability in the recorded signals.

In comparison, the fractal-like pattern electrodes (both 8% and 10% power) display slightly lower selectivity (95.3% and 99.4%, respectively) and accuracy (90.6% and 98.5%, respectively) but achieve higher mean cross-correlation scores (0.15 and 0.13, respectively). This suggests that the fractal patterns might provide more consistent waveform shapes but with slightly less overall signal accuracy and selectivity.

These findings underscore the trade-offs between different electrode designs:

- **Circular Pattern Electrodes:** Offer superior detection performance but may suffer from misidentification issues, particularly when T-wave amplitudes are larger than those of the QRS complex.
- **Fractal Pattern Electrodes:** Provide more consistent signal morphology, as indicated by higher mean cross-correlation scores, but may not perform as well in terms of overall detection accuracy and selectivity.

Thus, while the circular pattern electrode at 10% power and 100 mm/s speed ranks highest in terms of selectivity, positive predictive value, and accuracy, careful consideration is needed for its application, especially in scenarios where distinguishing between T-waves and QRS complexes is critical.

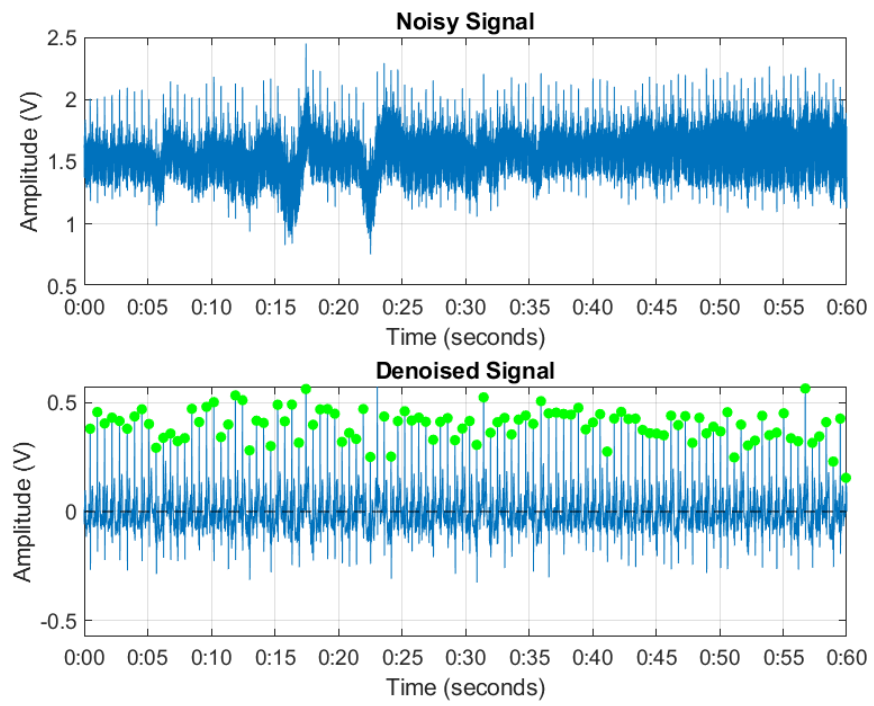


*Figure 4-41 ECG signal processing: raw and denoised signals using wavelet transformation and high-pass filter (LIG-PI-Circle fabricated at 100 mm/s and 8% power).*

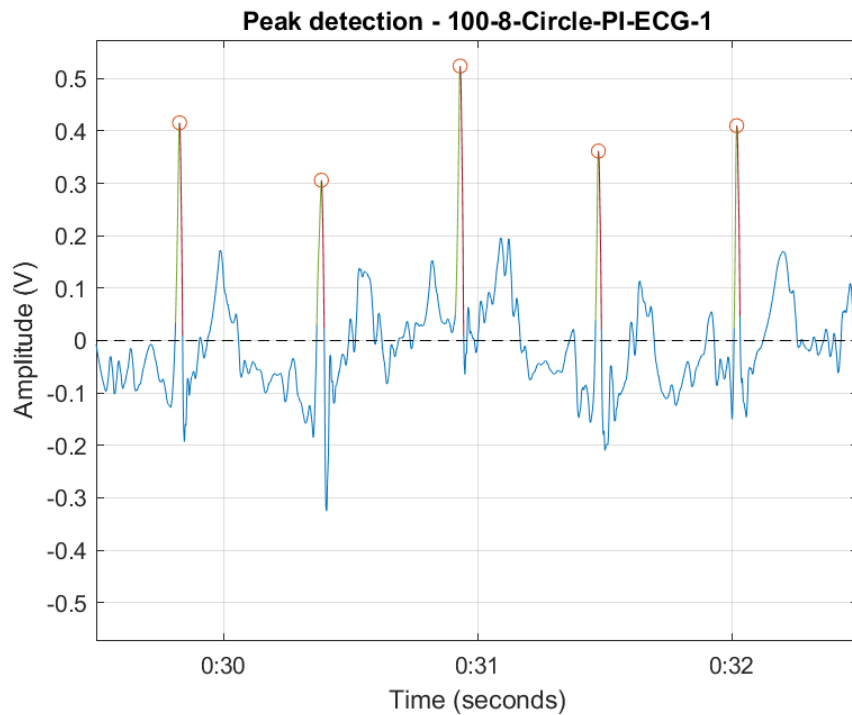


*Figure 4-42 Zoomed view of ECG signal features: P-wave, QRS complex, and T-wave identification.*

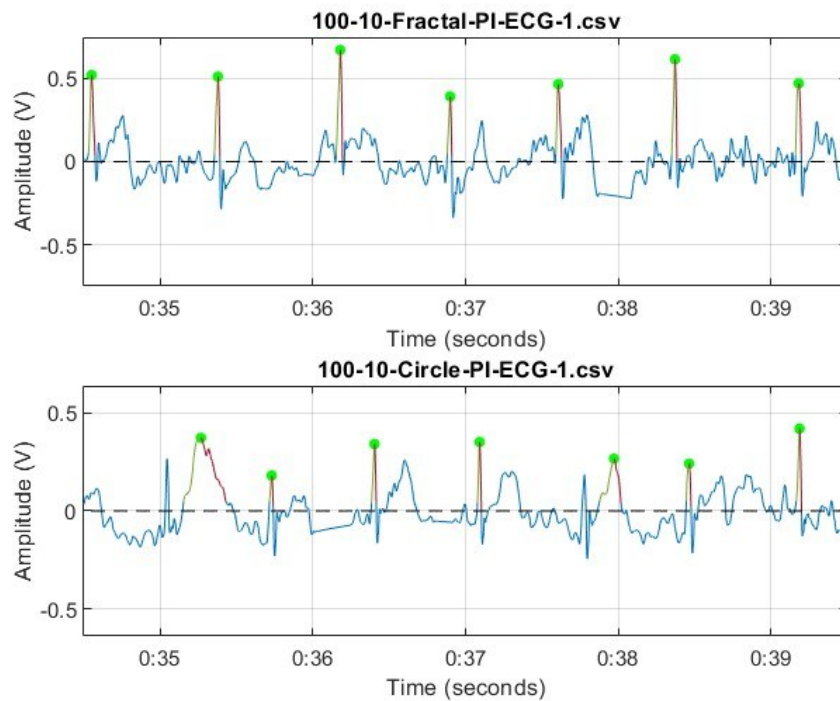


*Figure 4-43 Comparison of ECG signal features between circular and fractal-like patterns on PI substrates (100 mm/s, 10% Power): P-Wave, QRS Complex, and T-Wave identification.*

*Table 4-6 Performance comparison of LIG-ECG electrodes with different patterns and power settings: true positives, false positives, false negatives, and cross-correlation scores.*

	100-8- Circle	100-10- Circle	100-8- Fractal	100-10- Fractal
<b>TP</b>	1012	625	819	805
<b>FP</b>	8	43	45	7
<b>FN</b>	4	42	40	5
<b>Se</b>	99.6	93.7	95.3	99.4
<b>PP</b>	99.2	93.6	94.8	99.1
<b>A</b>	98.8	88.0	90.6	98.5
<b>Mean Cross-Correlation</b>	0.12	0.14	0.15	0.13
<b>SD of Cross-Correlation</b>	0.04	0.03	0.03	0.07

## 5. CONCLUSIONS AND FURTHER WORK

To summarize, the electrical properties of LIG are influenced by several independent factors, including laser power, scanning speed, and sensor pattern. Additionally, the choice of substrate is crucial in the synthesis of LIG. Each substrate investigated—PI film, medical tape, PU tape, bandage, and silicone protection tape—offers unique benefits for LIG synthesis, highlighting the importance of substrate selection in optimizing the performance and characteristics of LIG-based sensors. Among these, LIG transferred to PU tape has proven to be the most effective for strain sensing applications.

Moving forward, it is essential to identify substrates that can be effectively employed in real-life applications for detecting physiological signals. The signals of interest include human motion detection (e.g., finger bending, hand grip for gesture recognition) and arterial pulse (for calculating heart rate and blood pressure). Additionally, ECG electrodes made from PI at power levels lower than 10% have successfully detected ECG signals.

Due to equipment and time constraints, some electrical measurements, such as resistance testing under strain, were not performed. Furthermore, a detailed evaluation of the sensor's micromorphology was not conducted, which could have offered deeper insights into the sensor's behaviour and performance.

To enhance the performance of synthesized LIG sensors, it is advisable to extend their evaluation to include additional physiological signals, such as breath sensing and monitoring blood glucose levels from tears and sweat. Furthermore, exploring novel substrate materials that offer desirable characteristics like mechanical flexibility and biocompatibility could lead to identifying substrates better suited for specific applications in physiological signal detection. This approach aims to broaden the capabilities and versatility of LIG-based sensors, facilitating advancements in biomedical and wearable technology fields.

Enhancing sensitivity and selectivity in LIG sensors through optimizing sensor design, electrode arrangement, and signal processing algorithms is essential for improving signal detection capabilities. Additionally, comprehensive validation studies across various real-world scenarios are crucial to validate the reliability, accuracy, and resilience of LIG sensors in biomedical applications.

## 6. REFERENCES

- [1] M. Yi and Z. Shen, “A review on mechanical exfoliation for the scalable production of graphene”, *Journal of Materials Chemistry A*, vol. 3, no. 22, pp. 11700–11715, 2015.
- [2] H. Ye, X. Zhang, Y. Zhu, C. Xu, and L. Xu, “High energy density in poly(vinylidene fluoride-chlorotrifluoroethylene) nanocomposite with oriented graphene exfoliated with assistance of fluoro hyperbranched copolymer”, *Energy Technology*, vol. 7, no.9, pp. 1900023, 2019.
- [3] P. R. Somani, S. P. Somani, and M. Umeno, “Planer nano-graphenes from camphor by CVD”, *Chemical Physics Letters*, , vol. 430, no. 1-3, pp. 56-59, 2006.
- [4] Q. Yu, J. Lian, S. Siriponglert, H. Li, Y. P. Chen, and S. S. Pei, “Graphene segregated on Ni surfaces and transferred to insulators”, *Applied Physics Letters*, vol. 93, no. 11, pp. 113103, 2008.
- [5] W. Strupinski, K. Grodecki, A. Wysmolek, R. Stepniewski, T. Szkopek, P. E. Gaskell, A. Grüneis, D. Haberer, R. Bozek, J. Krupka, and J. M. Baranowski, “Graphene Epitaxy by Chemical Vapor Deposition on SiC”, *Nano Letters*, vol. 11, no. 4, pp. 1786-1791, 2011.
- [6] Y. B. Mollamahale, M. Ghorbani, A. Dolati, and D. Hosseini, “Electrodeposition of well-defined gold nanowires with uniform ends for developing 3D nanoelectrode ensembles with enhanced sensitivity”, *Materials Chemistry and Physics*, vol. 219, pp. 67-75, 2018.
- [7] A. Lamberti, F. Clerici, M. Fontana, and L. Scaltrito, “A highly stretchable supercapacitor using laser-induced graphene electrodes onto elastomeric substrate”, *Advanced Energy Materials*, vol. 6, no. 10, pp. 160005, 2016.
- [8] J. Lin, Z. Peng, Y. Liu, et al., “Laser-induced porous graphene films from commercial polymers”, *Nature Communications*, vol. 5, pp. 5714, 2014.

- [9] HR. Moon and B. Ryu, “Review of laser-induced graphene (LIG) produced on eco-friendly substrates”, *Int. J. of Precis. Eng. and Manuf.-Green Tech.*, vol. 11, pp. 1279–1294, 2024.
- [10] Y. Guo, C. Zhang, Y. Chen, and Z. Nie, “Research progress on the preparation and applications of laser-induced graphene technology”, *Nanomaterials*, vol. 12, no. 14, pp. 2336, 2022.
- [11] L. Wang, Zh. Wang, A. N. Bakhtiyari, and H. Zheng, “A comparative study of laser-induced graphene by CO<sub>2</sub> infrared laser and 355 nm ultraviolet (UV) laser”, *Micromachines*, vol. 11, no.12, pp. 1094, 2020.
- [12] B.S. Shin, J.Y. Oh a, and H. Sohn, “Theoretical and experimental investigations into laser ablation of polyimide and copper films with 355-nm Nd:YVO<sub>4</sub> laser”, *Journal of Materials Processing Technology*, vol. 187, pp. 260-263, 2007.
- [13] R. Mukherjee, A.V. Thomas, A. Krishnamurthy, and N. Koratkar, “Photothermally reduced graphene as high-power anodes for lithium-ion batteries”, *ACS Nano*, vol. 6, no. 9, pp. 7867-7878, 2012.
- [14] G. Lia, “Direct laser writing of graphene electrodes”, *Journal of Applied Physics*, vol. 127, pp. 010901, 2020.
- [15] Z. Zhang, H. Zhu, W. Zhang, Z. Zhang, J. Lu, K. Xu, Y. Liu, and V. Saetang, “A review of laser-induced graphene: From experimental and theoretical fabrication processes to emerging applications”, *Carbon*, vol. 214, pp. 118356, 2023.
- [16] N. Dixit and S. P. Singh, “Laser-induced graphene (LIG) as a smart and sustainable material to restrain pandemics and endemics: A perspective”, *ACS Omega*, vol. 7, no.6, pp. 5112-5130, 2022.
- [17] A. F. Carvalho, A. J. S. Fernandes, C. Leitão, J. Deuermeier, A. C. Marques, R. Martins, E. Fortunato, and F. M. Costa, “Laser-induced graphene strain sensors produced by ultraviolet irradiation of polyimide”, *Advanced Functional Materials*, vol. 28, no. 52, pp. 180527, 2018.

- [18] V. Fiodorov, R. Trusovas, Z. Mockus, K. Ratautas, and G. Račiukaitis, “Laser-induced graphene formation on polyimide using UV to mid-infrared laser radiation”, *Polymers*, vol. 15, no. 21, pp. 4229, 2023.
- [19] H. Yu, M. Gai, L. Liu, F. Chen, J. Bian, and Y. Huang, “Laser-induced direct graphene patterning: From formation mechanism to flexible applications”, *Soft Science*, vol. 3, no. 1, pp. 4, 2023.
- [20] S. Luo, P. T. Hoang, and T. Liu, “Direct laser writing for creating porous graphitic structures and their use for flexible and highly sensitive sensor and sensor arrays”, *Carbon*, vol. 96, pp. 522-531, 2016.
- [21] L. X. Duy , Z. Peng , Y. Li , J. Zhang , Y. Ji, and J. M. Tour, “Laser-induced graphene fibers”, *Carbon*, vol. 126, pp. 472-479, 2018.
- [22] Z. Wang, G. Wang, W. Liu, B. Hu, J. Liu, and Y. Zhang, “Patterned laser-induced graphene for terahertz wave modulation”, *Journal of the Optical Society of America B*, vol. 37, no. 2, pp. 546-551, 2020.
- [23] X. Xing, Y. Zou, M. Zhong, S. Li, H. Fan, X. Lei, J. Yin, J. Shen, X. Liu, M. Xu, et al., “A flexible wearable sensor based on laser-induced graphene for high-precision fine motion capture for pilots”, *Sensors*, vol. 24, no. 4, pp. 1349, 2024.
- [24] H. Wang, Z. Zhao, P. Liu, and X. Guo., “A soft and stretchable electronics using laser-induced graphene on polyimide/PDMS composite substrate”, *npj Flex Electronics*, vol. 6, pp. 26, 2022.
- [25] S. Jindal, R. Anand, N. Sharma, N. Yadav, D. Mudgal, R. Mishra, and V. Mishra, “Sustainable approach for developing graphene-based materials from natural resources and biowastes for electronic applications”, *ACS Applied Electronic Materials*, vol 4, no. 5, pp. 2146-2174, 2022.
- [26] S. Liu, R. Chen, R. Chen, C. Jiang, C. Zhang, D. Chen, W. Zhou, S. Chen, and T. Luo, “Facile and cost-effective fabrication of highly sensitive, fast-response flexible humidity sensors enabled by laser-induced graphene”, *ACS Applied Materials & Interfaces*, vol. 15, pp. 57327–57337, 2023.

- [27] B. Sindhu, A. Kothuru, P. Sahatiya, S. Goel, and S. Nand, “Laser-induced graphene printed wearable flexible antenna-based strain sensor for wireless human motion monitoring”, *IEEE Transactions on Electron Devices*, vol. 68, no. 7, pp. 3189-3194, 2021.
- [28] A. F. Carvalho, A. J. S. Fernandes, C. Leitão, J. Deuermeier, A. C. Marques, R. Martins, E. Fortunato, F. M. Costa, “Laser-induced graphene strain sensors produced by ultraviolet irradiation of polyimide”, *Advanced Functional Materials*, vol. 28, no. 52, pp. 1805271, 2018.
- [29] M. T. Gilavan, M. S. Rahman, A. M-Khan, S. Nambi, and G. Grau, “One-step fabrication of low-resistance conductors on 3d-printed structures by laser-induced graphene”, *ACS Applied Electronic Materials*, vol. 3, no. 9, pp. 3867, 2021.
- [30] Q. Li, T. Wu, W. Zhao, J. Ji, and G. Wang, “Laser-induced corrugated graphene films for integrated multimodal sensors”, *ACS Applied Materials & Interfaces*, vol. 13, no.31, pp. 10210, 2021.
- [31] B. Kulyk, B. F. R. Silva, A. F. Carvalho, P. Barbosa, A. V. Girão, J. Deuermeier, A. J. S. Fernandes, F. M. L. Figueiredo, E. Fortunato, and F. M. Costa, “Laser-induced graphene from paper by ultraviolet irradiation: humidity and temperature sensors”, *Advanced Materials Technologies*, vol. 7, no. 7, pp. 2101311, 2022.
- [32] W. Yang, W. Zhao, Q. Li, H. Li, Y. Wang, Y. Li, and G. Wang., “Fabrication of smart components by 3D printing and laser-scribing technologies”, *ACS Applied Materials & Interfaces*, vol. 12, no. 3, pp. 3928, 2020
- [33] T.-S. D. Le, S. Park, J. An, P. S. Lee, and Y.-J. Kim, “Ultrafast laser pulses enable one-step graphene patterning on woods and leaves for green electronics”, *Advanced Functional Materials*, vol. 29, no. 33, pp. 1902771, 2019
- [34] Q. Li, T. Wu, W.Zhao, J. Ji, and G. Wang, “Laser-induced corrugated graphene films for integrated multimodal sensors”, *ACS Applied Materials & Interfaces*, vol. 13, no. 31, pp. 37433, 2021

- [35] Z. Zhang, M. Song, J. Hao, K. Wu, C. Li, and C. Hu, “Visible light laser-induced graphene from phenolic resin: A new approach for directly writing graphene-based electrochemical devices on various substrates”, *Carbon*, vol. 127, pp. 287-296, 2018.
- [36] R. D. Rodriguez, S. Shchadenko, G. Murastov, A. Lipovka, M. Fatkullin, I. Petrov, T.-H. Tran, A. Khalelov, M. Saqib, N. E. Villa, V. Bogoslovskiy, Y. Wang, C.-G. Hu, A. Zinovyev, W. Sheng, J.-J. Chen, I. Amin, and E. Sheremet, “Ultra-robust flexible electronics by laser-driven polymer-nanomaterials integration”, *Advanced Functional Materials*, vol. 31, no. 17, pp. 2008818, 2021.
- [37] A. Lamberti, M. Serrapede, G. Ferraro, M. Fontana, F. Perrucci, S. Bianco, A. Chiolerio, and S. Bocchini, “All-SPEEK flexible supercapacitor exploiting laser induced graphenization”, *2D Mater*, vol. 4, pp. 035012, 2017.
- [38] Y. Song, J. Zhang, N. Li, S. Han, S. Xu, J. Yin, W. Qu, C. Liu, S. Zhang, and Z. Wang, “Design of a high performance electrode composed of porous nickel–cobalt layered double hydroxide nanosheets supported on vertical graphene fibers for flexible supercapacitors”, *New Journal of Chemistry*, vol. 44, pp. 6623, 2020.
- [39] Y.-R. Chen, K.-F. Chiu, H. C. Lin, C.-L. Chen, C. Y. Hsieh, C. B. Tsai, and B. T. T. Chu, “Graphene/activated carbon supercapacitors with sulfonated-polyetheretherketone as solid-state electrolyte and multifunctional binder”, *Solid State Sciences*, vol. 37, pp. 80-85, 2014.
- [40] H. Wang, H. Wang, Y. Wang, X. Su, C. Wang, M. Zhang, M. Jian, K. Xia, X. Liang, H. Lu, S. Li, and Y. Zhang, “Laser writing of janus graphene/kevlar textile for intelligent protective clothing”, *ACS Nano*, vol. 14, no. 3, pp. 3219-3226, 2020.
- [41] Y.-J. Kima, D. Yanga, H. K. Nama, T.-S. Dinh Lea, Y. Leea, and S. Kwonb, “Direct-laser-conversion of Kevlar textile to laser-induced-graphene for realizing fast and flexible fabric strain sensors”, *CIRP Annals - Manufacturing Technology*, vol. 71, pp. 473-476, 2022.
- [42] R. Ye, Y. Chyan, J. Zhang, Y. Li, X. Han, C. Kittrell, J. M. Tour, “Laser-induced graphene formation on wood”, *Advanced Materials*, vol. 29, no. 37, pp. 1702211, 2017.

- [43] L.-Q. Tao, H. Tian, Y. Liu, et al., “An intelligent artificial throat with sound-sensing ability based on laser induced graphene”, *Nature Communications*, vol. 8, pp. 14579, 2017.
- [44] Z. Li, L. Lu, Y. Xie, W. Wang, Z. Lin, B. Tang, and N. Lin, “Preparation of laser-induced graphene fabric from silk and its application examples for flexible sensor”, *Advanced Engineering Materials*, vol. 23, no. 9, pp. 2100195, 2021.
- [45] D. Yang, H. K. Nam, T.-S. D. Le, J. Yeo, Y. Lee, Y.-R. Kim, S.-W. Kim, H.-J. Choi, H. C. Shim, S. Ryu, S. Kwon, and Y.-J. Kim, “Multimodal e-textile enabled by one-step maskless patterning of femtosecond-laser-induced graphene on nonwoven, knit, and woven textiles”, *ACS Nano*, vol. 17, pp. 18893-18904, 2023.
- [46] X. Xing, Y. Zou, M. Zhong, S. Li, H. Fan, X. Lei, J. Yin, J. Shen, X. Liu, M. Xu, et al. “A flexible wearable sensor based on laser-induced graphene for high-precision fine motion capture for pilots”, *Sensors*, vol. 24, pp. 1349, 2024.
- [47] R. Murray, M. Burke, D. Iacopino, and A. J. Quinn, “Design of Experiments and Optimization of Laser-Induced Graphene”, *ACS Omega*, vol. 6, no. 26, pp. 16736-16743, 2021.
- [48] A. Schott, S. Biehl, G. Bräuer, and C. Herrmann, “Thin Film Sensor Systems for Use in Smart Production”, in *Technologies for Economic and Functional Lightweight Design. Zukunftstechnologien für den Multifunktionalen Leichtbau*, K. Dröder and T. Vietor, Eds. Berlin, Heidelberg: Springer Vieweg, 2021, pp. 229-240.
- [49] S. Sang, L. Liu, A. Jian, Q. Duan, J. Ji, Q. Zhang, and W. Zhang, “Highly sensitive wearable strain sensor based on silver nanowires and nanoparticles”, *Nanotechnology*, vol. 29, pp. 255202, 2018.
- [50] X. Chen, F. Luo, M. Yuan, D. Xie, L. Shen, K. Zheng, Z. Wang, X. Li, and L.-Q. Tao, “A dual-functional graphene-based self-alarm health-monitoring e-skin,” *Adv. Funct. Mater.*, vol. 29, pp. 1904706, 2019.
- [51] C. Zhang, H. Chen, X. Ding, F. Lorestani, C. Huang, B. Zhang, B. Zheng, J. Wang, H. Cheng, and Y. Xu, “Human motion-driven self-powered stretchable sensing platform based on laser-induced graphene foams,” *Applied Physics Reviews*, vol. 9, p. 029901, 2022.

- [52] Y. Song, L. Chen, Q. Yang, G. Liu, Q. Yu, X. Xie, C. Chen, J. Liu, G. Chao, X. Chen, and M.-W. Chang, “Graphene-based flexible sensors for respiratory and airflow monitoring”, *ACS Applied Nano Materials*, vol. 6, no. 10, pp. 8937-8944, 2023.
- [53] H. C. Bidsorkhi, N. Faramarzi, B. Ali, L. R. Ballam, A. G. D'Aloia, A. Tamburrano, and M. S. Sarto, “Wearable graphene-based smart face mask for real-time human respiration monitoring”, *Materials & Design*, vol. 230, p. 111970, 2023.
- [54] J. Liao, X. Zhang, Z. Sun, H. Chen, J. Fu, H. Si, C. Ge, and S. Lin, “Laser-induced graphene-based wearable epidermal ion-selective sensors for noninvasive multiplexed sweat analysis,” *Biosensors*, vol. 12, no. 6, p. 397, 2022.

## **APPENDIX A: PROJECT SPECIFICATION**

### **Laser-induced graphene-based wearable sensors for health monitoring**

The rise of wearable sensors as rapidly advancing interdisciplinary technologies has found extensive use in health monitoring, robotics, and human-machine interactions. However, challenges persist in their commercialization in healthcare, including bio-interface design, personalization, and the need for enhanced performance and cost reduction [1].

Graphene, a material with a two-dimensional structure, has garnered increasing interest due to its exceptional electrical conductivity, mechanical strength, optical properties, and thermal conductivity. Several synthesis methods have been developed to commercialize graphene, including mechanical exfoliation, chemical vapor deposition, and chemical reduction of graphene oxide [2]. While these methods allow for the production of graphene with varying grades, their drawbacks are low productivity, high energy consumption, and extensive procedures resulting in significant costs. The “laser-induced graphene (LIG)” presents a straightforward solution to address these challenges [3].

The aim of this project is to develop and produce a wearable sensing system utilizing laser-induced graphene, created through direct laser irradiation on carbon-rich materials, for health monitoring. The focus will be on one-step, low-cost fabrication to simplify sensor production. Specifically, the project will identify materials as transfer substrates to improve the stretchability and gauge factor of the strain sensor. Additionally, it will optimize parameters for generating LIG from polyimide (PI), such as laser power, scanning speed, number of scanning cycles, and sensor pattern.

Subsequently, the morphology and sensing properties, including mechanical, electrical, and thermal characteristics, will be thoroughly examined. The obtained results will be compared with those of other models, and the most effective model for manufacturing the sensing system will be summarized. The culmination of the project will be the development of new LIG synthesis parameters for health monitoring, such as hand rotation and arm flexing, utilizing direct laser irradiation without requiring any other process or equipment.

[1] Sun B., McCay RN., Goswami S., et al. *Adv Mater.* 30(50), (2018), 1804327.

[2] Huang L., Su J., Song Y., et al. *Nano-Micro Lett.* 12, (2020), 157.

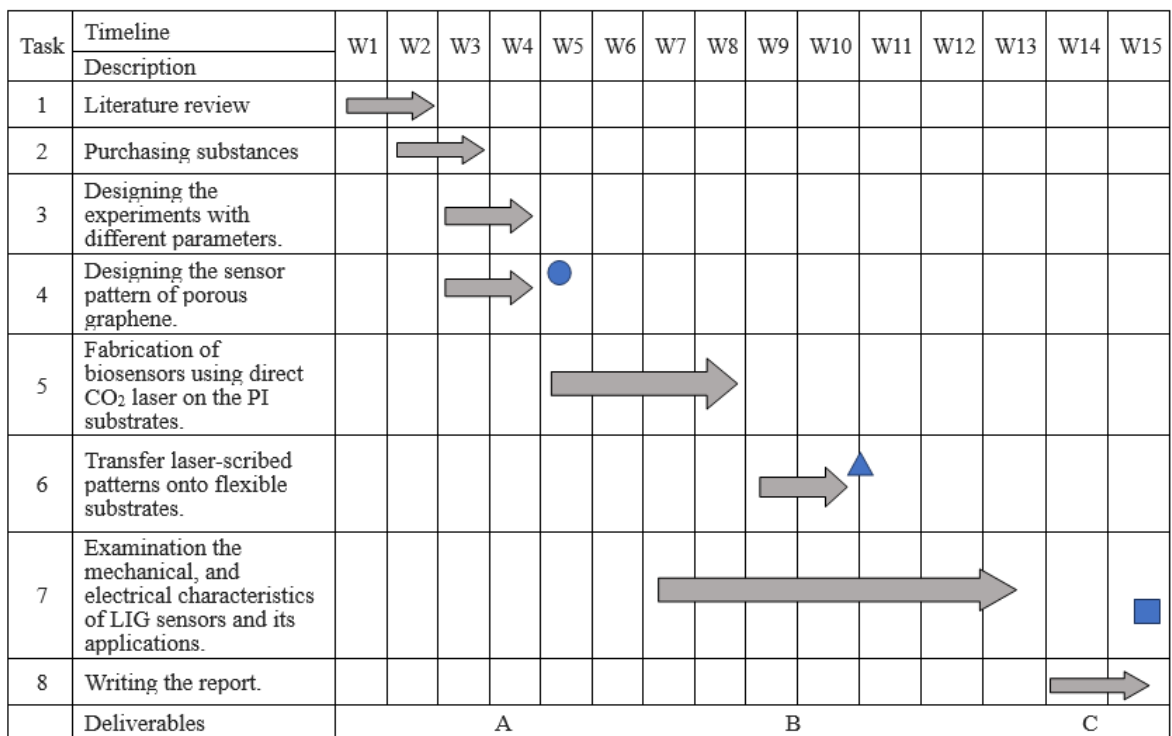
[3] Yang S., Chen YC., Nicolini L., et al. *Adv Mater.* 27(41), (2015), 6423.

The laser cutting machine (Laserscript-LS3040 Desktop) is located on the first floor of EEE Building Block B, specifically assigned to the BOSE group. The lab space designated for this project is on the fourth floor of EEE Building Block A. Professor Zheng Youbin, the lecturer overseeing this project, supervises every process on the first floor of EEE Building Block B.

After acquiring the required substances and designing the experiments, the next step involves modelling computer-designed layouts of open-mesh and Serpentine configurations on PI substrates. The fabrication of CO<sub>2</sub> laser-patterned porous graphene on PI was conducted using a laser systems platform with a wavelength of approximately 10.6 μm. The laser had a beam size ranging from 100 to 120 μm, a maximum power of 35 W, and a maximum scanning speed of 400 mm/s. The patterns of porous graphene, created through laser scribing, are subsequently transferred onto elastic substrates, such as packaging tape or medical tape. Finally, the resulting LIG sensors are examined for their suitability in wearable devices.

The work plan is presented in Table A-1. Based on the Gantt chart, tasks 1 to 4 were completed on schedule. Task 5, which involved the fabrication of LIG, began in week 5 as planned. However, additional fabrication efforts were undertaken from weeks 12 to 14 to enhance the performance of the LIG strain sensor for ECG signal detection. Similarly, task 6, which focused on transferring high-gas-permeable materials, did not fully meet expectations for all healthcare applications. Therefore, this task continued from week 9 to week 13. Task 7 also extended to week 14 due to the need for testing new materials. Despite these adjustments, ECG detection was successfully completed by the end of week 14. Task 8, which involves report writing, did not follow the original Gantt chart timeline precisely. Time waiting for material delivery was effectively utilized for writing the report. The revised Gantt chart is presented in Table A-2.

*Table A-1 Gantt chart.*



Deliverable	Description
A	New methodology of sensor fabrication
B	Developed LIG sensors with soft, flexible materials
C	Thesis report
Milestones	Description
	Experiment design made
	LIG strain sensor fabricated
	Thesis submission

*Table A-2 Revised Gantt chart.*

Task	Timeline	W1	W2	W3	W4	W5	W6	W7	W8	W9	W10	W11	W12	W13	W14	W15
	Description															
1	Literature review															
2	Purchasing substances															
3	Designing the experiments with different parameters.															
4	Designing the sensor pattern of porous graphene.															
5	Fabrication of biosensors using direct CO <sub>2</sub> laser on the PI substrates.															
6	Transfer laser-scribed patterns onto flexible substrates.															
7	Examination the mechanical, and electrical characteristics of LIG sensors and its applications.															
8	Writing the report.															
	Deliverables					A						B		C		

Deliverable	Description
A	New methodology of sensor fabrication
B	Developed LIG sensors with soft, flexible materials
C	Thesis report
Milestones	Description
●	Experiment design made
▲	LIG strain sensor fabricated
■	Thesis submission

Table A-3 outlines the risk management for potential events and their associated levels of danger, while Table A-4 provides a reference for the severity of potential injury or damage. As evident from the risk rating, all potential events fall within the moderate level, which is deemed acceptable for project execution.

*Table A-3 Risk Management.*

Actions	Likelihood	Severity	Risk rating	Mitigation
The properties of elastomer sponges are varied.	2	3	6	Provide an alternative methodology for the synthesis.
The design of the fabrication is not working.	2	3	6	Other designs are available.
Air contamination leakage from the machine.	1	5	5	Engineering controls must be in place prior to use, and materials must be compatible with the equipment.
High energy laser beam that can cause severe damage.	1	5	5	Follow the safety instructions carefully while working.
Illness that causes multiple weeks of absence.	2	3	6	Reduce the number of experimented variables and modify work plan.
Key staff leave the project.	1	5	5	Recruitment can be done.

*Table A-4 Severity of the potential injury/damage.*

0 – 5 = Low Risk		Severity of the potential injury/damage				
6 – 10 = Moderate Risk		Insignificant damage to Property, Equipment or Minor Injury	Non-Reportable Injury, minor loss of Process or slight damage to Property	Reportable Injury moderate loss of Process or limited damage to Property	Major Injury, Single Fatality critical loss of Process/damage to Property	Multiple Fatalities Catastrophic Loss of Business
11 – 15 = High Risk		1	2	3	4	5
16 – 25 = extremely high unacceptable risk		5	10	15	20	25
Likelihood of the hazard happening	Almost Certain 5	5	10	15	20	25
	Will probably occur 4	4	8	12	16	20
	Possible occur 3	3	6	9	12	15
	Remote possibility 2	2	4	6	8	10
	Extremely Unlikely 1	1	2	3	4	5

## APPENDIX B: ETHICAL APPROVAL

Version 1: 2021-22



### DEPARTMENT OF ELECTRICAL ENGINEERING AND ELECTRONICS

*Application for ethical approval for projects in which the researcher/s and the subject are the same person/people*

Student Name: Khanthapak Thaipakdee \_\_\_\_\_ Module: ELEC460 MSC Project \_\_\_\_\_

Supervisor: Youbin Zheng \_\_\_\_\_ Student ID No: 201750406 \_\_\_\_\_

Project Title: Laser-induced graphene-based wearable sensors for health monitoring \_\_\_\_\_

#### Section 1: Description of the research aims

The research aims must be described using language that can be understood by a lay reader. Please note that your application will be returned if the description of the research aims and design is not written in language that can be understood by a non-expert reader.

*(Recommended length: 100-200 words)*

The aim of this project is to design and fabricate a wearable epidermal sensing system utilizing laser-induced graphene (LIG) for health monitoring applications. This research will focus on optimizing two main types of parameters: the parameters for laser cutting, such as laser power, scanning speed, and cycle of scanning, and the materials used for producing LIG, including PI film, masking tape, packing tape, medical PE tape, etc. This project will employ direct laser irradiation on carbon-rich materials to simplify the process by eliminating multiple synthesis steps, reducing the need for complex equipment and techniques, and lowering costs. Additionally, the study will involve characterizing the sensing properties and developing the sensing system for effective health monitoring. The application of sensors includes measuring physiological signals such as human motion movements (hand rotation, finger bending, and arm flexing/extension). Pulse detection, ECG, EOG, and EMG will be studied, but they are not the primary goals of the project.

## **Section 2: Description of the research activity**

The research *activities* must be described using language that can be understood by a lay reader.

(Recommended length: 100-200 words)

The research activities can be described in two main types: one focuses on adjusting parameters to manufacture the sensor, and the other involves examining and applying the sensor. The parameters included in this project are laser power, scanning speed, cycle of scanning, and materials used to fabricate the sensor, such as PI film, masking tape, packing tape, medical PE tape, etc. To test the characteristics of the generated sensor, electrical and mechanical properties are evaluated. Optical microscope images of generated LIG sensor and Raman spectra (if available) are used to analyse the morphology of the LIG sensor. To examine the electromechanical properties of the sensor, electrical resistance variation at different tensile strains and different bending radii are measured, along with the stability of the sensor and other properties like water-vapor transmission and water-wicking distances. For the application phase, researcher will use the sensor to measure physiological signals, including hand rotation, finger bending, and arm flexing/extension, using himself as a subject.

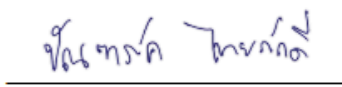
## **Section 3: Mitigation strategy**

The text in this section should describe the strategy that you will adopt to ensure that the risk to the researcher is reduced.

The system utilizes low voltage and current to significantly reduce the risk of electrocution. Additionally, there is no direct contact between the source of electricity and humans, as the LIG sensor functions as an electrical insulator. For detecting human movement, normal physiological movements will be examined, such as finger bending, which is one of the human features that does not apply any force to harm the user. The angle of body movement will be limited to 180 degrees to prevent fatigue or any muscle damage. Additionally, for detecting wrist pulse or eye blinking, there is no risk involved that could harm the user. For studying ECG, EOG, and EMG, the tests will be conducted for no more than 2 minutes at a time to mitigate the risk. Moreover, before conducting any test, the equipment will be checked to prevent any risk.

I have agreed these limits with my supervisor. I understand that results from any tests that exceed these limits cannot be included in the thesis, and I may be subject to further academic penalties if I conduct any measurements outside the agreed limits.

Student Signature:



Date: 16 July 2024

Supervisor Signature:



Date: 16 July 2024

Approved: Mark Bowden, Dept Ethics Lead, 29/07/2024

## APPENDIX C: LIG-BASED STRAIN SENSORS ON PROTECTION TAPE, BANDAGE, AND PE NONWOVEN TAPE

Figure C-1 showcases various patterns of LIG-based strain sensors fabricated on silicone protection tape. Each sensor pattern is illustrated to highlight differences in design and performance.



*Figure C-1 LIG strain sensor with different patterns on silicone protection tape.*

Table C-1 presents the performance characteristics of LIG-based strain sensors fabricated on silicone protection tape with various patterns (Zigzag, Serpentine, Square, Shutter). The table details the laser power, scanning speed, initial resistance, percentage change at a 0.25 mm radius, and recovery percentage for each pattern.

The serpentine pattern shows the highest percentage change at 0.25 mm radius, reaching 102.13%. This indicates that the serpentine pattern exhibits the greatest relative change in resistance when subjected to strain.

The square pattern demonstrates the highest recovery percentage at 93.34%. This signifies that the square pattern has the best ability to return to its original resistance state after deformation.

However, when applied in healthcare settings, the sensor struggles to capture changes associated with finger bending, elbow bending, hand gripping, or arterial pulse. While the sensor's soft and flexible substrate is advantageous, its thickness of 0.2 mm may impede accurate signal detection. Additionally, a slower response time could make it challenging to capture rapid resistance changes, further affecting the sensor's performance in recording these physiological signals.

*Table C-1 Performance characteristics of LIG-based strain sensors with different patterns on silicone protection tape.*

Pattern	Power (%)	Speed (mm/s)	Initial Resistance (W)	Percentage change at 0.25 mm radius (%)	Recovery (%)
Zigzag	10	200	248548.8	58.00%	66.66%
Serpentine	10	200	441258.7	42.64%	72.51%
Square	10	200	31419.4	76.80%	90.47%
Shutter	10	200	23944.53	62.83%	62.07%
Zigzag	25	400	123456.8	72.60%	67.05%
Serpentine	10	200	136796.3	102.13%	60.33%
Square	10	200	30734.22	52.16%	93.34%
Shutter	10	200	20782.19	40.52%	88.30%

Figure C-2 showcases various patterns of LIG-based strain sensors transferred on medical tape. Figure C-2a shows the LIG strain sensor with a zigzag pattern directly applied to the medical tape. This subfigure captures the sensor's appearance before any additional covering or modifications. Figure C-2b demonstrates the same LIG strain sensor, now covered with an additional layer of medical tape. This subfigure highlights the sensor's configuration after being sandwiched between layers of medical tape, providing insight into how the sensor is protected and its interaction with the substrate. Due to its low elongation break percentage, medical tape easily stretches beyond its initial length, causing the sensor pattern to deviate from its intended design. While the LIG sensor on medical tape is capable of detecting human motion, it is unable to effectively detect arterial pulse.



*Figure C-2 LIG strain sensor zigzag on medical tape  
(a) Normal sensor, (b) Sandwich covered with medical tape.*

Figure C-3 illustrates the graphene-based LIG sensors with square and shutter patterns applied to a bandage.

- Figure C-3a shows the sensors in their original, unstretched state, displaying the graphene square and shutter patterns on the bandage.
- Figure C-3b depicts the graphene shutter pattern sensor when the bandage is stretched.
- Figure C-3c demonstrates the graphene square pattern sensor under the same stretching conditions.

It can be observed that stretching the bandage causes discontinuities in the sensor patterns, resulting in a loss of their specific shapes. Additionally, after 2 or 3 stretching cycles, the resistance of the sensors increases significantly, exceeding  $10 \text{ M}\Omega$ , indicating that the bandage may not be suitable for this application. However, exploring the use of bandage as a substrate material instead of PI film could be a valuable area for further investigation.

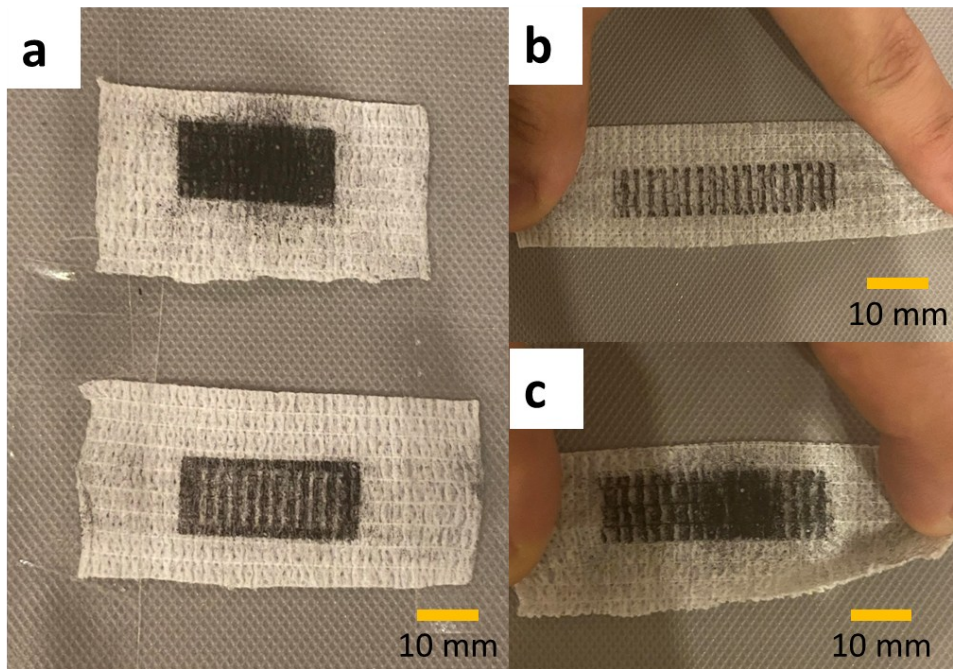


*Figure C-3 Graphene square and shutter patterns on bandage  
(a) Initial state, (b) shutter pattern under stretch, and (c) square pattern under stretch.*

## APPENDIX D: CODING

Snippet Code D-1 represents the code related to wavelet filtering, a 0.5 Hz high-pass filter, and peak analysis. The wavelet filter utilizes a Daubechies wavelet of order 6 with a decomposition level of 4. The high-pass filter applied is a highpassiir filter of order 8. The parameter MinPeakDistance is set to 150 peaks per minute; if the user's heart rate exceeds this value, this number should be adjusted accordingly. Additionally, MinPeakHeight can be modified to optimize the accuracy of peak detection.

### Snippet Code D-1

```
% Filter using wavelet
% Choose wavelet
wavelet = 'db4'; % Daubechies wavelet of order 6

% Perform wavelet decomposition
[coeffs, levels] = wavedec(noised_signal, 4, wavelet); % 4 levels of decomposition

% Set threshold
threshold = sqrt(2*log(length(noised_signal))); % Universal threshold

% Apply soft thresholding
for i = 1:length(coeffs)
    coeffs(i) = sign(coeffs(i)) * max(abs(coeffs(i)) - threshold, 0);
end

% Reconstruct the signal
reconstructedSignal = waverec(coeffs, levels, wavelet);

% Parameters
highPassCutoff = 0.5; % Cutoff frequency for high-pass filter (Hz)
fs = 1000; % Sampling frequency (Hz)

% Design high-pass filter to remove baseline drift
hpFilt = designfilt('highpassiir', 'FilterOrder', 8, ...
    'HalfPowerFrequency', highPassCutoff, ...
    'SampleRate', fs);

% Apply high-pass filter to correct baseline drift
denoised_signal = filtfilt(hpFilt, reconstructedSignal);

% Find peak
mean_denoised_signal = mean(denoised_signal);
std_denoised_signal = std(denoised_signal);
[peaks, locsMax] = findpeaks(denoised_signal, MinPeakDistance = 60*fs/150, MinPeakHeight = mean_denoised_signal + std_denoised_signal);
```

```

% Define baseline
baseline = mean(denoised_signal);

tolerance = 0.05; % Tolerance for checking if values are nearly equal to the baseline

% Find indices where the signal is nearly equal to the baseline
baseline_indices = find(abs(denoised_signal - baseline) < tolerance);

% Sort baseline_indices to ensure sequential processing
baseline_indices = sort(baseline_indices);

max_distance = MinPeakDistance; % Maximum distance to consider a segment valid

% Loop through each local maximum

for i = 1:length(locsMax)
    % Find the nearest baseline point before the peak
    baseline_before_peak = baseline_indices(baseline_indices < locsMax(i));
    if ~isempty(baseline_before_peak)
        % Take the last baseline index before the peak
        baseline_before_peak = baseline_before_peak(end);
        % Check the distance
        if abs(locsMax(i) - baseline_before_peak) < max_distance
            % Plot from this baseline point to the peak in green
            % Green for upward trend
            plot(t(baseline_before_peak:locsMax(i)), ...
                  denoised_signal(baseline_before_peak:locsMax(i)), 'Color', '#77AC30');
        end
    end

    % Find the nearest baseline point after the peak
    baseline_after_peak = baseline_indices(baseline_indices > locsMax(i));
    if ~isempty(baseline_after_peak)
        % Take the first baseline index after the peak
        baseline_after_peak = baseline_after_peak(1);
        % Check the distance
        if abs(baseline_after_peak - locsMax(i)) < max_distance
            % Plot from the peak to this baseline point in red
            % Red for downward trend
            plot(t(locsMax(i):baseline_after_peak), ...
                  denoised_signal(locsMax(i):baseline_after_peak), 'Color', '#A2142F');
        end
    end
end

plot(t, baseline * ones(size(t)), 'k--'); % Baseline as a dashed black line

```